

学位論文

**Laser Detonation Propulsion with  
Solid-state Laser**

(固体レーザーを用いたレーザー爆轟推進の研究)

王 彬



# INDEX

<b>Chapter 1 INTRODUCTION .....</b>	<b>7</b>
1.1 Background.....	7
1.2 Laser detonation launching system.....	11
1.3 Scope of present study .....	22
1.4 Objectives .....	27
References.....	28
<b>Chapter 2 SUPPORTING CONDITIONS OF LASER DETONATION .....</b>	<b>31</b>
2.1 Experimental apparatus and methods .....	32
2.2 Results and discussions.....	44
2.3 LSD termination condition .....	50
2.4 Summary of Chapter 2.....	53
References.....	54
<b>Chapter 3 BLAST WAVE ENERGY CONVERSION PROCESS.....</b>	<b>55</b>
3.1 Fractional and temporal laser absorption.....	56
3.2 Shadowgraph experiment apparatus .....	62
3.3 Method to estimate the blast wave energy efficiency .....	65
3.4 Ambient pressure influence .....	74
3.5 Summary of Chapter 3.....	78
References.....	79
<b>Chapter 4 THRUST GENERATION PROCESS.....</b>	<b>80</b>
4.1 Experimental setup for thrust measurement .....	80
4.2 Results and discussions.....	85
4.3 Summary of Chapter 4.....	89
References.....	90
<b>Chapter 5 CONCLUSIONS.....</b>	<b>91</b>
<b>PUBLICATIONS.....</b>	<b>93</b>
<b>ACKNOWLEDGEMENTS.....</b>	<b>95</b>

# List of Figures

1.1	Varieties of laser propulsion, (a) Flat plate type laser propulsion, (b) Pulsejet laser propulsion with a Bell nozzle and (c) Laser In-tube Accelerator (LITA) with a wall ablator.....	10
1.2	Circle of pulsed detonation engine, from left to right: laser ignition and energy absorption, impulse generation and breath .....	12
1.3	Vertical launching of a 100 kg vehicle to GEO through three modes of laser propulsion, with payload ratio of 0.6 .....	12
1.4	Momentum coupling coefficient for laser detonation thrusters (Bohn and Schall, 2002; Pirri, Monsler and Nebolsine, 1974; Tang, Gong and Hu, 2003; Mori, Sasoh and Myrabo, 2005).....	14
1.5	Plug-nozzle type Lightcraft .....	14
1.6	Typical LSD wave structure .....	16
1.7	Electron density distribution around LSD termination time, $t_{\text{term}} = 1.4 \mu\text{s}$ .....	18
1.8	Laser heating rate and local laser energy density behind the shock wave, $t_{\text{term}} = 1.4\mu\text{s}$ .....	19
1.9	Schematic of regime transition from LSD to LSC .....	24
2.1	The Nd:glass laser, (a) its photo and (b) principle diagram. ....	33
2.2	Energy meter QE25LP-S-MB .....	34
2.3	Photodetector.....	36
2.4	Laser pulse shape and cumulative energy for $E_i = 1.0$ and $2.0 \text{ J}$ .....	37
2.5	Laser power in log-scale, pulse width 33 ns .....	37
2.6	Laser burn pattern gotten with energy paper.....	38

2.7	Laser transverse mode .....	38
2.8	Schematic of the experimental setup for shadowgraph measurement. (PD1, PD2, photodetectors; EM1, EM2, energy meters; L1, high-energy laser focusing lens; L2, L3, L4, lenses; BE, beam expander; PG, pulse generator; ICCD, intensified CCD high-speed camera). .....	40
2.9	Ultra 8 high speed camera .....	41
2.10	Pulse generator, Stanford Research Systems, Inc. DG535 .....	41
2.11	(a) Setup of Half-Shadowgraph-Half-Self emission (HSHS) experiment and (b) a picture taken with this arrangement, $E_i = 1.0 \text{ J}$ , $f = 6.27$ .....	43
2.12	Shadowgraphs of $E_i = 2.0 \text{ J}$ , $f = 6.27$ at different time after breakdown in atmosphere air .....	45
2.13	Schematic diagram of two directions propagation LSD wave .....	45
2.14	Temporal displacements of the shock wave front R and the ionization front Ri. Subscript a, forward expansion; b, backward expansion. $E_i = 1.0 \text{ J}$ (a) and $2.0 \text{ J}$ (b)....	47
2.15	Propagation speeds of LSD waves in directions of (a) upstream (backward), $V_a$ , and (b) downstream (forward), $V_b$ for $E_i = 1.0 \text{ J}$ and $2.0 \text{ J}$ , 1 atm atmosphere air .....	49
2.16	Schematic of the glass-laser induced LSD wave .....	51
2.17	Laser intensities on the backward propagation shock waves, $E_i = 1.0 \text{ J}$ and $2.0 \text{ J}$ , $f = 6.27$ .....	52
3.1	Energy conversion process for laser propulsion with a solid-state laser.....	55
3.2	Setup of fractional energy absorption experiment .....	57
3.3	Energy absorption variation with laser pulse energy, $E_i = 1.0, 1.5$ , and $2.0 \text{ J}$ .....	58
3.4	Temporal shapes of transmitted and absorbed laser power (a) $E_i = 1.0 \text{ J/pulse}$ and (b) $2.0 \text{ J/pulse}$ . $f = 6.27$ .....	60
3.5	Setup of shadowgraph experiment .....	63
3.6	Optical setup for focusing $f$ number 3.75 .....	63
3.7	Test cell for the experiments at reduced ambient pressures, (a) photo and (b) a schematic diagram.....	64

3.8	Images of evolution of the laser absorption wave, $E_i = 1.0$ J (a), and schematic of laser generated blast wave expanding in three directions (b) .....	66
3.9	Temporal $R$ variations and the expansion velocities for $E_i = 1.0$ J (a) and 2.0 J (b), $f = 6.2$ .....	67
3.10	Temporal $R$ variations and the expansion velocities for $E_i = 1.0$ J (a) and 2.0 J (b), $f = 3.75$ .....	68
3.11	Temporal $g$ variation with $E_i = 1.0$ J and 2.0 J, $f = 6.27$ .....	71
3.12	Energy absorbed under reduced air pressure, $E_i = 2.0$ J, $f = 3.75$ .....	75
3.13	Temporal incident and transmitted laser power $E_i = 2.0$ J/pulse; air pressures are 101, 80, 50 and 30 kPa .....	75
3.14	Blast wave expansion in three directions, for (a) 101 kPa, (b) 80 kPa, (c) 50 kPa and (d) 30 kPa .....	76
3.15	Temporal $g$ variation at reduced ambient pressure .....	77
4.1	Impulse pendulum experimental setup .....	82
4.2	Design map (a) and photo (b) of conical nozzle thrusters .....	82
4.3	Schematic of calibration setup .....	83
4.4	(a) Photo of load cell and (b) typical load cell signal .....	83
4.5	Calibration line, using a nozzle with $45^\circ$ apex angle .....	84
4.6	Measured $C_m$ at various dimensionless nozzle lengths, (a) $\alpha = 15^\circ$ ; (b) $\alpha = 22.5^\circ$ for glass laser and $\alpha = 30^\circ$ for $\text{CO}_2$ laser .....	87
4.7	Blast wave shapes in the nozzles at LSD termination time, for (a) TEA $\text{CO}_2$ laser, (b) and (c) Nd:glass laser .....	88

# List of Tables

1.1	Characteristics of high power lasers.....	21
2.1	Specification of the Nd:glass laser.....	33
2.2	Specification of energy meter.....	34
2.3	Specifications of photodetector (Electro-Optics Technology, Inc.).....	36
2.4	Laser intensity threshold for backward LSD termination, together with CO <sub>2</sub> laser result.....	51
3.1	Measured fractional transmission for Nd:Glass laser and CO <sub>2</sub> laser.....	59
3.2	Energy efficiencies with CO <sub>2</sub> laser data.....	71
3.3	Energy flow in the blast wave energy conversion process.....	73
3.4	Energy flow in the blast wave energy conversion process under various ambient pressure, $f = 3.75$ .....	77
4.1	Measured maximum $C_m$ with solid state laser, together with data got in former CO <sub>2</sub> laser experiments.....	85

# NOMENCLATURE

$c$	: speed of light
$C_m$	: momentum-coupling coefficient
$c_a$	: speed of sound
$D$	: minimum velocity of a supersonic discharge wave
$D_{LSD}$	: distance between the focus point and the shock front.
$e$	: electron charge
$E_{abs}$	: absorbed laser energy
$E_{bw}$	: blast wave energy
$E_i$	: laser pulse energy
$E_{LSD}$	: laser energy absorbed during the LSD regime
$f$	: focusing number
$G$	: gaunt factor
$h$	: planck's constant
$I$	: propulsive impulse
$I_0$	: intensity of the laser radiation
$k_B$	: boltzmann's constant
$k_{e-i}$	: energy transfer between electrons and ions
$k_{e-n}$	: energy transfer between electrons and neutron particles
$k_{IB}$	: inverse-Bremsstrahlung absorption coefficient
$m_e$	: electron mass
$M_s$	: blast wave expansion Mach number
$n_e$	: number density of electron
$n_i$	: number density of ion
$n_n$	: number density of neutron particles
$p_a$	: ambient air pressure
$P_{spike}$	: laser power at the leading spike
$P_{tail}$	: laser power at the tail
$R$	: displacement of shock front
$R_a$	: backward shock wave expansion displacement
$R_b$	: forward shock wave expansion displacement
$R_c$	: largest shock wave displacement vertical to the laser axis

$R_i$	: displacement of ionization front
$R_{\text{major}}$	: major radius of a elliptical expansion blast wave
$R_{\text{minor}}$	: minor radius of a elliptical expansion blast wave
$r$	: laser channel radius
$r^*$	: characteristic shock wave radius
$r_{\text{LSD}}$	: radius on the blast wave front that irradiated by the laser beam
$r_n$	: nozzle length
$\tilde{r}_n$	: dimensionless nozzle length
$S$	: laser power density irradiated on the LSD wave
$t$	: time
$V_a$	: upstream Propagation speed of LSD wave
$V_b$	: downstream Propagation speed of LSD wave
$V_{\text{bw}}$	: volume involved in blast wave
$V_{\text{LSD}}$	: propagation speed of LSD wave
$\Delta x$	: laser absorption layer thickness
$z$	: ion charge number
$\alpha$	: half-cone angle
$\gamma$	: ratio of specific heats
$\gamma_{\text{eff}}$	: effective specific heat ratio
$\eta_{\text{abs}}$	: fractional laser energy absorption
$\eta_{\text{bw}}$	: blast wave energy efficiency
$\eta_{\text{LSD}}$	: fractional laser energy absorbed during the LSD regime
$\lambda$	: laser wave length
$\rho$	: gas pressure behind the shock wave
$\rho_a$	: ambient gas density
$\rho_0$	: ambient gas density ahead of the LSD wave

# Chapter 1

## INTRODUCTION

### 1.1 Background

#### *Status of present launch systems*

Space launch technology has been developed for longer than half century after the first orbital launch in 1957. As an expendable launch vehicle (ELV), chemical rocket is still dominant nowadays, because it's relatively affordable and reliable. However, it is in fact too expensive to be used for many space exploration proposals, like Solar Power Satellite<sup>[1]</sup>, space settlement or lunar base project<sup>[2,3]</sup>. Because the major portion of the launch mass is propellant, a typical payload launch to the LEO is only less than 4% by now. The common launch cost to a low earth orbit (LEO) is more than 5,000 \$/kg, which increases to 15,000 \$/kg for the geostationary transfer orbit<sup>[4]</sup>.

As an alternative, National Space Transportation System, space shuttle<sup>[5]</sup> was designed for multiple human space flight missions. It can carry different payloads to LEO, therefore has been used to service the International Space Station (ISS) for cargo supply and crew rotation. The requirement of reuse makes its system not so simple like that of the ELV. Moreover, the mass of orbiter structure limited the payload it can launch. For these reasons, the cost of space access is even higher than ELV, about 18,000 \$/kg as estimated for LEO<sup>[6]</sup>.

Besides of these practically used launching systems, there are other proposals which are under development. One of the most promising choices is the mass driver method. In which, the acceleration to high speed of projectile could be achieved by electromagnetic force on a fixed path, coilgun<sup>[7,8]</sup> or railgun<sup>[9-11]</sup>. After separating, the payload part continues the flight due to the momentum it gained. It is thought that this system can get energetic efficiency as

high as 90%, with applying superconducting coils to fabricate the path. The launch cost of mass driver could be dramatically reduced since the major part of facility, the path has great reusability, and the payload part could be extremely simple. Moreover, the projectile part could be very simple, since there is no need for on-board energy supply system. The mass driver is more advantageous for using in space than on the ground, because when the velocity increases to a certain high value, the projectile will suffer to severe aerodynamic heating as well as air drag deceleration if it is launching from the ground.

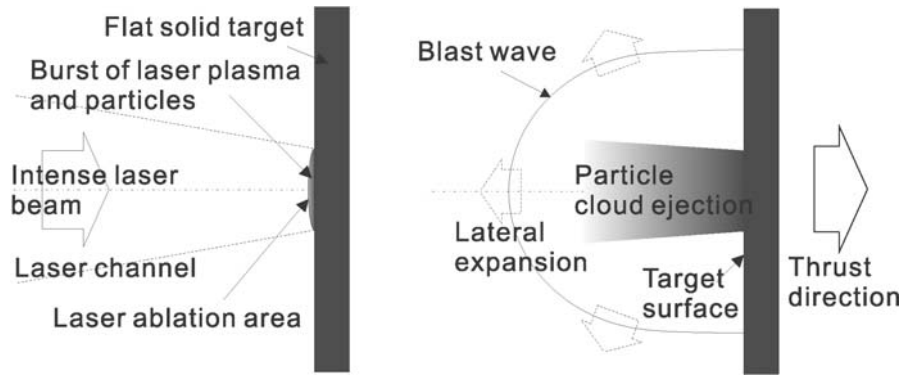
### *Laser propulsion*

A space launch system powered by high-power ground-based lasers was first proposed by Kantrowitz<sup>[12]</sup> in 1972. This beamed energy launch system is now recognized as a potential low-cost, low-emission, and resource-saving alternative to chemical rocket launch vehicles. Using laser heating instead of combustion, rocket propulsion parameters are not limited by propellant chemistry: the specific impulse  $I_{SP}$  depends simply on the ability to focus the energy beam; infinite  $I_{SP}$  can be realized in no-fuel air-breathing flights in the atmosphere, although propellant is necessary for flight out of the atmosphere. The thrust to mass ratio is a function of the available laser power, and the acceleration could be greater than  $10\times g$ . The craft need not park in a low earth orbit and can instead head directly for a geosynchronous orbit or beyond<sup>[13]</sup>. Such vehicles require neither a pressure vessel nor a turbo-pump system when the gas is heated rapidly by intense pulsed laser irradiation such as laser-supported detonation or laser ablation. Vehicle structures are expected to be very simple, inexpensive, and disposable. In contrast, laser facilities, the cost of which is predominant among all launch costs, are maintainable and replaceable at any time because they remain on the ground. Different varieties of laser propulsion were proposed include flat plate, pulsejets type and In-tube Accelerator, which are schematically shown in Figure 1.1.

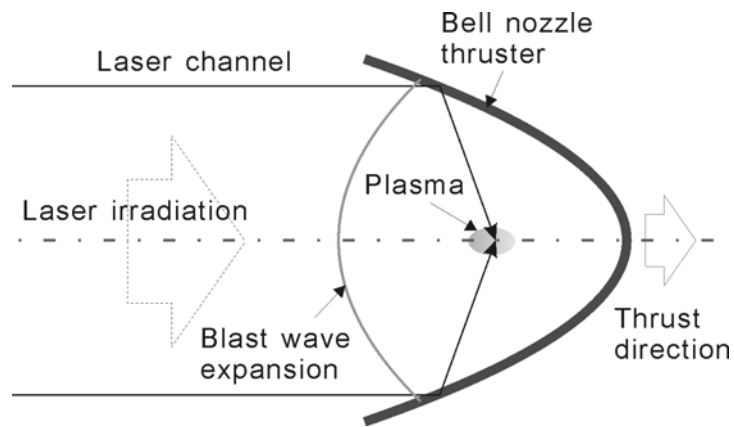
The concepts of 'Highways of Light' and 'Beam Riding' present explicit images of future space-transportation systems using beamed energy propulsion: an extremely energetic laser-propelled vehicle will ride on virtual energy highways, for which a grid of remote

energy-beaming power plants is located either in space or on the ground<sup>[16]</sup>. The vehicle geometry will be designed so that the side force and pitching moment act against any tendency of the vehicle to drift from the beam's center<sup>[17]</sup>. This beam-riding capability also obviates long-distance vehicle tracking, precise beam pointing, and vehicle attitude control.

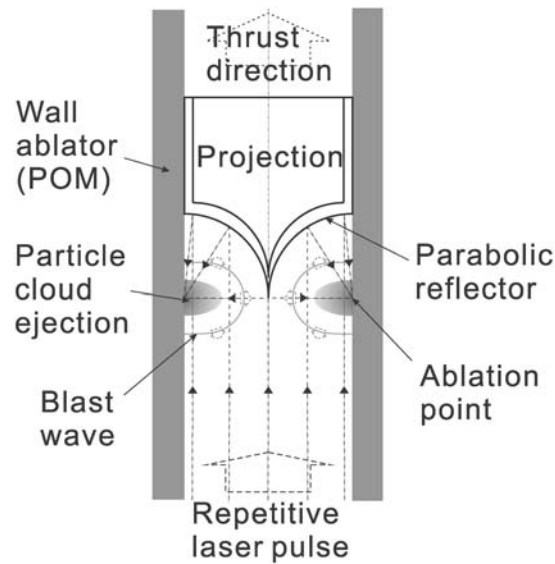
In-space laser propulsion was also proposed by Minovich<sup>[18]</sup>. Using a remote power supply from space-based lasers, the specific power (available power per thruster system weight) would be drastically greater than that of solar electric propulsion, and mission times would be shortened. In continuous wave laser propulsion<sup>[19]</sup>, a stable laser discharge plasma is sustained apart from a pressure chamber wall, so that a higher gas temperature and therefore higher specific impulse can be expected than that provided by chemical thrusters. Furthermore, laser microthrusters<sup>[20]</sup> using on-board diode lasers have been proposed for orienting or repositioning microsatellites with precise thrust control. The diode lasers need only a few watts of power at a few tens of volts; they will be driven directly by a solar array. This would be distinctly advantageous compared to conventional compact electric propulsion thrusters such as Pulsed Plasma Thrusters and Field Emission Electric Propulsions.



(a)



(b)



(c)

Figure 1.1: Varieties of laser propulsion, (a) Flat plate type laser propulsion<sup>[14]</sup>, (b) Pulsejet laser propulsion with a Bell nozzle<sup>[14]</sup> and (c) Laser In-tube Accelerator (LITA) with a wall ablator<sup>[15]</sup>

## 1.2 Laser detonation launching system

### *Laser Detonation Thrusters*

Most laser detonation thrusters are designed to use the Earth's atmosphere to great propulsive advantage during atmospheric flight, enabling a considerable reduction in the propellant mass and an increase in the payload fraction. Pulsed gas or solid lasers are used to generate laser detonation waves on the bottom of a vehicle. Impulsive thrust is applied to the thruster when the blast wave reached its inner wall. During the pulse interval, fresh air replaces the heated air. This cycle is designated as a pulsed detonation engine (PDE, Figure 1.2).

A laser PDE propelled vehicle will reach an orbit by switching its engine cycle mode. At the initial stage, air is taken and exhausted from the bottom of the vehicle (pulsejet mode). As a result of vehicle acceleration, when ram-compression becomes available, air is taken and compressed from the top (ramjet mode). Finally, when the altitude is too high that the vehicle cannot breathe sufficient working air, on-board propellant, hydrogen or argon, for example, will be injected (rocket mode). Impulsive thrust is generated through the three modes as the result of laser induced explosion.

For launching a vehicle to GEO, a velocity increase of 10 km/s is needed. An adapt of engine cycle analysis was performed by Katsurayama et al<sup>[13]</sup> in 2003 to evaluate the feasibility of laser detonation propulsion. In the calculation, they assumed that a 100 kg laser beam riding vehicle is vertically launched from the sea-level to an altitude of 200 km with a 100 MW power level pulsed laser. The estimated laser propulsion trajectory with PDE engine is shown in Fig. 1.3.

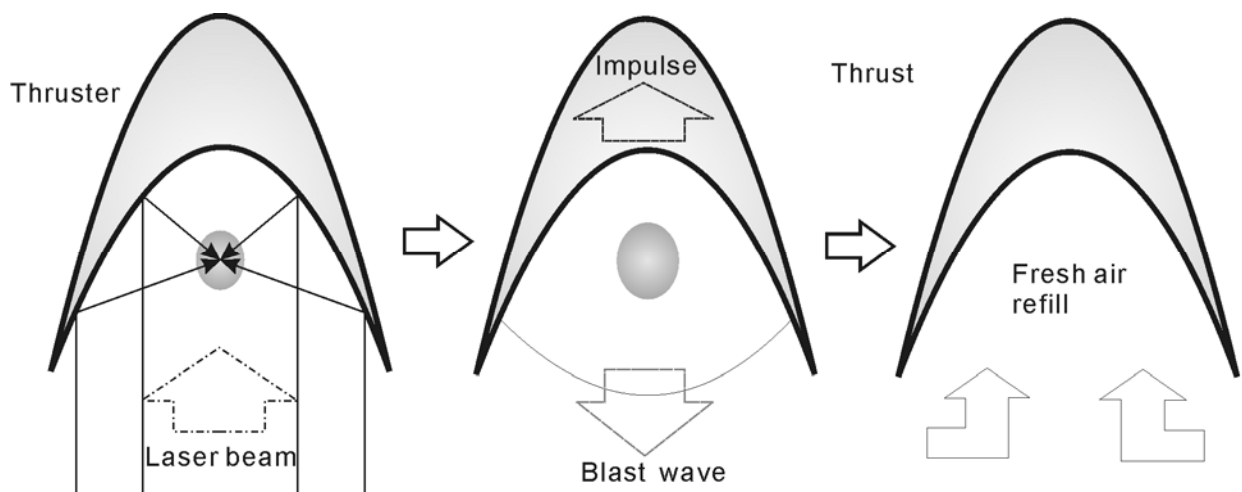


Figure 1.2: Circle of pulsed detonation engine, from left to right: laser ignition and energy absorption, impulse generation and breath.

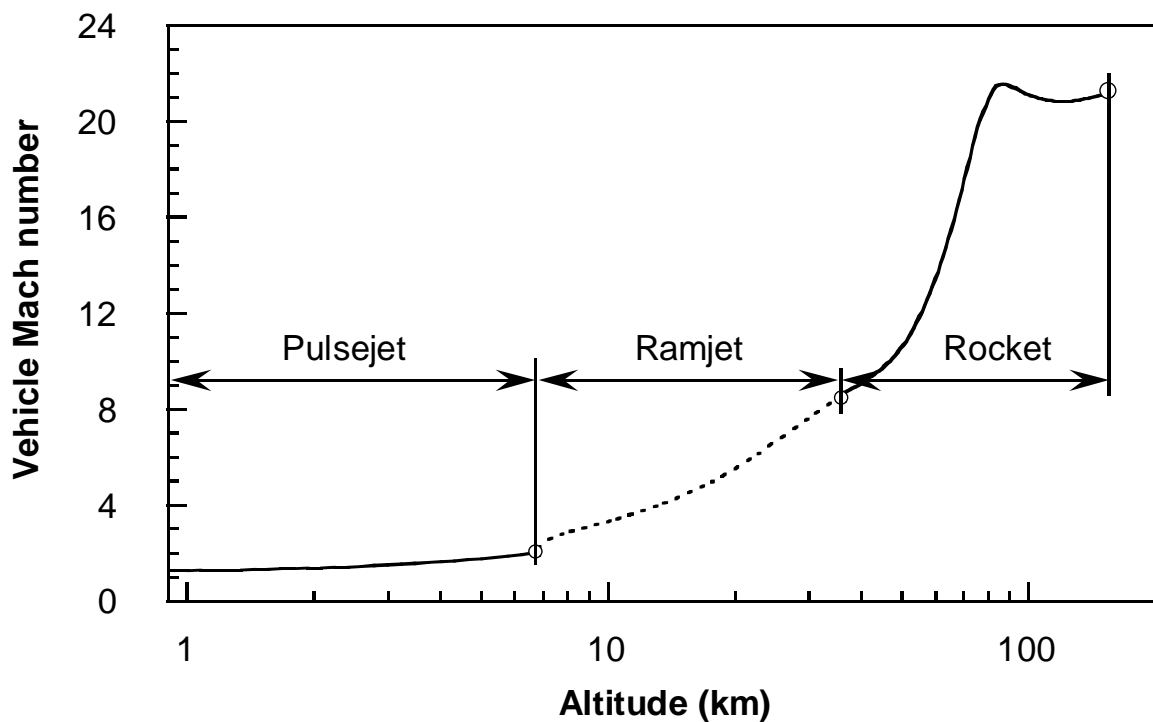


Figure 1.3: Vertical launching of a 100kg vehicle to GEO through three modes of laser propulsion, with payload ratio of 0.6<sup>[13]</sup>.

### *Thrust performance*

Thrust performance of pulse-laser driven thrusters is typically evaluated in terms of momentum-coupling coefficient  $C_m$ . It's a ratio of propulsive impulses  $I$  thruster obtained to input laser energy  $E_i$  expressed as:

$$C_m \equiv \frac{I}{E_i} \quad (1-1)$$

A Bell-nozzle thruster<sup>[21-23]</sup> in which a parabolic mirror is used to concentrate the incident laser beam and to reflect induced blast waves achieved high  $C_m$  of up to 400 N/MW with pulsed energy of about 200J using a TEA-CO<sub>2</sub> laser. Figure 1.4 portrays the data of measured  $C_m$  for various vehicle geometries.

Tang found that larger  $C_m$  is achieved with smaller focal length and larger nozzle diameter. The  $C_m$  in a single pulse test is higher than that in a multi-pulse test. The reflector is subjected to strong thermo/mechanic impact for multi-pulsed tests, which is expected to be a critical problem to overcome through future studies.

The plug nozzle Lightcraft designed by Myrabo<sup>[25]</sup> is presented in Fig. 1.5. The vehicle employs a plug-shaped parabolic mirror to concentrate the incident laser radiation to a circular line focus located close to an annular shroud, which serves as the principal impulse surface. The pulsed laser radiation ignites a strong laser detonation wave in the air or rocket propellant gas flowing over the impulse surface. The forebody aeroshell acts as an external compression inlet for the airbreathing engine mode.

In 2000, on the White Sands Missile Range in New Mexico, USA, a new altitude record of 71 m was set with a 12cm diameter model using a 10kW pulsed CO<sub>2</sub> laser<sup>[26]</sup>. The improved #200-series Lightcraft used a plastic ablative propellant. It was spin-stabilized to 10,000RPM immediately before launch. The vehicle was accelerated during the first 2s; thereafter, it maintained a quasi-constant velocity of 8.2m/s for the next 3.5s. Most of the 12.7s flight was spent hovering at about 200 feet, before setting the new world altitude record. The vehicle sustained no notable damage. The craft simultaneously demonstrated the longest ever laser-powered free flight.

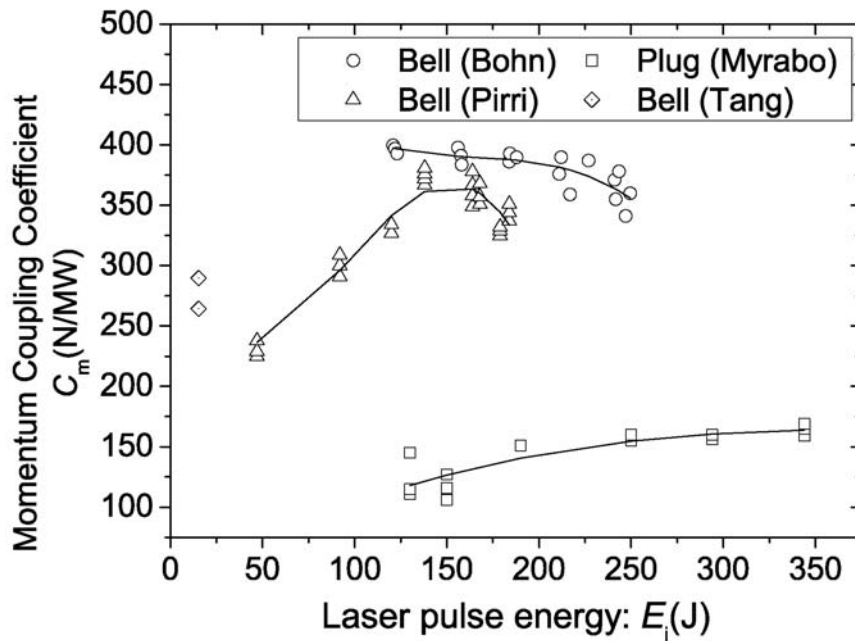


Figure 1.4: Momentum coupling coefficient for laser detonation thrusters<sup>[21-24]</sup> (Bohn and Schall, 2002; Pirri, Monsler and Nebolsine, 1974; Tang, Gong and Hu, 2003; Mori, Sasoh and Myrabo, 2005).

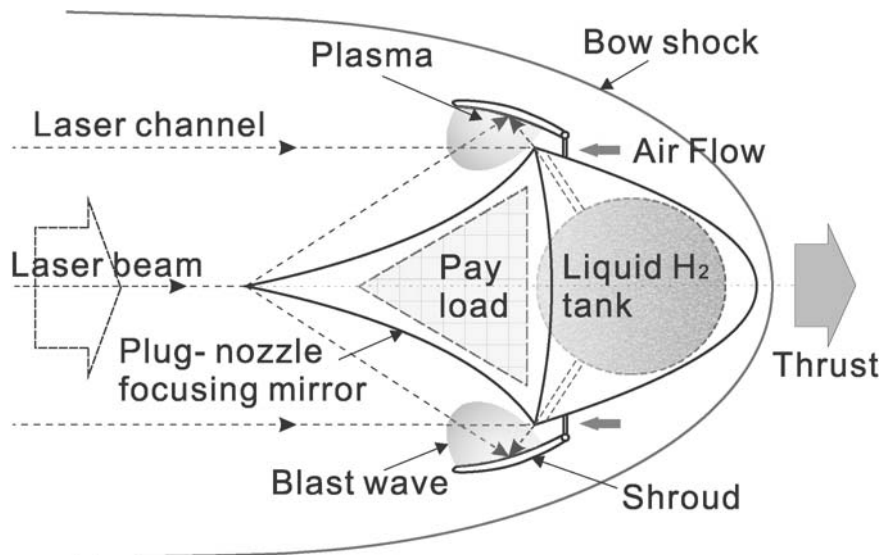


Figure 1.5: Plug-nozzle type Lightcraft<sup>[25]</sup>.

### *Laser Supported Detonation (LSD)*

A laser-supported absorption wave is ignited by laser-induced gas breakdown, spark discharge, particulate absorption, or ignition off a metal target. Figure 1.6 portrays the absorption wave structure in the laser supported detonation (LSD) regime<sup>[27]</sup>. For CO<sub>2</sub> laser, the incident laser energy is absorbed in a thin layer behind the leading-edge shock wave. The wave propagates opposite to the incident laser beam. The minimum velocity of a supersonic discharge wave corresponding to the Chapman–Jouguet detonation  $D$  is

$$D = \left[ 2(\gamma^2 - 1) I_0 / \rho_0 \right]^{1/3} \quad (1-2)$$

where  $\gamma$  is the ratio of specific heats,  $\rho_0$  is the ambient density of the gas ahead of the LSD wave, and  $I_0$  is the intensity of the laser radiation.  $D$  is approximately 100km/s when a 10MW beam is focused on a circle of 0.1mm diameter in the atmosphere ( $\rho_0 = 1 \text{ kg/m}^3$ ). The gas pressure within the space immediately behind the shock wave is (for  $p_0/p \rightarrow 0$ )

$$p = \rho_0 D^2 / (\gamma + 1) \quad (1-3)$$

With the decrease in  $I_0$ , the detonation wave becomes weaker and finally terminates at a critical condition in which the energy loss attributable to the lateral wave expansion becomes comparable to the energy used in driving the detonation wave. The condition can be characterized by the ratio of the absorption layer thickness  $\Delta x$  (reciprocal of the optical absorption coefficient) to the laser channel radius  $r$ .

Mori<sup>[28]</sup> experimentally studied the characteristics of LSD wave induced by point focusing pulsed CO<sub>2</sub> laser in air under various conditions such as focusing number, laser energy and ambient pressures. The measured LSD wave propagation speed agrees reasonably with the cube-root law (Eq. (1-2)) though there are certain differences on the experimental conditions.

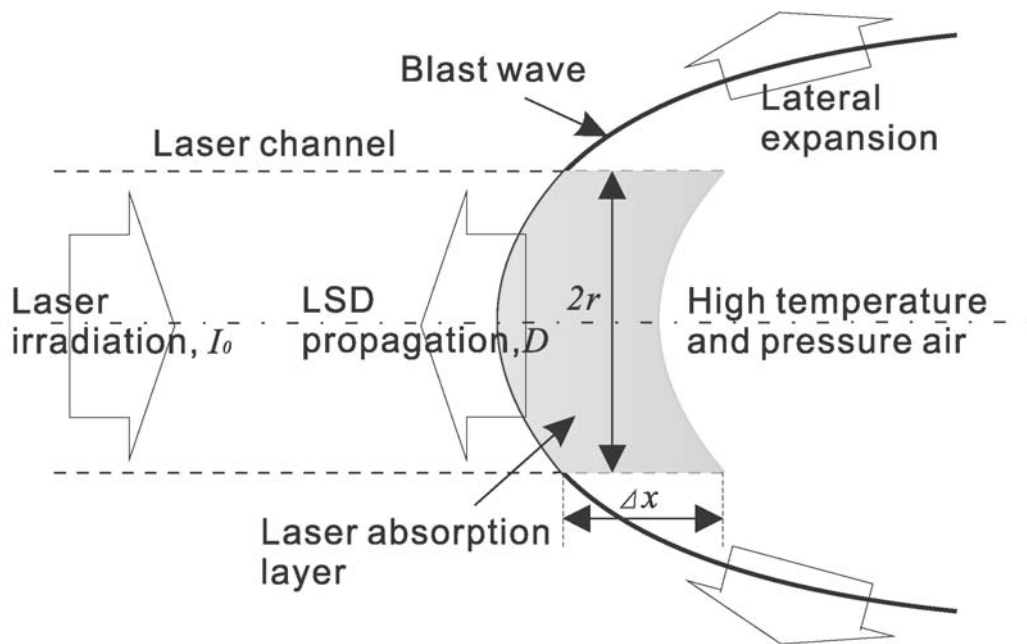


Figure 1.6: Typical LSD wave structure<sup>[27]</sup>.

As proposed in Raizer's theory<sup>[27]</sup>, LSD terminated when the energy loss on lateral wave expansion become comparable to that drive the detonation wave. To investigate this lateral expansion effect on LSD termination, a quasi-1D experiment and its corresponding 2D experiment were performed by Ushio<sup>[29]</sup>, in which LSD wave were generated by line focused laser beam on an aluminum plate. In the test, quasi-1D LSD evolution was realized by adding an aluminum wedge nozzle for confining the blast wave expansion. Results show that the LSD termination threshold in quasi-1D case is half of that gotten in 2D case. This verified that lateral expansion has great influence on the LSD termination condition as predicted by Raizer. However, because the LSD terminates during the laser pulse even there is no lateral expansion energy loss, there should have other mechanisms in dominating the LSD termination.

Another approach was done on studying the laser absorption structure in LSD wave. Distribution of its electron density was measured by 2-wavelength Mach-Zehnder interferometry in previous works<sup>[30]</sup>. The electron temperature distribution was determined by emission spectroscopy method. The result shows that electron density distribution of LSD has a peak behind shock wave (As shown in Figure 1.7). Because of its high electron density, incident laser energy can be entirely absorbed before reaching this peak (Fig. 1.8). In this way, a new electron density peak is always generating in front of the old one while laser intensity is high. In this way, this electron density peak propagates together with the shock wave at the same velocity, and high laser heating near the shock front is sustained. However, as the incident laser power becomes lower, laser absorption layer will become thicker. At the termination time, the electron density peak will not catch up with the shock wave anymore, the LSD terminated.

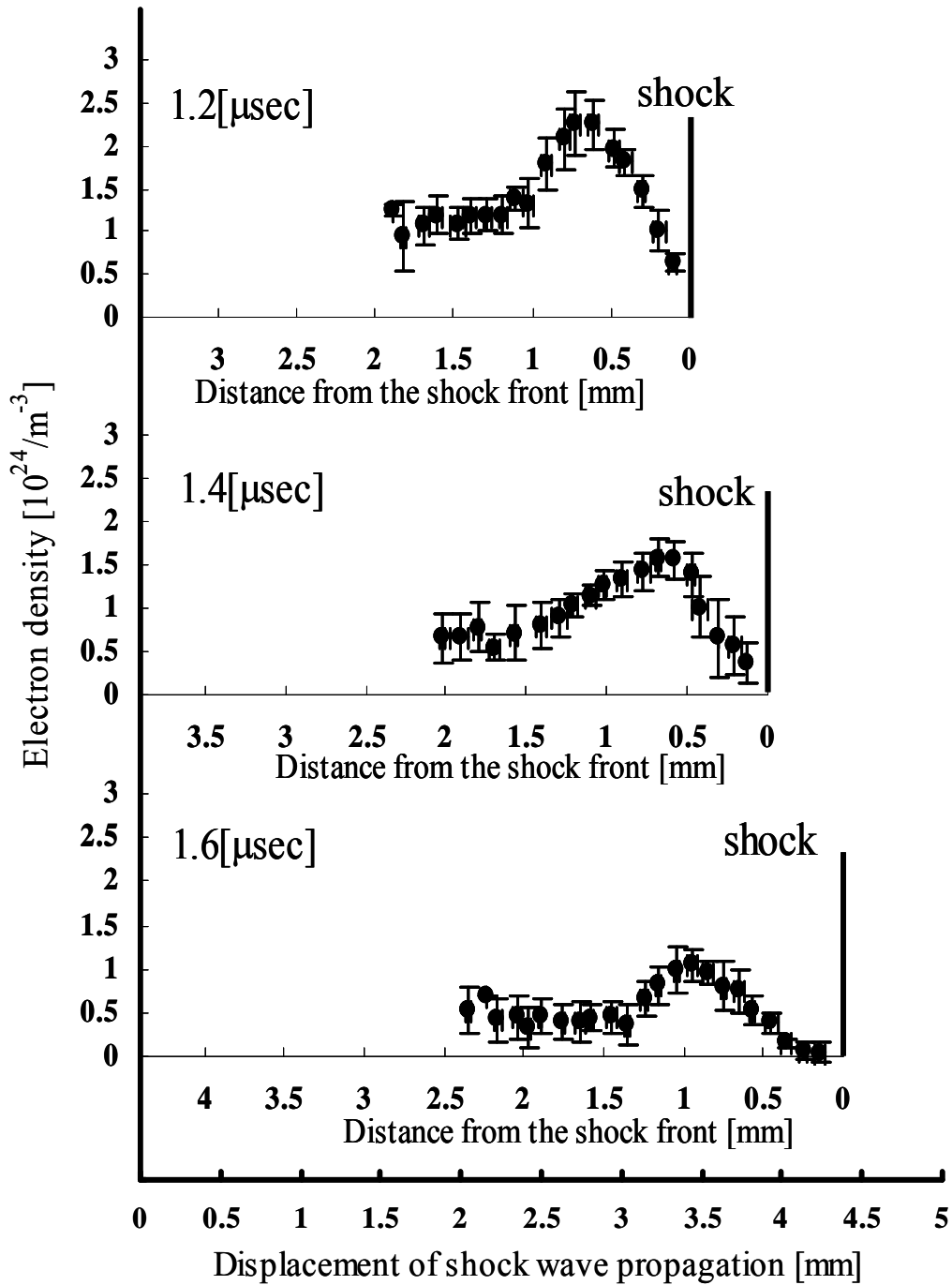


Figure 1.7: Electron density distribution around LSD termination time,  $t_{\text{term}} = 1.4 \mu\text{s}$ <sup>[30]</sup>.

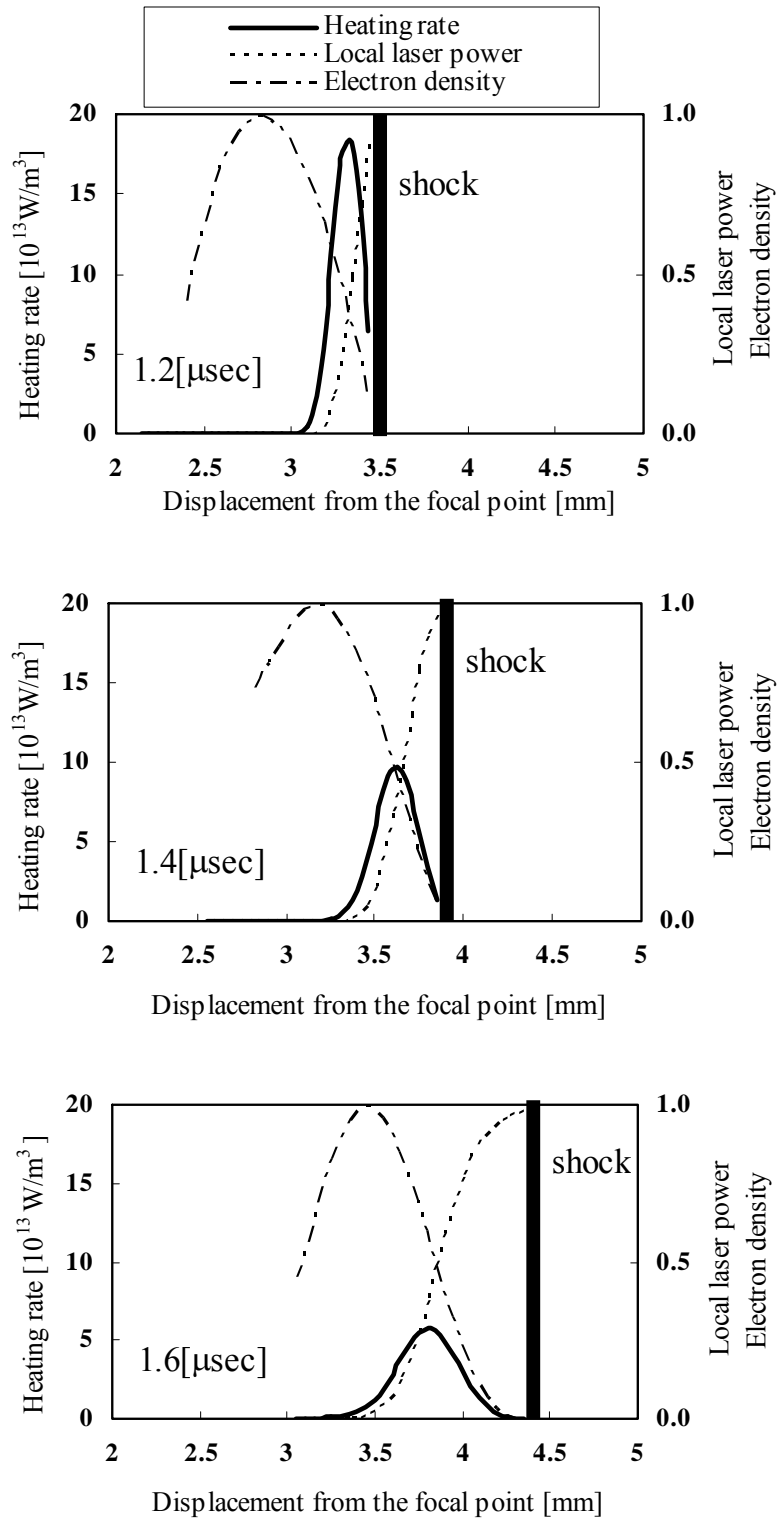


Figure 1.8: Laser heating rate and local laser energy density behind the shock wave,  $t_{\text{term}} = 1.4 \mu\text{s}$ <sup>[30]</sup>.

### *High power laser system*

Typical high power laser systems, such as a solid-state laser, a CO<sub>2</sub> laser and LDs, were rapidly developed in these years and they bring us choices for performing laser propulsion missions. Some characteristics of them are listed in Table 1.1. Many of solid-state lasers use Nd:YAG (1.06 μm) or Nd: glass (1.053 μm) as working medium. The attenuation of a laser beam in these wavelengths through the atmosphere is acceptable, around 30% to 40% in clear day. A solid state laser typically has Electro-Optical efficiency of about 20%, similarly to CO<sub>2</sub> lasers. Taking the advantage of military demands, such as Joint High Power Solid State Laser (JHPSSL) project<sup>[31,32]</sup>, its average power has reached 100 kW level with good beam quality in 2009, the same as the power achieved with a high power CO<sub>2</sub> laser. From the aspect of pulse energy, as demonstrated in the inertial confinement fusion experiment, a single pulse output up to 1.8 MJ with great beam quality was realized with joint of 192 laser beams<sup>[33,34]</sup>. For these advantages, a solid-state laser is gradually becoming the most promising laser system for laser propulsion. A pulsed CO<sub>2</sub> laser is characterized with up to 1000 J high pulse energy at a relatively low price. Its price in terms of per kW laser output is only about 20 % of those using solid-state lasers. Besides, current technology advances in diode switch and Magnetic Pulse Compression ensured that the repetition frequency could reach as high as 1k Hz, as reported by Yasuoka et al<sup>[35]</sup>. However, the combinability of multiple pulsed CO<sub>2</sub> lasers to approach higher power is poor compared with solid-state lasers. This prevents its practical application in conducting laser propulsion mission. Laser Diode array was developed for getting higher scale power output in recent times, in which laser diodes are constructed in a 2-dimensional array. It has advantage like high electrical conversion efficiency and thus easier cooling system during its operation. However, the most crucial problem for using a laser array in laser propulsion is that its beam quality is not good for long distance beam transmission.

As written in the last paragraph, the most significant advance on solid-state laser is the extremely high, MJ level, pulse energy it has reached as demonstrated by the National Ignition Facility as a result of combining 192 beams. This is due to its characteristic of good

combinability. The injection laser works like this<sup>[36]</sup>, at the very beginning, a laser pulse with a few nJ energy is generated by the master oscillator. Then with using series of fiber splitters and amplifier it is split to 48 individual pulses and each of them is amplified from about 750 pJ to energy as high as 10 J in preamplifier module (PAM) by passing through neodymium glass rods pumped by laser diodes array and flash lamps in two stages. After the preamplifier, each of 48 beams is further split to 4 beams and conditioned in the Preamplifier Beam Transport System (PABTS). Totally 192 beams are injected into the same number of amplifier beam lines. It is in which each beam is further amplified to 20,000 J of energy after traveling through laser amplifier glass slabs. In the final stage, as the energy amplification is finished, efforts are done by optical devices like special deformable mirror to ensure the combined beams have high degree of temporal and spatial precision for meeting the NIF requirements.

Table 1.1: Characteristics of high power lasers.

Laser	Solid-state	CO2	Laser Diode array
Wave length ( $\mu\text{m}$ )	1.053, 1.06,	10.6,	0.8 – 1.5
Efficiency (%)	20	20	< 70
Average power (kW)	105	100	100
Pulse energy (J)	1.8M	1k	-

### 1.3 Scope of present study

As introduced in former sections, laser detonation propulsion is a promising launch method with remarkable advantages. Many works have been done on topics like thrust performance and trajectory calculation. However, almost all of the studies concentrated on the using of CO<sub>2</sub> laser in performing this mission. There is no systematic research on the using of solid-state laser as laser power source. Recent developments on high power solid-state laser system are making it a potential candidate for fulfilling the laser propulsion requirements, this is the reason we conduct this study.

Main subject of this study is to clarify the feasibility of laser propulsion with solid-state laser. For this purpose, researches were performed following this sequence: (1) at the beginning, the laser absorption process was investigated particularly on the laser supported detonation supporting condition; (2) then, works were conducted to clarify the energy conversion process, especially on how high the blast wave energy efficiency could reach; this is of great importance because it is decisive for the final thrust performance; (3) after that, the impulse generation process was studied by way of thrust measurement on a ballistic pendulum system, to verify the obtained blast wave energy efficiency; this will give a direct evidence to prove the feasibility of laser propulsion with solid-state laser.

#### *Laser breakdown in air*

As the initiation of air-breathing laser propulsion PDE circle, focusing intense pulse laser in atmosphere air generates breakdown when the laser intensity at the focal spot reach a critical value, which have been intensively studied under various experimental conditions<sup>[37-41]</sup>. The breakdown threshold is sensitive to factors like laser specifications, focusing optics and air condition. For solid-state laser with near-infrared wavelength, the power threshold in 1 atm air is measured at the order of  $10^{10} - 10^{11}$  W/cm<sup>2</sup><sup>[41]</sup>. For Q-switched

solid-state laser, the time needed for breakdown after the laser incidence is of the same magnitude with the laser pulse width (FWHM), which has influence on the following laser absorption process. Besides, the transmission before breakdown itself is a certain amount of energy loss that should be taken into account in the energy conversion investigation.

### *Laser absorption process*

As breakdown happened, the succeeding laser energy in the same pulse is absorbed by the generated high temperature plasma. The dominant absorption mechanism is Inverse-Bremsstrahlung (IB), the process in which electron absorbs incident photon in the coulomb field of a nucleus, for both solid-state laser with near-infrared wavelength<sup>[42]</sup> and CO<sub>2</sub> laser at laser power intensities of  $10^9 - 10^{11}$  W/cm<sup>2</sup>.

It is well known that the laser absorption wave has two regimes. One is the Laser Supported Detonation (LSD) wave<sup>[43-45]</sup> occurs at laser power density higher than the order of  $10^7$  W/cm<sup>2</sup>. The other is Laser combustion (LSC) regime happens when the power density is lower than  $10^6$  W/cm<sup>2</sup>. These regime transfer threshold is gotten with CO<sub>2</sub> laser.

In LSD regime, the laser absorption area propagates together with the blast wave. It is in this regime that the absorbed laser energy could be efficiently used to drive a high pressure blast wave in the surrounding air through the expansion of plasma. In other words, the energy can be efficiently converted to the motion of air. As the laser power decreases to a certain threshold, the LSD regime transits to LSC regime, in which the propagating blast wave separates from the plasma as shown in Figure 1.9. Because the laser heating can not affect the blast wave anymore, the blast wave expands adiabatically in this post-LSD regime. The laser energy absorbed in LSC regime is thought to convert to the internal energy frozen in the plasma region or radiation energy emitted from the plasma.

Because it is only in the LSD regime that efficient energy conversion happens, study on how much of the laser energy is irradiated in this regime is of great importance for finding method to enhance the laser propulsion thrust performance. LSD wave efficiency  $\eta_{\text{LSD}}$  is introduced to express the fraction of laser energy that absorbed during the LSD regime.

Previous researchers studied CO<sub>2</sub> laser induced LSD wave from the aspects like its termination condition<sup>[28,30]</sup> or propagation velocities. By now, there is no systematic investigation show the information on using solid-state laser with near-infrared wavelength, which should be different from that gotten in CO<sub>2</sub> laser case due to the difference on their IB absorption coefficient.

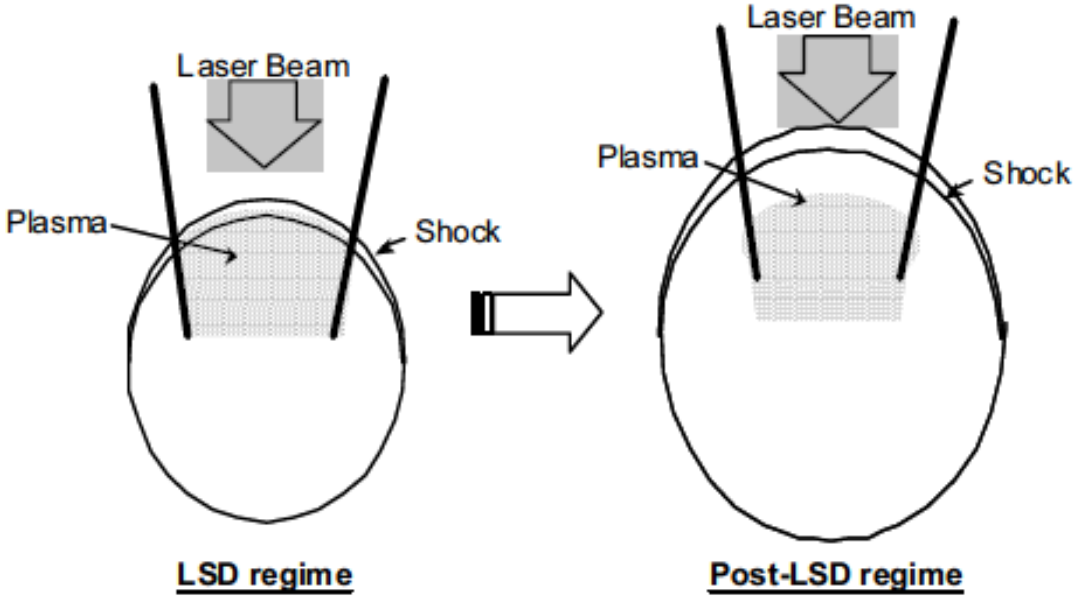


Figure 1.9: Schematic of regime transition from LSD to LSC.

*Blast wave energy conversion process*

The fast propagation of plasma supported by laser beam drives a blast wave expands to surrounding ambient air, which results in the rising on motion of the air. The blast wave energy is defined as the source energy necessary to drive an equivalent blast wave in a calorically perfect gas.

In laser propulsion study, how much of the absorbed laser energy could be converted to that of the blast wave and generate thrust is of primary importance. For evaluating this conversion, conversion efficiency is defined as the fraction of blast wave energy  $E_{bw}$  to the incident laser pulse energy  $E_i$ .

$$\eta_{bw} \equiv \frac{E_{bw}}{E_i} \quad (1-4)$$

The evolution of adiabatically spherical blast wave expansion could be approached by Sedov–Taylor similarity solutions<sup>[46-48]</sup>. And for cylindrical geometry, notable analytical solution is introduced by Sakurai<sup>[49,50]</sup>. Brode<sup>[51]</sup>, Friedman<sup>[52]</sup> provided numerical solutions described the more realistic case of initially isothermal high pressure gas explosions. Leonard and Mayer<sup>[53]</sup> estimated the blast wave energy  $E_{bw}$  by comparing the wave arrival time with Brode’s spherical computational results.

Because of the rapid moving on energy absorption structure, the LSD wave, the shape of laser induced blast wave is irregular rather than a sphere, which is especially true at its initial stage. Mori proposed a calculation method to estimate the pulsed TEA-CO<sub>2</sub> laser induced elliptical expansion blast wave energy. The efficiency  $\eta_{bw}$  estimated is 0.47 for focusing number of 2.2 and 0.44 for focusing number of 3.3, which are not sensitive with the pulse energy. By now there is no such research on near-infrared Q-switched laser induced blast wave.

### *Impulse generation*

The impulse generation process is important for the laser propulsion thrust performance. The momentum coupling coefficient  $C_m$  is a key factor to value this thrust performance. As defined in previous section,  $C_m$  is a function of impulse and input pulse energy. The energy conversion efficiency  $\eta_{bw}$  is a decisive factor for impulse and thus for  $C_m$ . A high  $\eta_{bw}$  with solid-state laser will show the possibility of getting the same level of  $C_m$  for a laser detonation thrust as that obtained in the CO<sub>2</sub> laser case, which is usually about 0.3 mNs/J. Therefore, by comparing the  $C_m$  gotten in solid laser thrust measurement experiment with that gotten with CO<sub>2</sub> laser, the calculated  $\eta_{bw}$  could be verified. By now, there is no such result reported yet with the use of Nd: Glass laser or other lasers in micrometer level wavelength. Thus, an impulse measurement experiment is conducted in this part to measure this thrust performance.

Besides, because the nozzle geometry has great influence on the thrust performance, it is

also necessary to investigate the relation between the nozzle size and the impulse thrust for thrust optimization. Both results will be solid evidence for showing the feasibility of performing laser propulsion with solid-state laser.

## 1.4 Objectives

- Determine the supporting and termination conditions of a solid-laser induced detonation wave.
- Develop a method to estimate the energy conversion efficiency from laser energy to blast wave energy for a solid-laser induced blast wave.
- Clarify the energy conversion process and its dependency on ambient pressures.
- Measure the impulsive thrust in a cone nozzle to validate the measured energy conversion efficiency and study its dependency on thruster geometry.

## References

- 1) Harron, R. J., Wadle, R. C., *Solar power satellite cost estimate*, NASA-TM-58231, January 1981
- 2) Cohen, M. M., *Mobile Lunar Base Concepts*, AIP Conf. Proc., Vol. 699, February 4, 2004 pp. 845-853.
- 3) Nishioka, K., Arno, R. D., Alexander, A. D., and Slye, R. E., "Feasibility of Mining Lunar Resources for Earth Use: Circa 2000 A.D., vols. I, II," vol. 1, NASA TM X-62, 267; vol. 2, NASA TM X-62, 268, 1973.
- 4) *Reducing Space Mission Cost*, ed. by Wertz, J., and Larson, W., Kluwer Academic Publishers, Boston, 1996.
- 5) *The Space Shuttle Decision: NASA's Search for a Reusable Space Vehicle*, ed by Heppenheimer, T. A., NASA SP-4221, Washington, D.C. 1999
- 6) Pielke, Jr., R. A., *Book Review for "Final Countdown: NASA and the End of the Space Shuttle Program" by Pat Duggins*, American Scientist, Vol. 96, No. 5, p. 32, 2008
- 7) Berning, P.R., Hummer, C. R., Hollandsworth, C. E., A coilgun-based launch system, IEEE Transactions on Magnetics, Vol. 35, issue 1, pp. 136-141.
- 8) Turman, B. N., Lipinski, R. J., Electromagnetic coilgun launcher for space applications, AIP Conf. Proc. 361, 703, 1996.
- 9) Zana, L. M., "Rail Accelerator for Space Transportation," NASA Technical paper, 2571, 1986.
- 10) Parker, J. V., *Electromagnetic projectile acceleration utilizing distributed energy sources*, J. Appl. Phys. Vol. 53(10), 6710, 1982.
- 11) Burton, R. L., Witherspoon, F. D., and Goldstei, S. A., *Performance of a self-augmented railgun*, J. Appl. Phys. Vol. 70, 3991, 1991.
- 12) Kantrovitz, A. "Propulsion to Orbit by Ground Based Lasers," *Aeronautics and Astronautics*, vol.10, 1972, pp. 74-76.
- 13) Katsurayama, H., Ushio, M., Komurasaki, K., and Arakawa, Y. Feasibility for the Orbital Launch by Pulse Laser Propulsion. *Journal of Space Technology and Science* 2005; **20**(2):32-42.
- 14) Komurasaki, K., and Wang, B., *Encyclopedia of Aerospace Engineering*, R. Blockley and W. Shyy (eds). John Wiley & Sons Ltd, Chichester, UK, (2010), pp 1351-1360.
- 15) Sasoh, A., Jeung, I.S., and Choi, J.Y. Access to Space without Energy and Propellant on Board. *Beamed Energy Propulsion: Fifth International Symposium on Beamed Energy Propulsion*, AIP Conference Proceedings, Vol. 997, 2007, pp. 37- 46.
- 16) Myrabo, L. N., "Highways of Light," *The Future of Space Exploration* by Scientific American (1999), pp.66-67.
- 17) Libeau, M., Myrabo, L., "Off-Axis and Angular Impulse Measurements on a Lightcraft Engine," *Beamed Energy Propulsion: Third International Symposium on Beamed Energy Propulsion*, AIP Conference Proceedings, Vol. 766, 2005, pp. 166-177.
- 18) Minovich, M. A., "Reactorless Nuclear Propulsion – The Laser Rocket," AIAA 72-1095, *AIAA/SAE 8<sup>th</sup> Joint Propulsion Specialist Conference*, December 1972.

- 19) Toyoda, K., Komurasaki, K., and Arakawa, Y., "Thrust Performance of a CW Laser Thruster in Vacuum," *Vacuum*, Vol. 65, Nos. 3-4, 2002, pp. 383-388.
- 20) Phipps, C.R., Luke, J.R., Helgeson W., and Johnson, R., "Performance Test Results for the Laser-Powered Microthruster," *Beamed Energy Propulsion: Fourth International Symposium on Beamed Energy Propulsion*, AIP Conference Proceedings, Vol. 830, May 2, 2006, pp. 224-234.
- 21) Bohn, W.L. and Schall, W.O., "Laser Propulsion Activities in Germany," *Beamed Energy Propulsion: First International Symposium on Beamed Energy Propulsion*, AIP Conference Proceedings, Vol. 664, 2002, pp. 79-91.
- 22) Pirri, A. N., Monsler, M. J. and Nebolsine, P. E. Propulsion by Absorption of Laser Radiation. *AIAA Journal* 1974; **12**: 1254-1261.
- 23) Tang, Z., Gong, P., and Hu, X., "Experimental Investigation on Air- Breathing Mode of Laser Propulsion," *Beamed Energy Propulsion: Second International Symposium on Beamed Energy Propulsion*, AIP Conference Proceedings, Vol. 702, 2003, pp. 23-30.
- 24) Mori, K., Sasoh, A., and Myrabo, L.N., "Experimental Investigation of Airbreathing Laser Propulsion Engines: CO<sub>2</sub> TEA vs. EDL," *Beamed Energy Propulsion: Third International Symposium on Beamed Energy Propulsion*, AIP Conference Proceedings, Vol. 766, 2005, pp. 155-165.
- 25) Myrabo, L. N., Messitt, D. G., and Mead, F. B. Jr., "Ground and Flight Tests of a Laser Propelled Vehicle," AIAA Paper 98-1001, Reno, 1998.
- 26) Myrabo, L. N., "Brief History of the Lightcraft Technology Demonstrator (LTD) Project," *Beamed Energy Propulsion: First International Symposium on Beamed Energy Propulsion*, AIP Conference Proceedings, Vol. 664, 2002, pp. 49-60.
- 27) Raizer, Y.P., "*Laser-Induced Discharge Phenomena*," Studies in Soviet Science. Consultants Bureau, New York, 1977.
- 28) Mori, K., Komurasaki, K. and Arakawa, Y., *J. Appl. Phys.* **95**, 5979 (2004)
- 29) Ushio, M., Komurasaki, K., Kawamura, K., Arakawa, Y., *Shock Waves* (2008) 18:35-39.
- 30) Wang, B., Yamaguchi, T., Hatai, K., Komurasaki, K., Arakawa, Y., *AIP Conference Proceedings*, Vol. 1230, Arizona, USA, 2010, pp. 137-147
- 31) Marmo, J., Injeyan, H., Komine, H., McNaught, S., Machan, J. and Sollee, J., Joint high power solid state laser program advancements at Northrop Grumman, *Proc. SPIN* 7195, 719507, 2009.
- 32) Bohn, W. L., Long range laserpropagation: power scaling and beam quality issues, *Proc. SPIE* 7751, 775127, 2010.
- 33) Haynam, C. A., Wegner, P. J., Auerbach, J. M., et al, National Ignition Facility laser performance status, *Applied Optics*, Vol. 46, Issue 16, pp. 3276-3303, 2007.
- 34) Moses, E, National Ignition Facility: 1.8-MJ 750-TW ultraviolet laser, *Proc. SPIE* **5341**, 13, 2004.
- 35) Yasuoka, K., Ishii, A., Tamagawa, T., and Ohshima, I., "Newly developed excitation circuit for kHz pulsed lasers," *Proceedings of SPIE*, Vol. 1412, 1991, pp. 32-37.
- 36) Sawicki, R. H., The National Ignition Facility: laser system, beam line design, and construction , *Proc. SPIE* **5341**, 43, 2004.
- 37) Tomlinson, R.C., Damon E.K., and Buscher H.T. in "Physics of Quantum Electronics" Edited by Kelley, Lax and Tannenwald, McGraw-Hill, New York (1966).

- 38) D.C. Smich, *Appl. Phys. Lett.* 19, 405 (1971)
- 39) D. E. Lencioni, *Appl. Phys. Lett.* 23, 12 (1973)
- 40) C.H.Chan, C.D.moody and W.B.McKnight, *J.Appl.Phys.* 44, 1179 (1973)
- 41) P. Woskoboinikow, W.J.Mulligan, H.C.Praddaude and D.R.Cohn, *Appl. Phys. Lett.* 32, 527 (1978)
- 42) D. Breitling, H. Schittenhelm, P. Berger, F. Dausinger, and H. Hügel, *Applied Physics A.* **69**, S505–S508 (1999)
- 43) Fischer, V. I., *Soviet Physics: Technical Physics*, Vol.28, 1984
- 44) Nielsen, P. E., “Hydrodynamic calculations of surface response in the presence of laser-supported detonation weaves,” *Journal of Applied Physics*, Vol. 46, 1975, pp. 4501-4505
- 45) Jumper, E. J., *Physics of Fluids*, Vol.21, 1978, p. 549
- 46) Zel'dovich, Y. B., and Raizer, Yu. P., *Physics of Shock waves and High-temperature Hydrodynamics Phenomena*, Dover, NewYork, 2002, Chap. I.
- 47) G. F. Kinney, *Explosive Shocks in Air*, Macmillan, New York, 1962, p. 75.
- 48) Sedov, L. I., *Similarity and Dimension Methods in Mechanics*, Academic Press, New York, 1959.
- 49) A.Sakurai, *J. Phys. Soc. Jpn.* 8, 662 (1953).
- 50) A.Sakurai, *J. Phys. Soc. Jpn.* 9, 256 (1954).
- 51) Brode, H. L., *Journal of Applied Physics*, Vol.26, 1955, p. 766
- 52) Friedman, M.P., *J. Fluid Mech.* 11, 1-15 (1961)
- 53) Leonard, T. A., and Mayer, F. J., *Journal of Applied Physics*, Vol.46, 1975, p. 3562.

## Chapter 2

# SUPPORTING CONDITIONS OF LASER DETONATION

In laser detonation propulsion, the laser energy only absorbed during laser supported detonation regime could be efficiently converted to that of the blast wave. Therefore, the supporting and termination conditions of LSD wave are important. The conditions are greatly influenced by laser parameters such as wave length, pulse profile and optical focusing number (defined as focal length / laser beam diameter). For a typical Q-switched Nd:Glass laser, it's oscillating at 1.053  $\mu\text{m}$  wavelength and the pulse width is in the order of 10 ns.

Past researches have been focused on the propagation velocity and regime conversion threshold of LSD using a CO<sub>2</sub> laser. By now, there is no systematic research has been conducted on that of solid-state laser induced laser detonation waves. In this chapter, an improved half shadowgraph half self-emission method is introduced to visualize the LSD wave evolution clearly. The pulse energy during the experiment changed from 1.0 J to 2.0 J for investigating the influence of the laser conditions on LSD threshold.

## 2.1 Experimental apparatus and methods

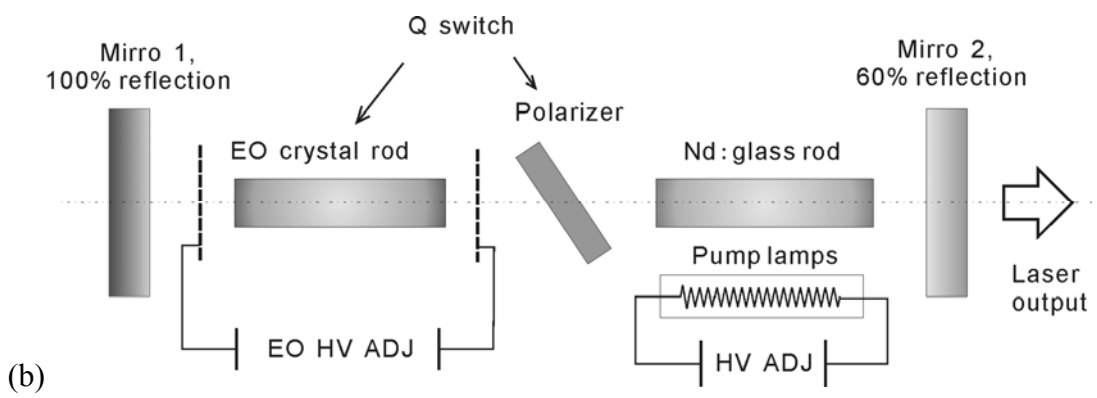
### *Laser and focusing optics*

The laser used in our experiment is a Q-switched Neodymium glass (Nd:glass) laser made by EOR company. Its principle diagram is shown schematically in Fig. 2.1. Besides, Table 2.1 summarized its specifications. The rod is pumped by two linear Xenon flash-tubes within a double ellipse reflector configuration. The flash lumps and laser rod are water-cooled for thermal stability. Single pulse energy is adjustable to reach a maximum output of 2.0 J, by changing the discharge voltage on the flash lumps (HV ADJ). The shot-to-shot pulse energy fluctuation was maintained below 2% throughout the experiments, as real time monitored by an energy meter made by Gentec Electro-Optics (QE25LP-S-MB, Figure 2.2, Table 2.2).

The laser oscillation wave length is  $\lambda=1.053 \mu\text{m}$ , 1/10 of the wavelength of TEA CO<sub>2</sub> laser. In addition, the pulse width is also adjustable in a certain range, from 20 to 40 ns full width at half maximum (FWHM), with the help of a resistance added to the discharge electric circuit. In our experiments, the pulse width was fixed at 33 ns, with an error of  $\pm 1$  ns, for all experiments that performed.



(a)



(b)

Figure 2.1: The Nd:glass laser, (a) its photo and (b) principle diagram.

Table 2.1: Specification of the Nd:glass laser.

Specifications	Nd: Glass laser
Wavelength	1.053 $\mu\text{m}$
Pulse width (FWHM)	20 ~ 40 ns
High voltage on flash lamp	0 ~ 2 kV
Pulse energy $E_i$ ,	Up to 2.0 J
$E_i$ fluctuation	$< \pm 2\%$
Beam cross-section	$r = 5\text{mm}$ round
Repetition	Single, about 0.01 Hz



Figure 2.2: Energy meter QE25LP-S-MB.

Table 2.2: Specification of energy meter.

Model	QE25LP-S-MB
Maximum Measurable Energy	Alone: 3.8 J With attenuator: 20J
Active Area	25 mm x 25 mm square
Repetition Rate	300 Hz
Noise Equivalent Energy	4 $\mu$ J
Sensitivity	10 V/J
Maximum Pulse width	400 $\mu$ s
Repeatability	< 0.5 %
Rise time	550 $\mu$ s

### *Pulse shape*

Temporal laser power profiles for  $E_i = 1.0$  and  $2.0$  J pulse energy were measured using a photodetector (ET-2030; Electro Optics Technology, Inc., Figure 2.3) with rising time as short as  $0.3$  ns. The photodetector specifications are summarized in Table 2.3.

As presented in Figure 2.4, the laser pulse consisted of a leading spike and a following exponentially decaying tail, which is typical for a Q-switched solid-state laser, lasting around  $900$  ns. The FWHM of the pulse was  $33 \pm 1$  ns for all experimental conditions. From the aspect of cumulative energy, about  $62\%$  of all pulse energy is irradiated in the first  $66$  ns (double the FWHM pulse width). The remaining part of the pulse energy ( $38\%$ ) was contained in the tail, which was found also important for the energy conversion process. As displayed in log-scale, Figure 2.5 clearly shows the temporal power changing on the decaying tail,  $E_i = 1.0$  J.

The temporal laser power change can be approximated by a sectional fitting of two functions. For the power at the leading spike  $P_{spike}(t)$ , a Gauss function can be applied as

$$P_{spike}(t) = \frac{A}{w\sqrt{\pi/2}} \exp\left(-\frac{2(t-t_c)^2}{w^2}\right) \quad (2-1)$$

besides, the temporal change of power at the tail was approximated as

$$P_{tail}(t) = P_{0,tail} \left[ A_1 \exp\left(-\frac{t}{\tau_{d1}}\right) + A_2 \exp\left(-\frac{t}{\tau_{d2}}\right) \right] \quad (2-2)$$

for  $E_i = 1.0$  J,  $P_{0,tail}=54.21$  MW, the decay-constants  $\tau_{d1}$  and  $\tau_{d2}$  were  $24.48 \pm 0.02$  ns and  $226.74 \pm 0.16$  ns, the factor  $A_1$  and  $A_2$  were  $0.967 \pm 0.023$  and  $0.033 \pm 0.001$ , respectively. For  $E_i = 2.0$  J,  $P_{0,tail}=47.87$  MW, the decay-constants  $\tau_{d1}$  and  $\tau_{d2}$  were  $32.44 \pm 0.45$  ns and  $492.10 \pm 11.20$  ns, the factor  $A_1$  and  $A_2$  were  $0.978 \pm 0.027$  and  $0.022 \pm 0.001$ , respectively. In the equations,  $t = 0$  means the starting of laser irradiation. The pulse shapes were monitored during the experiments.



Figure 2.3: Photodetector

Table 2.3: Specifications of photodetector (Electro-Optics Technology, Inc.).

Model No.	ET-2030
Detector Type	PIN
Risetime	< 300 ps
Falltime	< 300 ps
Responsivity @830nm	0.4A/W
Acceptance Angle (1/2 Angle)	30°
Active Area	0.4 mm diameter
Cut Off Frequency (into 50Ω)	>1.2GHz

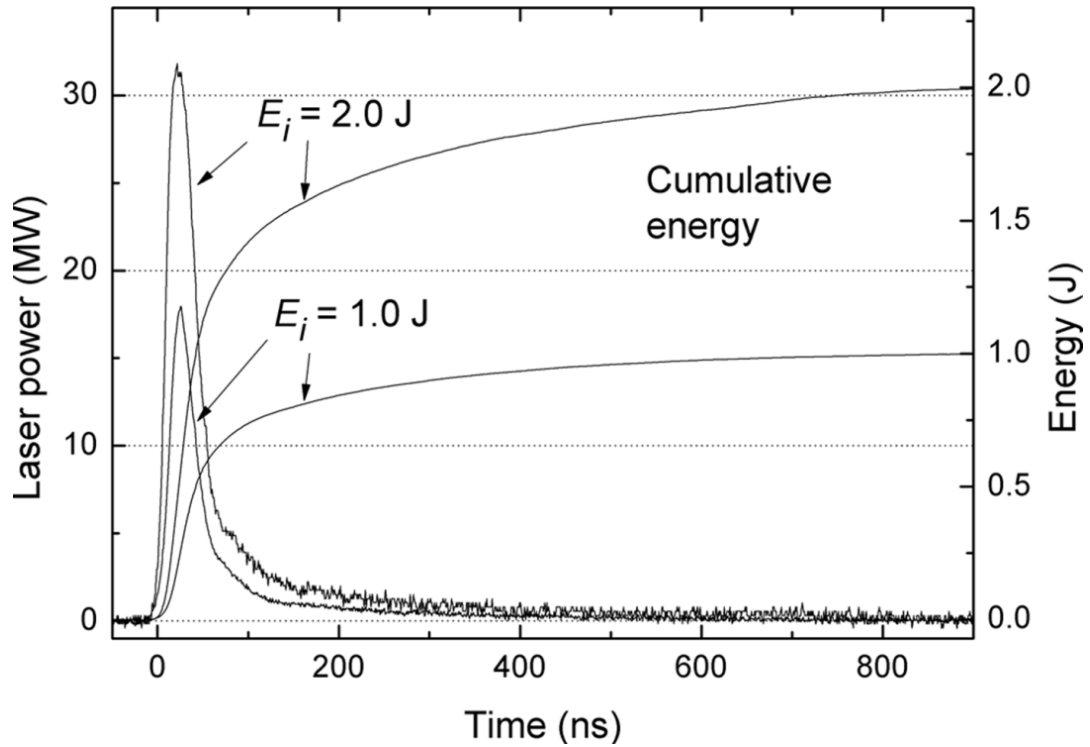


Figure 2.4: Laser pulse shape and cumulative energy for  $E_i = 1.0$  and  $2.0$  J.

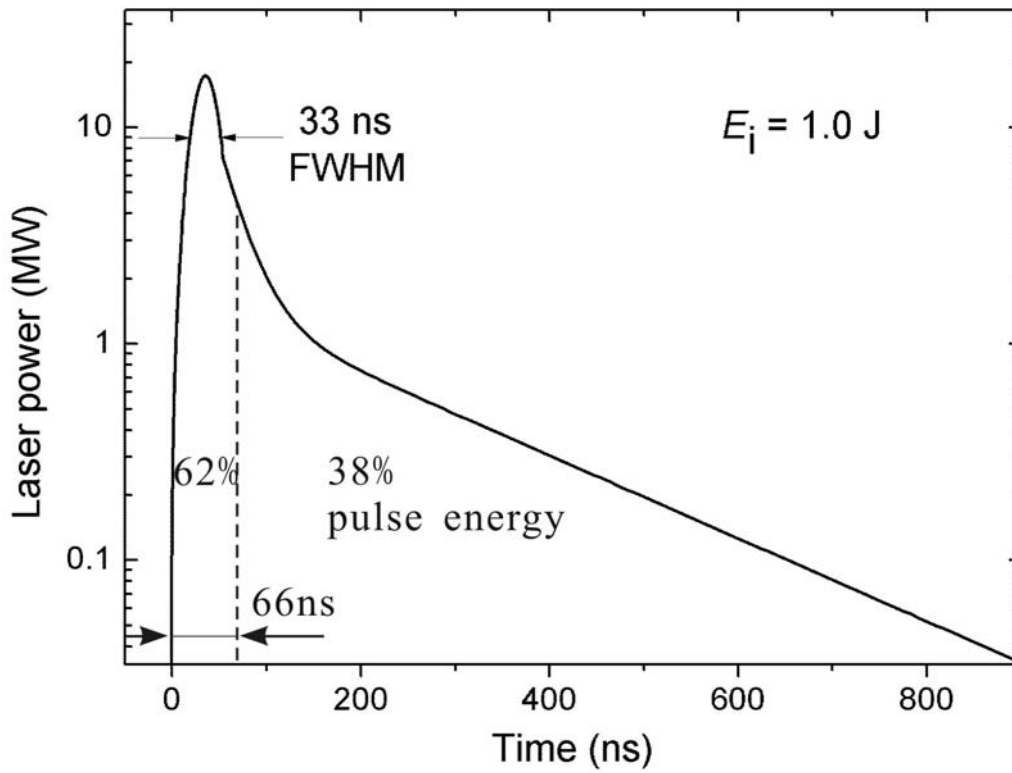


Figure 2.5: Laser power in log-scale, pulse width 33 ns.

### Power distribution on a beam cross section

The burn pattern of laser pulse was gotten by shooting laser on an energy paper, as shown in Figure 2.6. It is in high-order multi-transverse mode. The transverse mode is center symmetry, a circle of 5 mm radius. To study its power profile on this cross section, the beam was expanded by a concave lens to a circle with the radius of 15 cm. Energy meter was mounted on a rail and detect the cumulative energy at different positions along a selected radial direction. More than 5 shots were output at each position to clarify the power fluctuation.

As a result, the power distribution is presented in Figure 2.7, which shows that after adjustment, the laser has an even output in the circle area of about  $r < 3.5$  mm. Then it decreased with the increase of distance from the center and the power become 0 at about  $r=5$ mm.

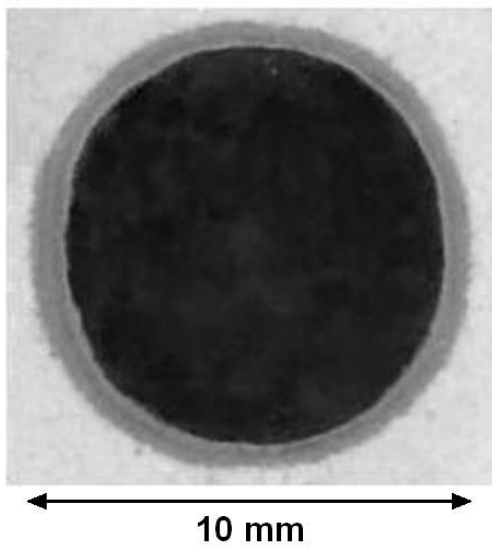


Figure 2.6: Laser burn pattern gotten with energy paper.

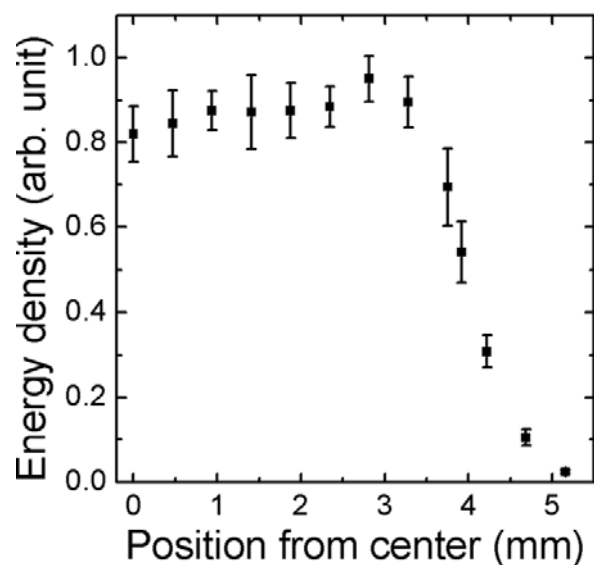


Figure 2.7: Laser transverse mode.

### *Ambient air control*

All the experiments were performed in atmosphere air, while the temperature was kept in the range of 293~276 K with air conditioner. The humidity was also monitored during the test, in the range of 50% ~ 60%, to ensure the reproducibility of experimental data.

### *Focusing lens*

Considering the relative high breakdown threshold intensity in air with near-infrared laser (in the range from  $10^{10}$  to  $10^{11}$  W/cm<sup>2</sup>), the focusing optical element used in the experiment is an aspheric lens named as GRADIUM lens made by LightPath company, its focal length  $f = 62.7$  mm, which bring us a focusing number of 6.27. It has unique refractive index profile that the rays are gradually bended while traveling through it, resulting in a better focused smaller spot.

### *Visualizing system*

Figure 2.8 portrays the arrangement of the shadowgraph experiment. The output laser beam is first separated by a beam splitter (BS). The minor energy one, which containing 3.9% of total pulse energy, passes through the splitter and received by a energy meter, while the major energy one that containing 96.1% of the pulse energy is focused in air using the aspheric lens with 62.7 mm focal length.

A continuous wave YAG laser ( $\lambda = 532$  nm) with 8 mW output power was used as a probe light. It projects the shadow of a blast wave on a high-speed ICCD camera (Figure 2.9, Ultra 8; DRS Technologies Inc.) which can take eight frames in each operation at the maximum framing rate of 100 million FPS with minimum exposure time of 10 ns.

The triggering consequence works like this, first, an external trigger output by the Nd: glass laser at the time of HV discharge. Then, this signal is transmitted to a delay-circuit (Stanford Research Systems, Inc., Digital Delay/Pulse Generator Model DG535, Figure 2.10), which allows settings like adding a delay or regulating this received triggering signal. After a

signal conditioning, it is transmitted to trigger the camera. Synchronization between the breakdown and the photographing is realized. A photodetector is placed to receive the emission of laser induced plasma during the experiment. By this arrangement, the timing of breakdown could be figured out. Besides of the pulse generator, it is also possible to set an additional delay on the camera control window.

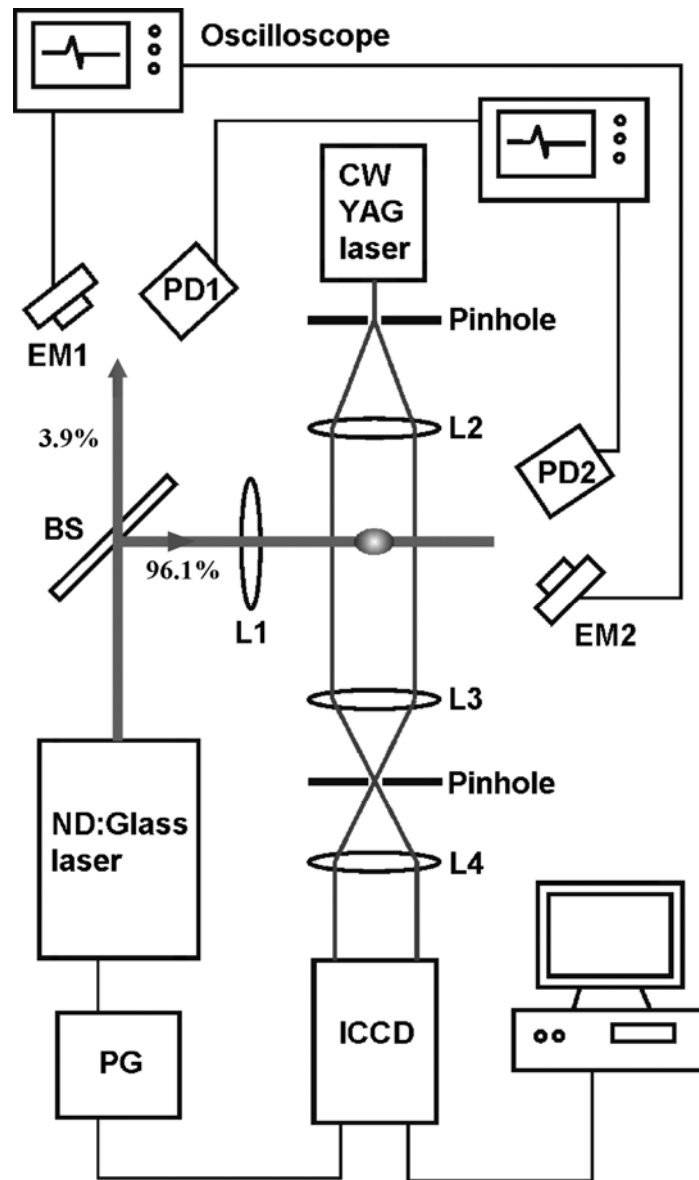


Figure 2.8: Schematic of the experimental setup for shadowgraph measurement. (PD1, PD2, photodetectors; EM1, EM2, energy meters; L1, high-energy laser focusing lens; L2, L3, L4, lenses; BE, beam expander; PG, pulse generator; ICCD, intensified CCD high-speed camera).



Figure 2.9: Ultra 8 high speed camera.



Figure 2.10: Pulse generator, Stanford Research Systems, Inc. DG535.

### *Half-shadowgraph-half-self-emission*

The termination time of LSD is the time when the propagating of ionization front separated from that of the shock wave on the laser beam axis. In previous researches<sup>[1-3]</sup>, the propagation history of the ionization front is obtained from the self-emission of the plasma. However, this is not quite clear especially under the disturbance of the probe light illumination.

An improvement was made on the visualizing experiment setup, which is schematically shown in Figure 2.11 (a). Considering of the symmetry of LSD wave, half of the probe light is blocked by a plate, to take off the influence of a probe light, means a plasma self-emission experiment. For the other half, in opposite, a band pass filter at  $\lambda = 532 \mu\text{m}$  (corresponding to the probe laser wavelength) is used to block most of the strong radiation from the plasma, to get a clear figure of the blast wave, means a shadowgraph experiment.

With this arrangement, the separation between the ionization front and the shock wave could be clearly figured out in one experimental operation. A picture gotten is given in Figure 2.11 (b). In this figure, the ionization front could be figured out from the left half plasma self-emission, while the shock wave could be gotten from the right half shadowgraph image. This method is designated as a Half-Shadowgraph-Half-Self emission (HSHS) experiment, to distinguish it from the conventional shadowgraph experiment. With this method, the shadowgraph and the plasma self-emission experiments could be conducted synchronously. Consequently, the evolution history of an ionization front and a shock wave can be measured precisely. The temporal and spatial resolutions were, respectively, 10 ns and 0.1 mm during the experiment.

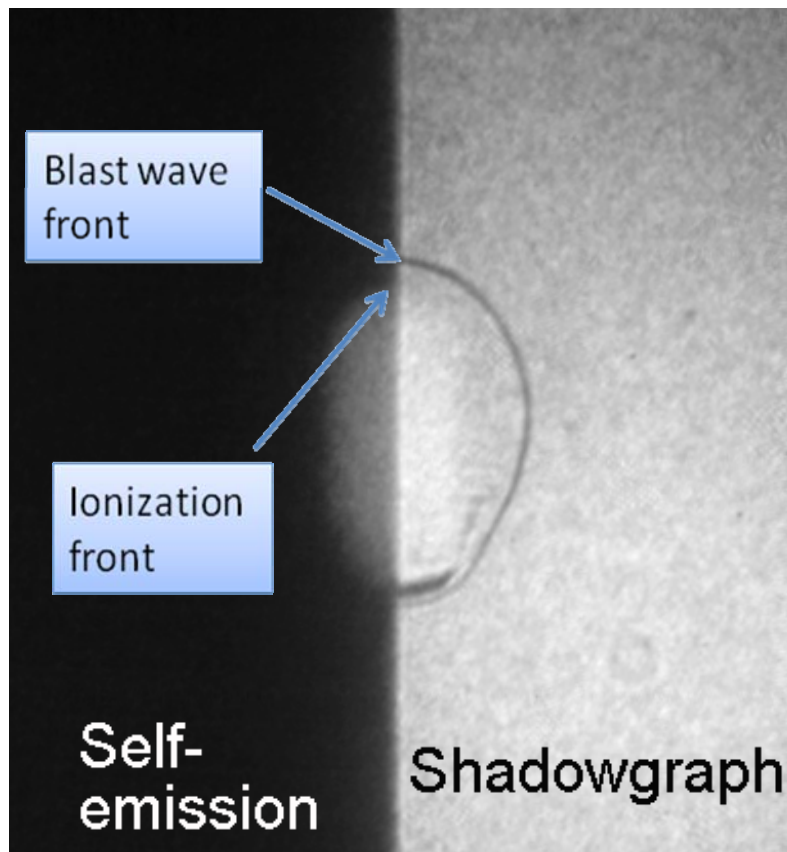
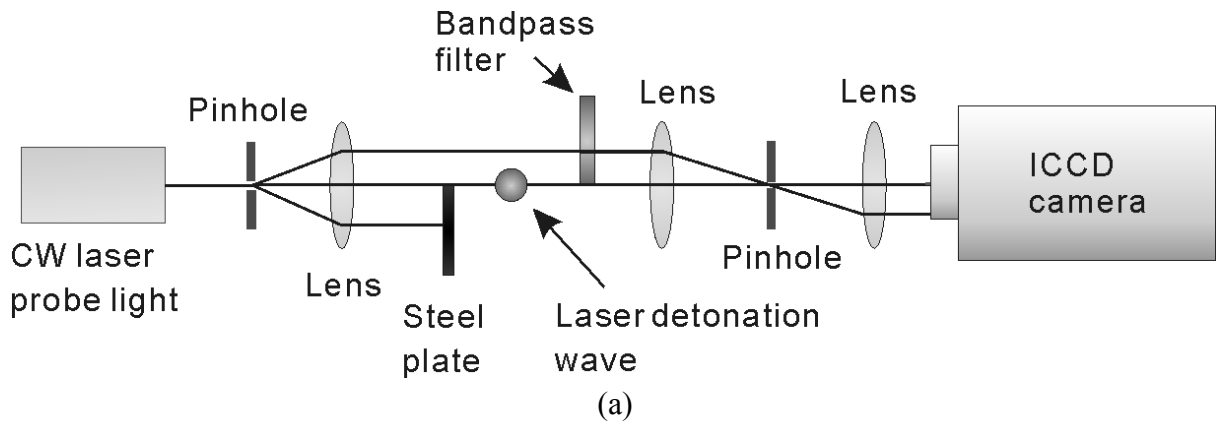


Figure 2.11: (a) Setup of Half-Shadowgraph-Half-Self emission (HSHS) experiment and (b) a picture taken with this arrangement,  $E_i = 1.0 \text{ J}$ ,  $f = 6.27$ .

## 2.2 Results and discussions

### *Shadowgraph images*

The pictures in Figure 2.12 are shadowgraphs taken in the HSHS experiment, for the case of  $f=6.27$  and  $E_i = 2.0$  J in atmospheric air.

The laser pulse started to irradiate in the picture at  $t = 0$  s.  $t$  is defined as an elapsed time from ignition. Breakdown happened at the focal point when the laser intensity reached the breakdown threshold. Luminous plasma could be seen. After that, at  $0 < t < 450$  ns, it is Laser Supported Detonation (LSD) regime, during which the luminous plasma front and shock wave propagate together along the laser channel. Due to the high laser intensity on the LSD wave front, the propagation velocity at the initial stage, like  $0 < t < 20$  ns, could reach  $>200$  km/s. It is seen that different from the one direction LSD propagation observed in the CO<sub>2</sub> laser case <sup>[4,5]</sup>, the glass laser induced LSD waves traveling both the upstream and downstream along the laser channel. This two-direction LSD propagation is schematically shown in Figure 2.13. The existence of LSD wave propagation in the downstream area indicates that laser beam absorption is not perfect in the upstream LSD during the glass laser induced LSD which will be more precisely studied in the next chapter. In contrast, for CO<sub>2</sub> laser case, the laser beam could be completely absorbed in a thin layer in LSD regime, attributed to its high laser absorption coefficient. <sup>[6]</sup>

At  $400 < t < 900$  ns, as the laser power decayed, the separation between shock wave front and plasma front separated in both directions, means the termination of LSD regime. The blast wave expands adiabatically in Laser Supported Combustion (LSC) regime because the separated plasma could not drive the blast wave anymore. The plasma luminous becomes weak as time goes by.

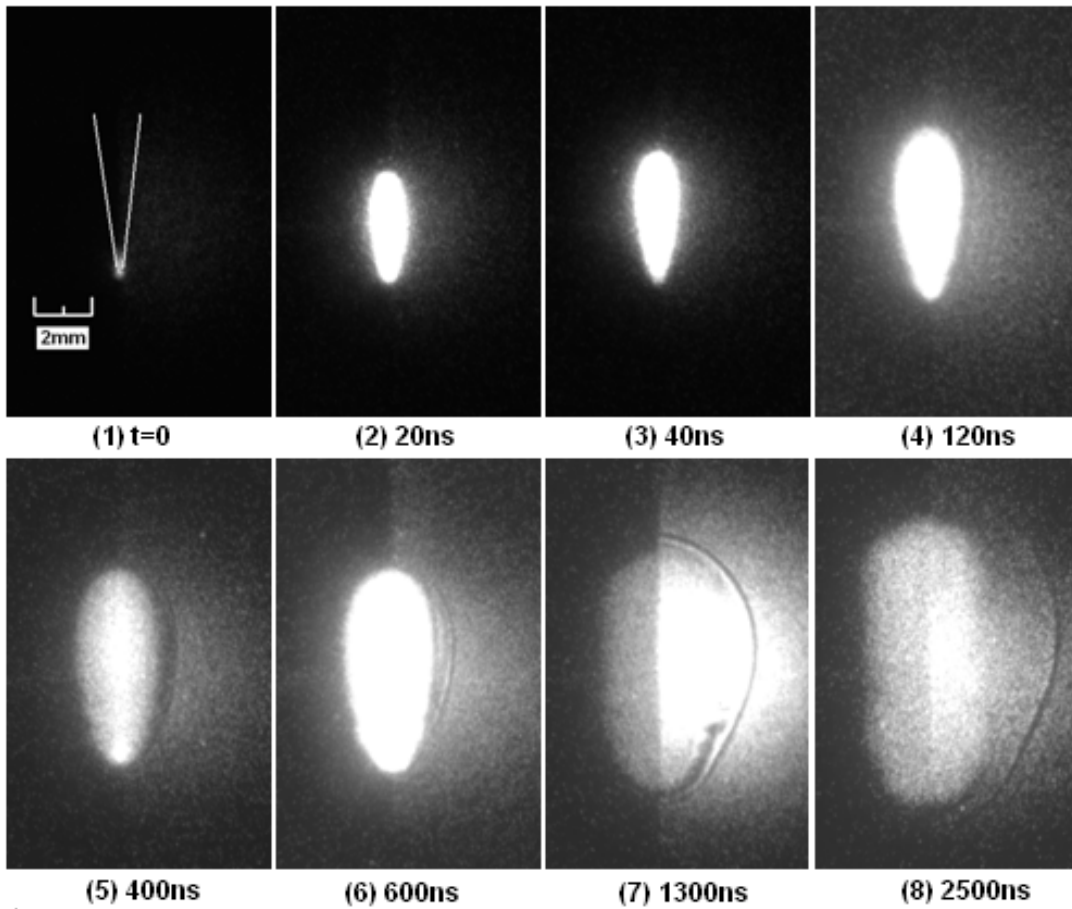


Figure 2.12: Shadowgraphs of  $E_i = 2.0$  J,  $f = 6.27$  at different time after breakdown in atmosphere air.

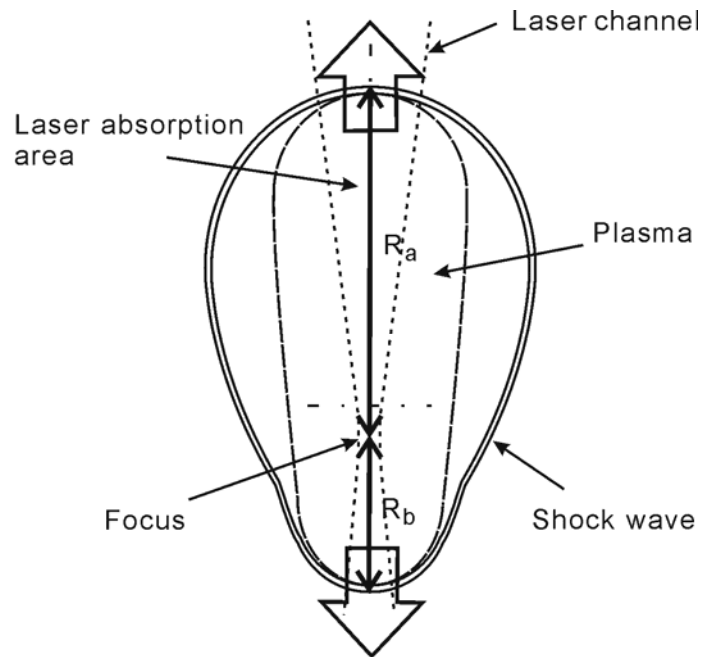


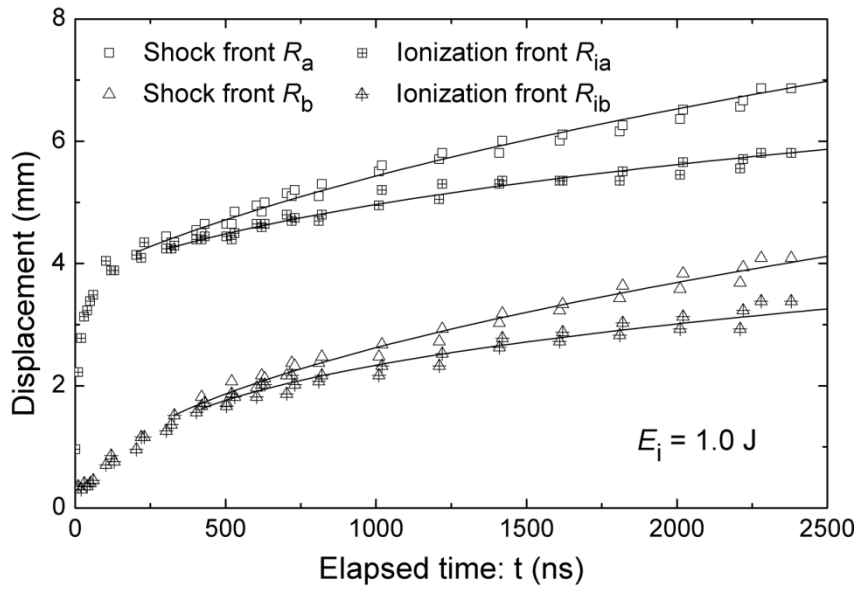
Figure 2.13: Schematic diagram of two directions propagation LSD wave

### *Two directional LSD and displacements of a shock wave and ionization front*

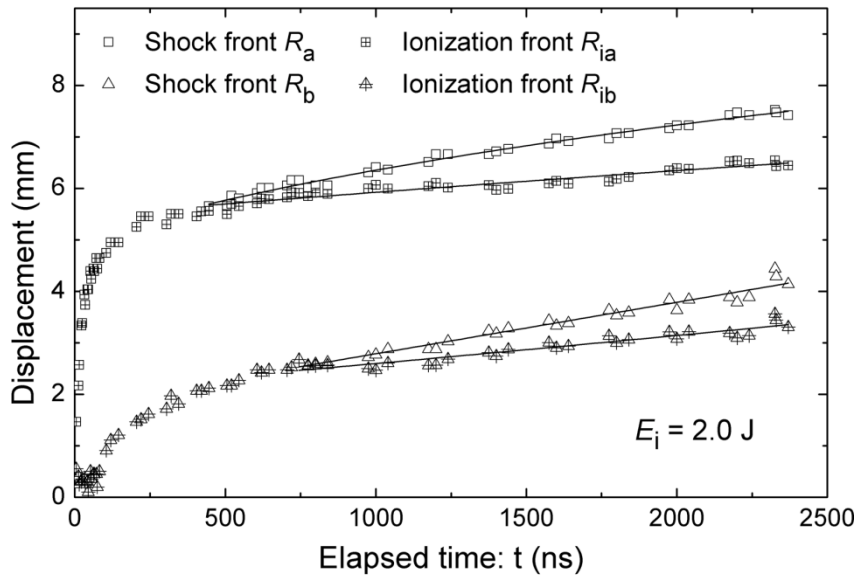
As the shadowgraphs (Fig. 2.12) show, the LSD wave was found to be driven in the forward (upstream) and the backward (downstream) directions in the laser channel. To characterize the evolution of this laser-induced blast wave precisely, a two directions LSD expansion model is proposed as illustrated in Fig. 2.13. The breakdown point, near the focus point, is set as the origin for all directions of expansion. As found in the test, the breakdown position was stable from pulse to pulse for the given laser energy and focusing condition. The respective subscripts a and b represent the displacements of the forward and backward propagation on the laser axis.

The displacements of the shock front  $R$  and the ionization front  $R_i$  from the obtained high speed images (Figure 2.12) are depicted in Fig. 2.14. As it shows, the backward (upstream) separation between a shock front and an ionization front occurred at approximately  $t=300$  ns for  $E_i=1.0$  J and 450 ns for 2.0 J. The forward (downstream) separation happened at around  $t=430$  ns for  $E_i=1.0$  J and 750 ns for 2.0 J. These separations respectively correspond to the terminations of the LSD regimes. Tendency appears that higher pulse energy caused longer LSD duration.

As calculated based on the laser profile and the shock expansion history, the laser intensities on the shock front at the LSD termination time were in the level of  $10^7$  W/cm<sup>2</sup>, which are still high enough to support plasma.



(a)



(b)

Figure 2.14: Temporal displacements of the shock wave front  $R$  and the ionization front  $R_i$ . Subscript a, forward expansion; b, backward expansion.  $E_i=1.0$  J (a) and 2.0 J (b).

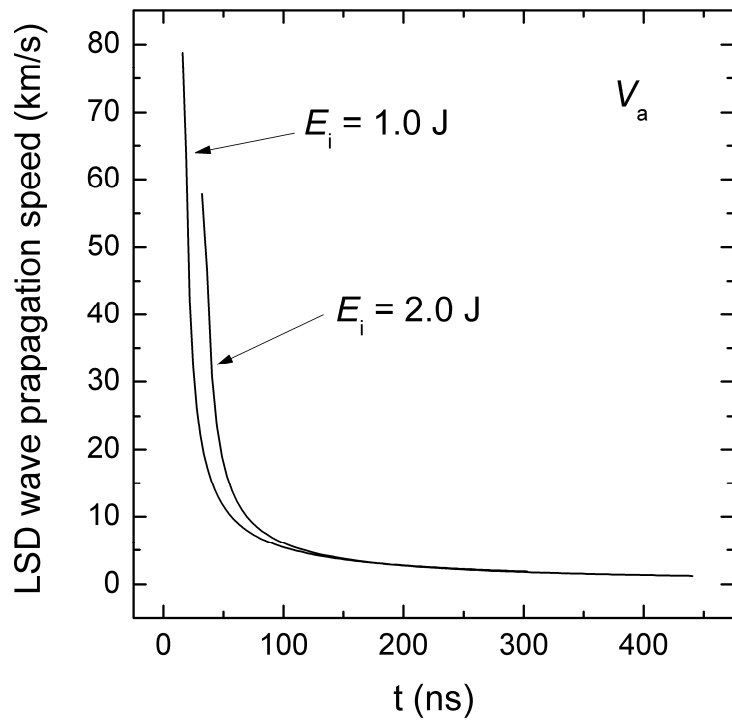
### *Propagation speed of a LSD wave*

The propagation speed of LSD wave under various experimental conditions has been studied. Raizer<sup>[1]</sup> has proposed a cube-root law to predict the relation between the upstream propagation speed of the LSD wave  $V_{\text{LSD}}$  and the laser power density on the shock wave front based on investigations with CO<sub>2</sub> laser:

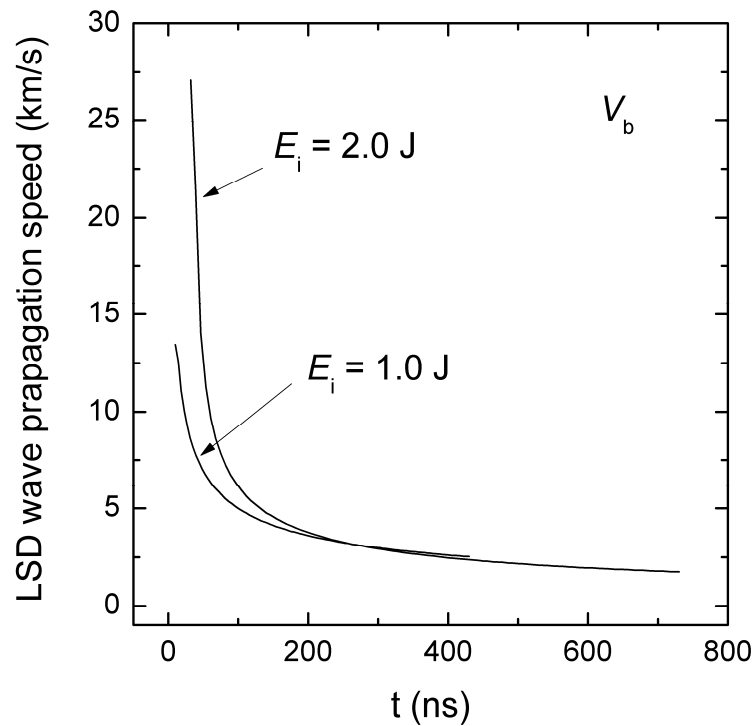
$$V_{\text{LSD}} = \left\{ 2 \left( \gamma_{\text{eff}}^2 - 1 \right) S / \rho_a \right\}^{1/3} \quad (2-3)$$

where  $\gamma_{\text{eff}}$  is the effective specific heat ratio,  $S$  is the laser power density irradiated on the LSD wave, and  $\rho_a$  is the ambient gas density.

The obtained temporal displacements of LSD waves could be functional fitted. A power function  $R = A(t - B)^C$  is used for these fittings. Then, by differentiating the fitting curves, the propagation velocities in two directions were obtained for  $E_i = 1.0$  and  $2.0$  J. The result is shown as Figure 2.15. There are dramatic speed declinations in the initial stages, about 100 ns, after the breakdown occur. This is attributed to the rapid decrease of laser power density on the LSD wave front, which was predicted by the cube-root law.



(a)



(b)

Figure 2.15: Propagation speeds of LSD waves in directions of (a) upstream (backward),  $V_a$ , and (b) downstream (forward),  $V_b$  for  $E_i = 1.0$  J and  $2.0$  J, 1 atm atmosphere air.

### 2.3 LSD wave termination conditions

For studying the LSD regime termination condition, the laser power density as a function of time on a LSD wave front was estimated. We assumed that the laser power is even in its cross section area. This is reasonable since the laser has a high-order transverse mode as measured in former section. Therefore, when the laser pulse is in its tail, about  $t > 50$  ns, the power density on the LSD wave could be obtained from

$$S = \frac{P_{0,tail} [A_1 \exp(-\frac{t}{\tau_{d1}}) + A_2 \exp(-\frac{t}{\tau_{d2}})]}{\pi r_{LSD}^2} \quad (2-4)$$

where the values of  $P_{0,tail}$ , factor  $A_1$ ,  $A_2$ , decay constant  $\tau_{d1}$  and  $\tau_{d2}$  has been listed in the laser pulse shape part. In the equation,  $r_{LSD}$  represents the radius on the blast wave front that irradiated by the laser beam, as shown in Figure 2.16. In addition, from the definition of focusing number  $f$ , the radius could be calculated from

$$r_{LSD} = \frac{D_{LSD}}{2f} \quad (2-5)$$

where  $D_{LSD}$  is the distance between the focus point and the shock front. For the upstream LSD propagation,  $D_{LSD} = R_a(t)$ . The temporal change of  $R_a$  was approximated with power function fitting. Because it is the incident laser characteristic that dominates the whole process. We focused on the power intensity on the upstream traveling LSD wave. Figure 2.17 shows the calculated  $S$  as a function of time. It can be seen that for both pulse energy cases, the backward LSD terminated at similar power density  $S$ , about  $110 \text{ MW/cm}^2$ . The results are listed in Table 2.4 together corresponding results gotten on  $\text{CO}_2$  laser. The LSD termination threshold are  $116 \pm 3 \text{ MW/cm}^2$  for  $E_i = 1.0 \text{ J}$ , and  $112 \pm 5 \text{ MW/cm}^2$  for  $E_i = 1.0 \text{ J}$ . This value is two orders of magnitude higher than that obtained in the  $\text{CO}_2$  laser case.

Table 2.4: Laser intensity threshold for backward LSD termination, together with CO<sub>2</sub> laser result<sup>[5]</sup>.

Laser	Pulse energy $E_i$ (J)	$f$	Backward LSD termination time	Threshold (MW/cm <sup>2</sup> )
Nd:glass	1.0	6.27	300 ns	$116 \pm 3$
	2.0	6.27	450 ns	$112 \pm 5$
TEA:CO <sub>2</sub>	4	2.2	2.1 $\mu$ s	$7.4 \pm 0.1$
	10	2.2	2.5 $\mu$ s	$3.7 \pm 0.4$

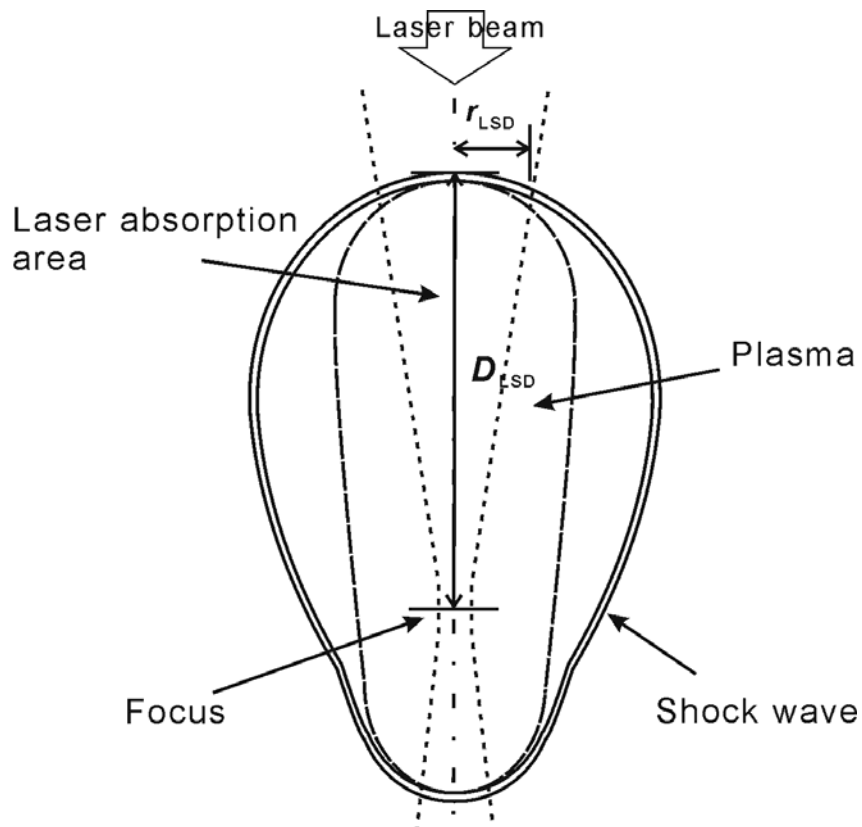


Figure 2.16: Schematic of the glass-laser induced LSD wave.

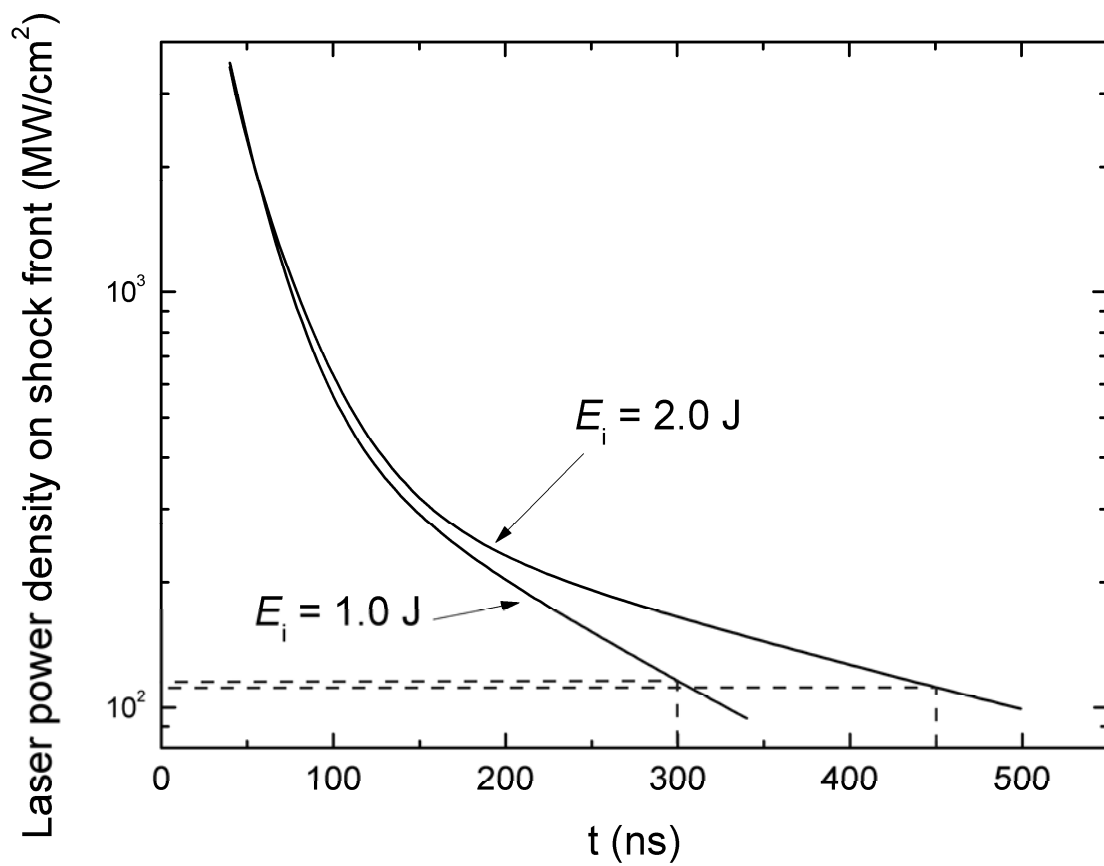


Figure 2.17: Laser intensities on the backward propagation shock waves,  $E_i = 1.0$  J and 2.0 J,  $f = 6.27$ .

## 2.4 Summary of Chapter 2

In order to clearly observe the separation between shock wave front and ionization front, a half self-emission half shadow graph experiment was designed to study the solid-state laser induced laser absorption wave. It is found that for solid-state laser with near-infrared wavelength, LSD wave propagates in two directions, both backward and forward along the laser beam axis. This indicates an incomplete laser absorption, which is mainly attributed to its low IB absorption coefficient for this wavelength.

The LSD termination threshold on the backward propagating shock wave is calculated at about  $100 \text{ MW/cm}^2$ , which are two orders of magnitude higher than that in the  $\text{CO}_2$  laser case. The result shows that this threshold is not sensitive to the pulse energy.

## References

- 1) Raizer, Yu. P., *Laser-Induced Discharge Phenomena*, Studies in Soviet Science, Consultants Bureau, New York, 1977
- 2) Bournot, P., Pincosy, P. A., Inglesakis, G., Autric, M., Dufresne, D., and Caressa, J.-P., "Propagation of a laser-supported detonation wave," *Acta Astronautica*, Vol.6, 1979, pp. 257-267
- 3) Maher, W. E., Hall, R. B., and Johnson, R. R., "Experimental study of ignition and propagation of laser-supported detonation waves," *Journal of Applied Physics*, Vol.45, 1974, pp. 2138-2145
- 4) Mori, K., Komurasaki, K., Arakawa, Y., *Applied Physics Letters*, 88 (2006), 12102
- 5) Mori, K., Komurasaki, K., Arakawa, Y., *Journal of Applied Physics*, Vol. 92, No. 10 (2002), pp. 5663E667
- 6) Wang, B., Yamaguchi, T., Hatai, K., Komurasaki, K., Arakawa, Y., *AIP Conference Proceedings* 1230, Arizona, USA, 2010, pp. 137-147

## Chapter 3

# BLAST WAVE ENERGY CONVERSION PROCESS

The blast wave energy conversion during the LSD process is schematically shown in Figure 3.1. The major difference between using a Nd:glass laser and a CO<sub>2</sub> laser is that, due to the low Inverse-Bremsstrahlung (IB) absorption coefficient in glass laser case, certain part of laser energy transmitted even after the breakdown, while the transmission after breakdown is negligibly small in the CO<sub>2</sub> laser case. Relation between incident pulse energy and absorbed energy should be firstly clarified under the given experimental condition. In addition, study on the temporal laser absorption is helpful to learn how much energy is absorbed during the LSD regime. It is known that not all the energy absorbed in the LSD regime could be converted to the blast wave energy. There is certain part of it is dissipated in the forms of radiant energy or

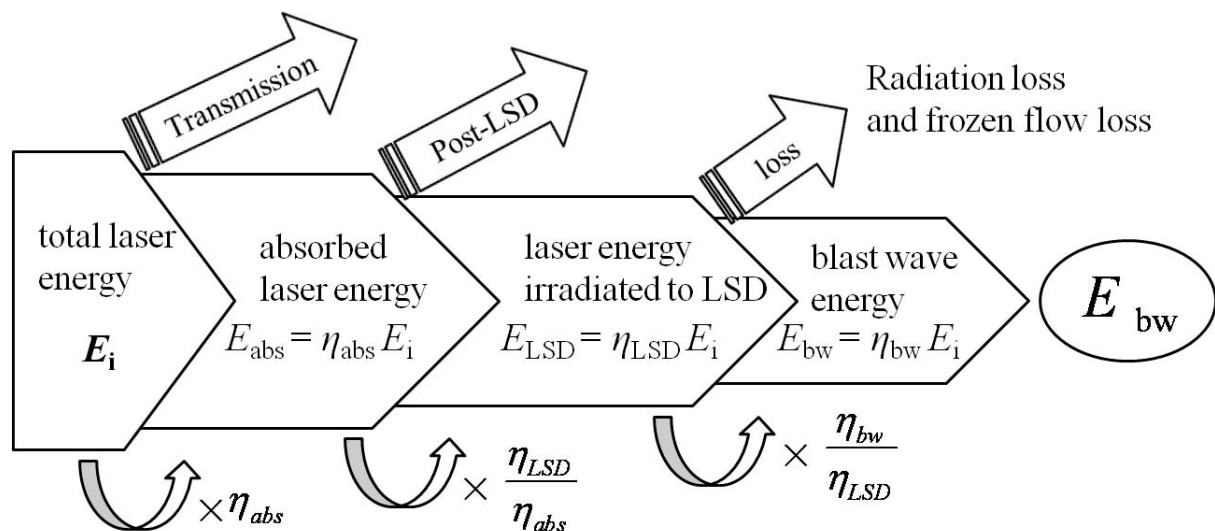


Figure 3.1: Energy conversion process for laser propulsion with a solid-state laser.

chemical potential energy frozen in plasma, which is an energy loss for laser propulsion application.

Blast wave energy efficiency  $\eta_{bw}$  is a decisive parameter for evaluating the feasibility of laser propulsion with solid-state laser. A method to extract  $\eta_{bw}$  from the glass laser induced blast wave expansion is firstly proposed. Besides, the  $\eta_{bw}$  dependency on factors like laser pulse energy, focusing number and ambient pressure are important for thrust performance optimization.

### 3.1 Fractional and temporal laser absorption

#### *Fractional laser absorption vs. $E_i$*

The fractional energy absorption  $\eta_{abs}$  at different incident pulse energy was studied with using of two energy meters (QE25LP-S-MB; Gentec Electro-Optics, Inc.). As illustrated in Figure 3.2, the laser beam output from Nd: glass laser is firstly splitted by a beam splitter. Major part of the beam, 96.1%, is reflected to generate breakdown in air, while the minor part is transmitted and received by an energy meter. After reflection, the parallel travelling beam is focused by a focus lens with focal length of 62.7 mm, result in a focusing number  $f = 6.27$ , which is the same as that used in former chapter. The transmitted energy is measured by another energy meter that is placed after the breakdown position. The influence of plasma radiation on energy meter is taken away by arrangement of putting the meter aside where it can only receive the radiation of plasma.

The result is shown in Figure 3.3. When pulse energy is lower than 0.7 J, there is no breakdown occurs in air, means that the laser power hasn't reached breakdown threshold at the focal spot. At  $E_i > 1.0$  J, though the absorbed energy increased with pulse energy, fractional absorption continuously decreased from 76% to 55%, from  $E_i = 1.0$  J to 2.0 J.

### *Optimum pulse energy vs. required energy*

This result indicates an absorption saturation trend with increase of pulse energy in a certain volume of air for a given optical condition. The highest absorption ratio is obtained when the irradiated laser energy just exceeds the breakdown threshold in this pulse energy level.

In a practical laser propulsion operation, the input laser power is assumed to be higher than 1 MW (pulse energy at 1 kJ level with repetition frequency of 1 kHz). To resolve this problem between optimum pulse energy and required energy in laser launch, finding a way to increase the effective laser absorption air volume will be necessary for big amount of energy absorption at an acceptable efficiency. In this way, thruster with specific beam reflecting surfaces should be designed. For example, design a multi-point ignition thruster, which uses separated mirrors instead of the continuous ring focus beam reflector proposed in Myrabo's lightcraft.

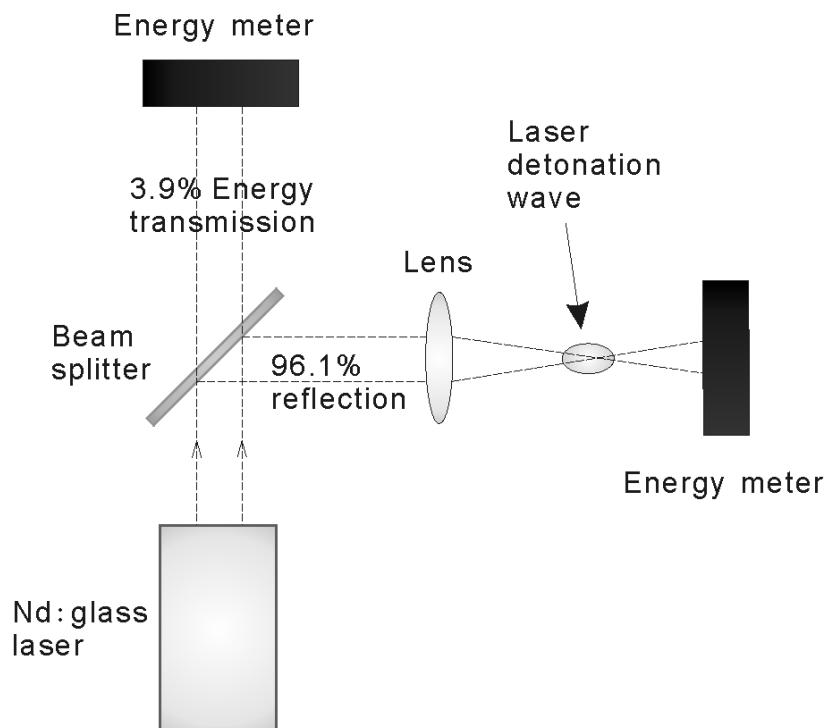


Figure 3.2: Setup of fractional energy absorption experiment.

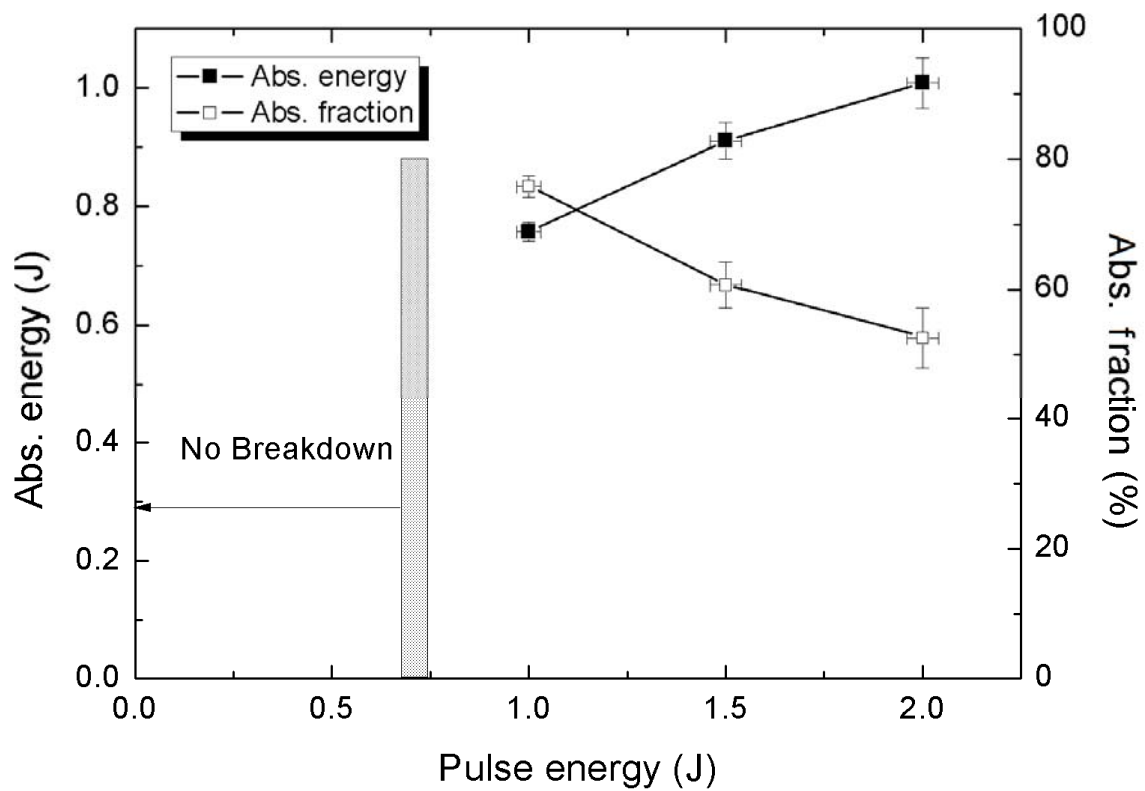


Figure 3.3: Energy absorption variation with laser pulse energy,  $E_i = 1.0, 1.5,$  and  $2.0$  J.

### Temporal laser absorption

With the help of placing two photodetectors (ET2030, Electro-Optics Technology, Inc) facing to the incident and transmitted laser beam, their temporal profiles were gotten synchronously. Then, the temporal laser absorption was obtained by subtracting the transmitting laser power from that of the incident during the process. Following that, cumulative absorbed energy is calculated by integrating this temporal power absorption.

The results with  $E_i=1.0$  J and 2.0 J are portrayed in Figure 3.4. The breakdown time was defined as the time at which the transmitted laser power reached its maximum value; it was approximately 14 ns after the start of laser irradiation. The influence of  $E_i$  variation on the breakdown time was small. Although the pre-breakdown absorption was negligibly small compared with the total laser energy, the pre-breakdown transmission was not. As an integration of the power profile before breakdown, the fractional transmission was 10% for  $E_i= 1.0$  J and 9% for  $E_i= 2.0$  J. In CO<sub>2</sub> laser case, it is only about 1% as listed in Table 3.1. This is because of its relative short time needed for generating breakdown in air.

After the breakdown, power absorption increased rapidly to a peak value and then decreased in accordance with the incident laser power decaying. The laser transmission is always higher in  $E_i= 2.0$  J case than 1.0 J case during the process, which results in an increase of fractional transmission with the pulse energy as measured in the last section. The fractional transmission after the breakdown was about 14% for  $E_i= 1.0$  J and 38% for  $E_i= 2.0$  J. Table 3.1 shows that this differs greatly from the CO<sub>2</sub> laser experiments.<sup>[1]</sup> Aside from that, more than 80% of the total energy absorption was completed in the first 200 ns after breakdown in each case.

Table 3.1: Measured fractional transmission for Nd:Glass laser and CO<sub>2</sub> laser

Fractional transmission	Laser	Nd:Glass laser, $f=6.27$		TEA-CO <sub>2</sub> laser, $f=2.2^{1)}$
		$E_i=1.0$ J	$E_i=2.0$ J	$E_i=10$ J
Before breakdown, %		10	9	1
After breakdown, %		14	38	1

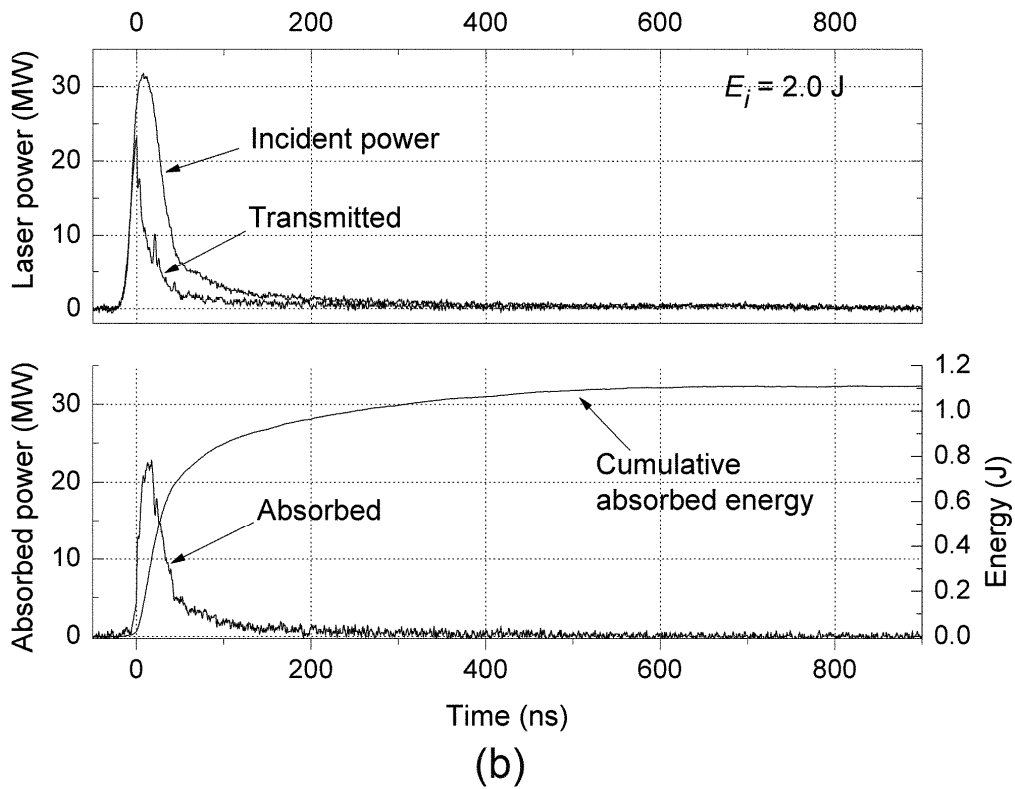
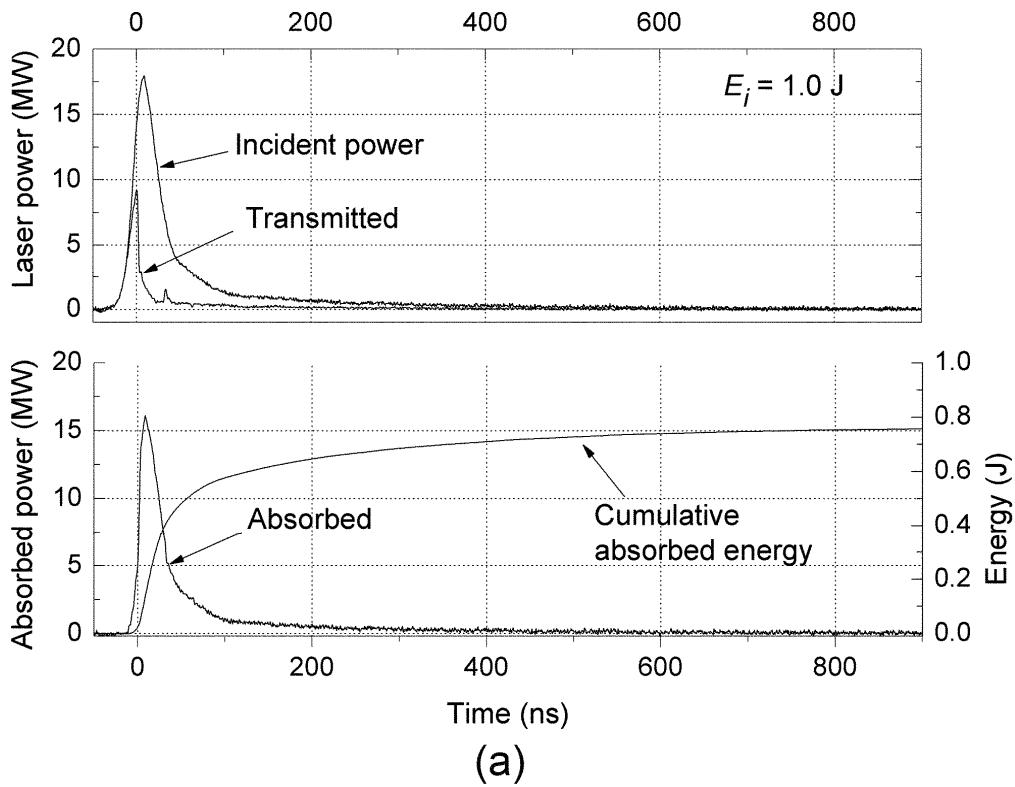


Figure 3.4: Temporal shapes of transmitted and absorbed laser power (a)  $E_i=1.0$  J/pulse and (b) 2.0 J/pulse.  $f=6.27$ .

In Chapter 2, the LSD termination time is observed in HSHS experiments. As found before, there are two directions LSD terminations in each case, backward and forward LSD propagation. Because the energy transfer from plasma to blast wave happens until the completely separation between them, the later separation time is the LSD termination time in the process. It is 430 ns for  $E_i = 1.0$  J, and 750 ns for  $E_i = 2.0$  J, with focusing number  $f = 6.27$ .

Different from the laser absorption wave induced by a CO<sub>2</sub> laser, a considerable part of the laser energy is transmitted through the waves, which is attributed to its low Inverse-Bremsstrahlung absorption coefficient. The IB absorption coefficient  $k_{IB}$  was calculated using Eq. (3-1),<sup>[2]</sup> where  $k_{e-i}$  and  $k_{e-n}$  indicate the energy transfer between electrons and ions and between electrons and neutron particles, respectively.

$$\begin{aligned}
 k_{IB} &= k_{e-i} + k_{e-n} \\
 &= \frac{4}{3} \left( \frac{2\pi}{3m_e k_B T_e} \right)^{\frac{1}{2}} \frac{z^2 e^6}{hc^4 m_e} G \left[ \exp(hc/\lambda k_B T_e) - 1 \right] \lambda^3 n_e n_i \\
 &\quad + \frac{k T_e^2 A(T_e)}{hc} \left[ 1 - \exp(-hc/\lambda k_B T_e) \right] \lambda^3 n_e n_n
 \end{aligned} \tag{3-1}$$

here  $G$  signifies a Gaunt factor,  $e$  is the electron charge,  $m_e$  represents the electron mass,  $h$  stands for Planck's constant,  $c$  denotes the speed of light,  $k_B$  is Boltzmann's constant,  $z$  denotes the ion charge number, and  $n_e$ ,  $n_i$  and  $n_n$  respectively represent the number densities of electron, ion, and neutron particles. Furthermore, factor  $A(T)$  has been tabulated for various gas species. The equation indicates that  $k_{IB}$  is proportional to the cube of the laser wavelength. Therefore, one order difference in  $\lambda$  between Nd:Glass laser ( $\lambda=1.053$   $\mu\text{m}$ ) and the CO<sub>2</sub> laser ( $\lambda=10.6$   $\mu\text{m}$ ) can engender several orders of difference in  $k_{IB}$ .

### 3.2 Shadowgraph experiment apparatus

Shadowgraph experiments were conducted to study the blast wave expansion history. The experimental setup is shown in Figure 3.5. Most of the apparatus used are the same as applied in the HSHS experiment. However, there are still some differences. One is that the plate placed for blocking half probing light is taken away because here we only need to learn the temporal evolution of a blast wave. Another is that for investigation of the  $\eta_{bw}$  dependency on focusing number, a laser quality focusing lens with 150 mm focal length was also used besides of the  $f = 62.7$  mm one. It works together with a beam expander which has magnification of 4, result in a focusing number  $f = 3.75$  as shown in Figure 3.6.

The experiments were performed in the same air condition as introduced in previous chapter. The temperature was kept in the range from 293 to 276 K by air conditioner. The humidity was controlled in the range between 50% and 60% during the tests, to ensure the experimental reproducibility.

In addition, for studying the ambient pressure influence on the propulsion performance, a chamber (see Figure 3.7) was applied for air pressure control. It has three windows in all. One is for passing of focused laser beam while the others are for the probing lights. A high power laser quality window for  $\lambda = 1.053$   $\mu\text{m}$  beam was assembled on it for avoiding the laser damage on window. The pressure in the chamber was changed by a rotary pump and monitored by a pressure meter (AP-C31, KEYENCE Corporation) during the experiment.

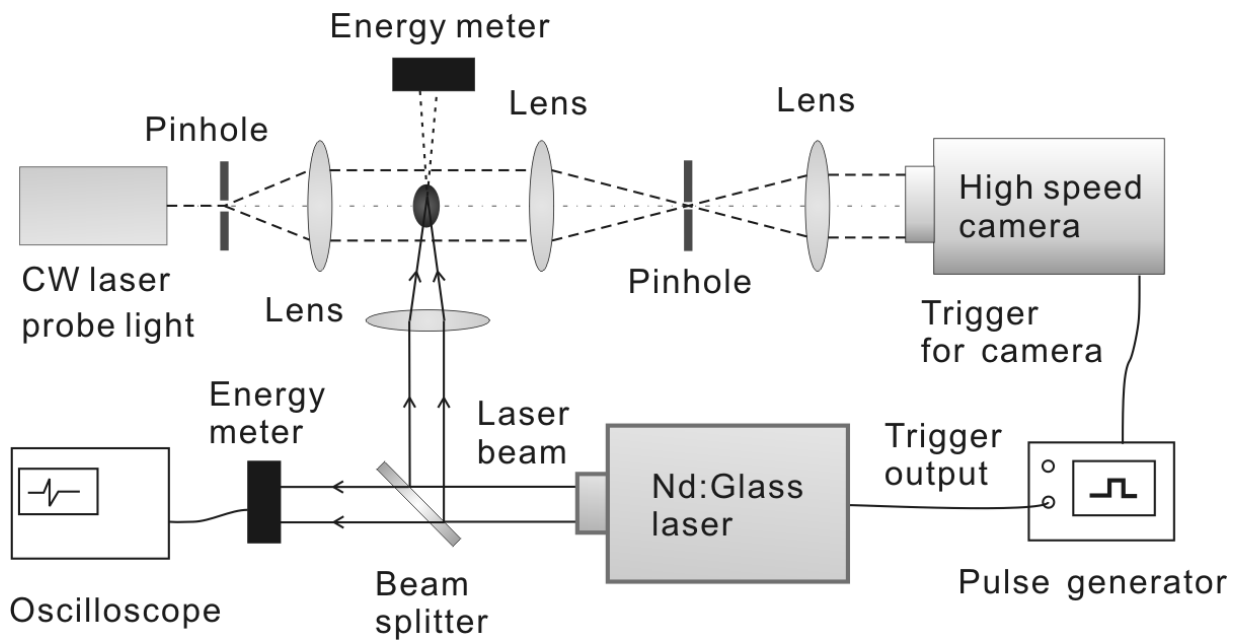


Figure 3.5: Setup of shadowgraph experiment.

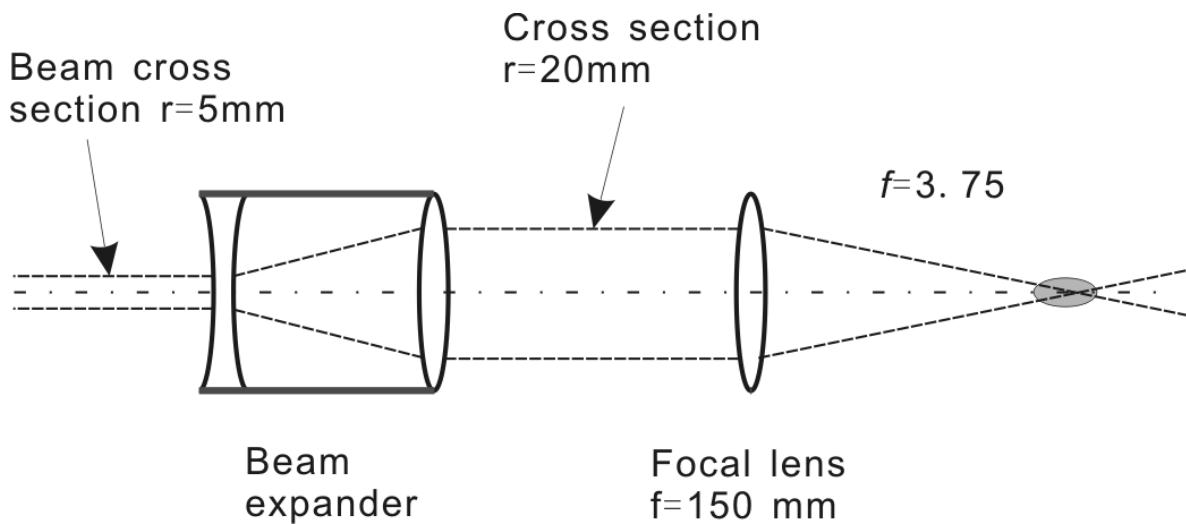
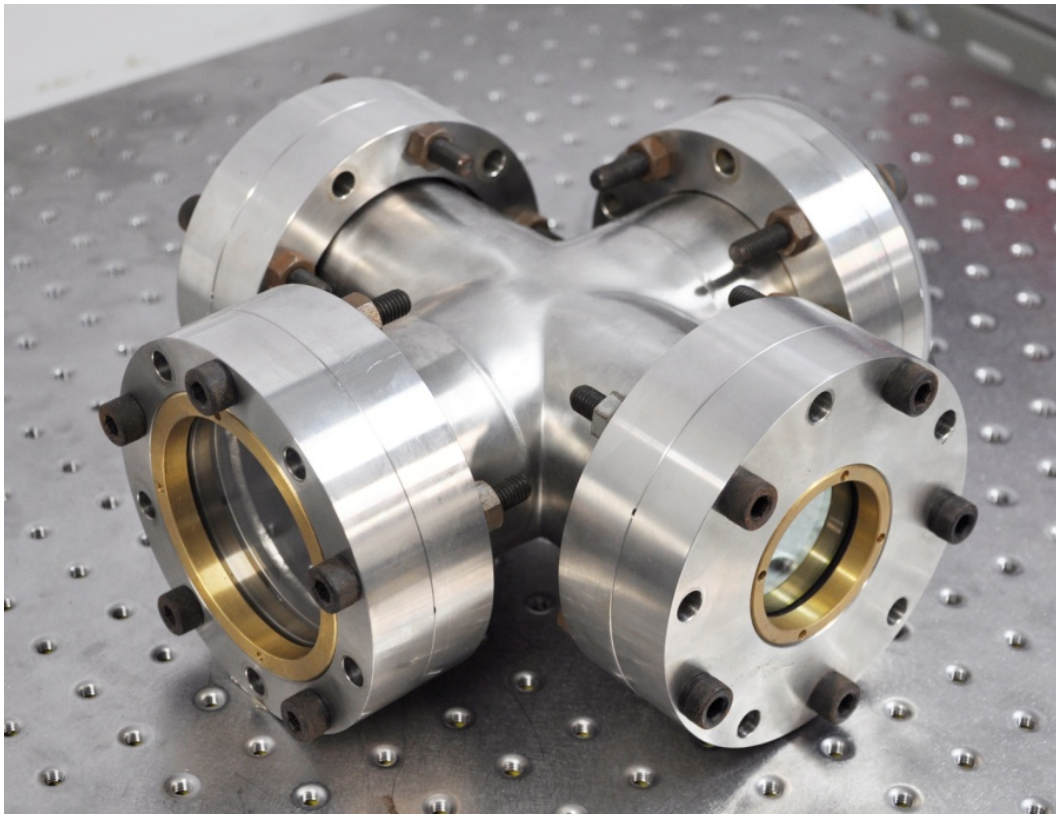
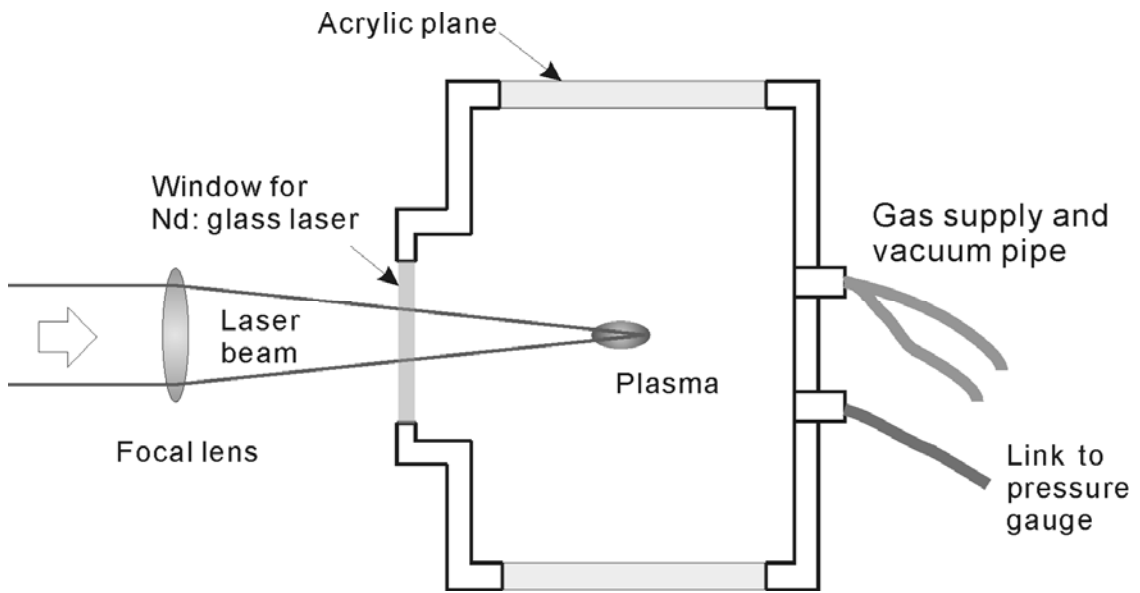


Figure 3.6: Optical setup for focusing  $f$  number 3.75.



(a)



(b)

Figure 3.7: Test cell for the experiments at reduced ambient pressures, (a) photo and (b) a schematic diagram.

### 3.3 Method to estimate the blast wave energy efficiency

#### 3.3.1 Temporal evolution of the laser absorption wave

A laser-induced blast wave is known to have two regimes that occur after breakdown. The first is designated as the LSD regime, in which an ionization front and a shock wave mutually contact and propagate at the same speed along the laser axis. The laser energy is transferred efficiently to the shock wave energy. The second is the adiabatic expansion regime. When laser power density decreases to a certain value after the peak of the laser power, the LSD regime terminates and the shock wave and the ionization front mutually separate. Plasma that remains behind a blast wave is heated in an isobaric condition by the successive part of the laser pulse and the shock wave expands adiabatically.

As the shadowgraphs (Figure 3.8(a)) show, the LSD wave was found to be driven in the forward (upstream) and the backward (downstream) directions in the laser channel. To characterize the evolution of this laser-induced blast wave precisely, a three-directional expansion model is proposed as illustrated in Figure 3.8(b). The breakdown point, near the focus point, is set as the origin for all directions of expansion. The respective values of  $R_a$  and  $R_b$  are the displacements of the forward and backward expansion on the laser axis;  $R_c$  is the largest shock wave displacement vertical to the laser axis.

In Figures 3.9 and 3.10, the measured shock displacements from shadowgraph images after LSD termination were fitted by power function curves<sup>[3]</sup> corresponding to the adiabatic blast wave expansion theory using the self-similar solution.<sup>[4,5]</sup> The expansion velocities in three directions were obtained by differentiating the fitted  $R_a$ ,  $R_b$ , and  $R_c$ . Although the blast wave is expected to achieve an identical expansion after a certain time as a result of enthalpy flow along the wave surface to form an spherical blast wave,<sup>[6]</sup> the uniform expansion speed was not achieved and the blast wave remained elliptic within 10  $\mu\text{s}$  after the breakdown.

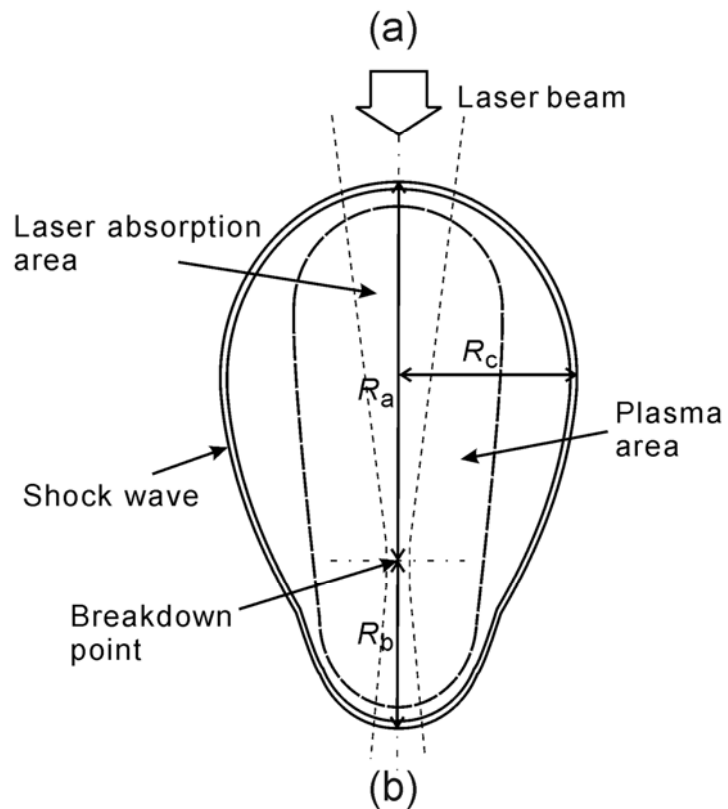
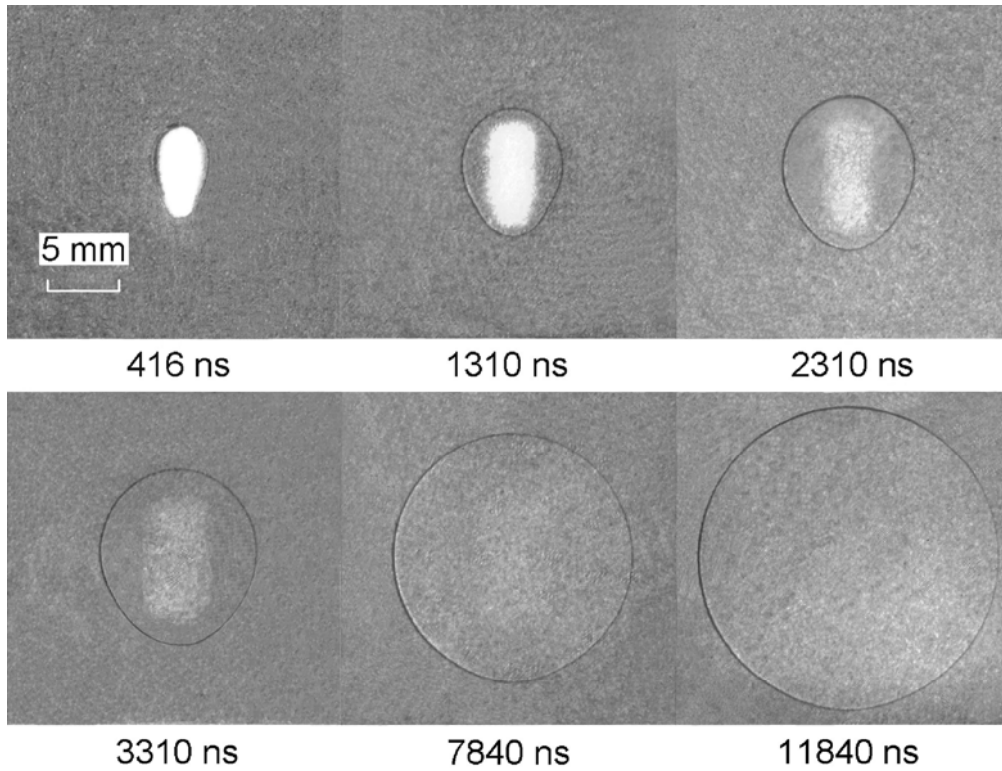
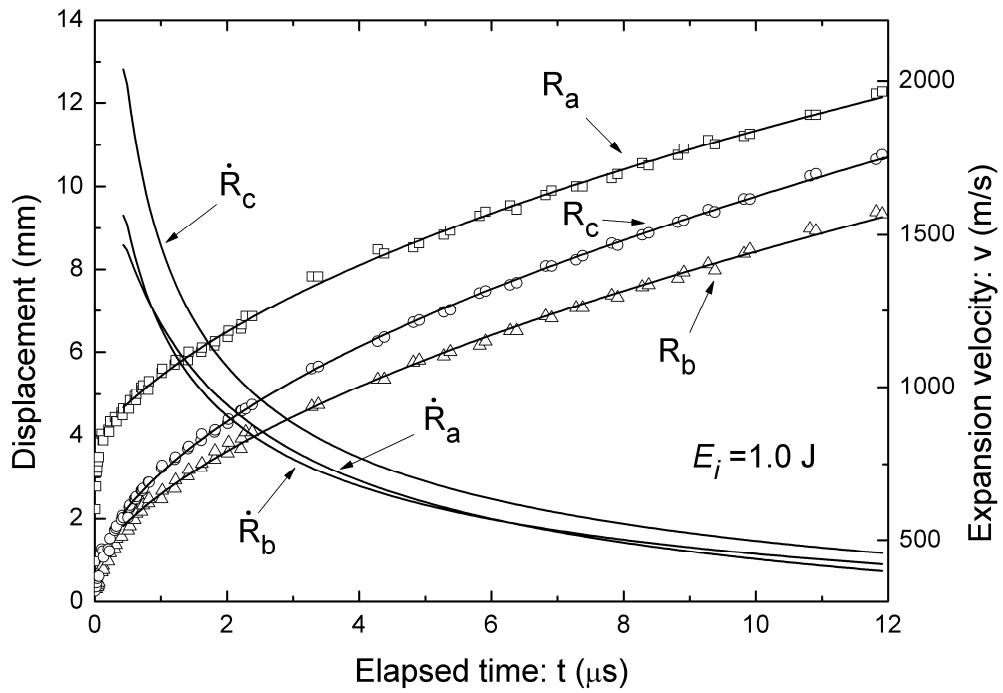
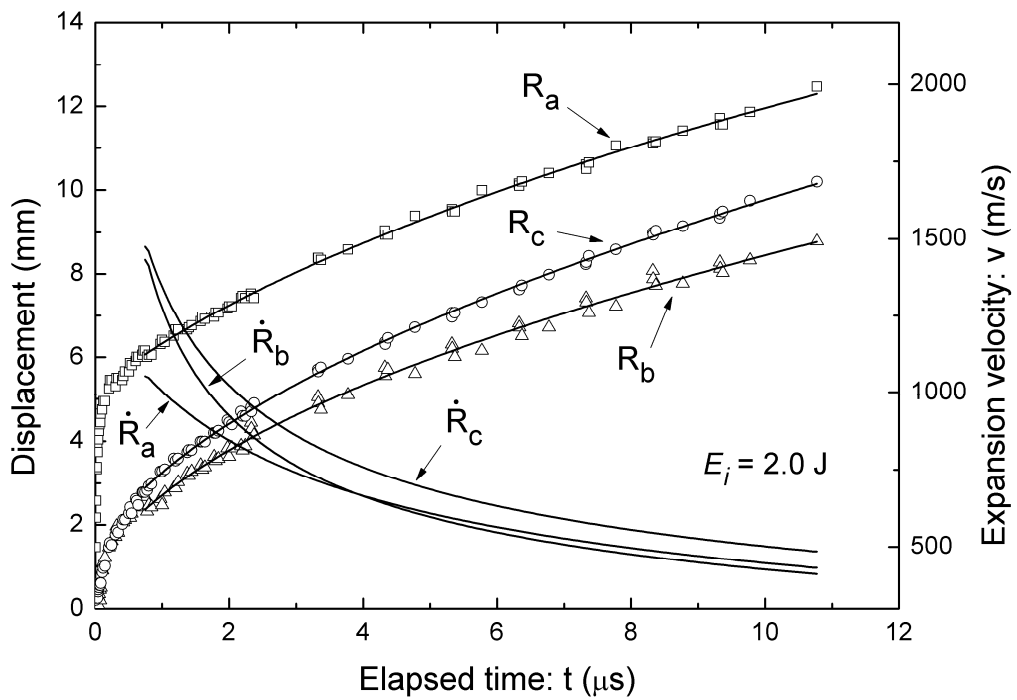


Figure 3.8: Images of evolution of the laser absorption wave,  $E_i = 1.0$  J (a), and schematic of laser generated blast wave expanding in three directions (b).

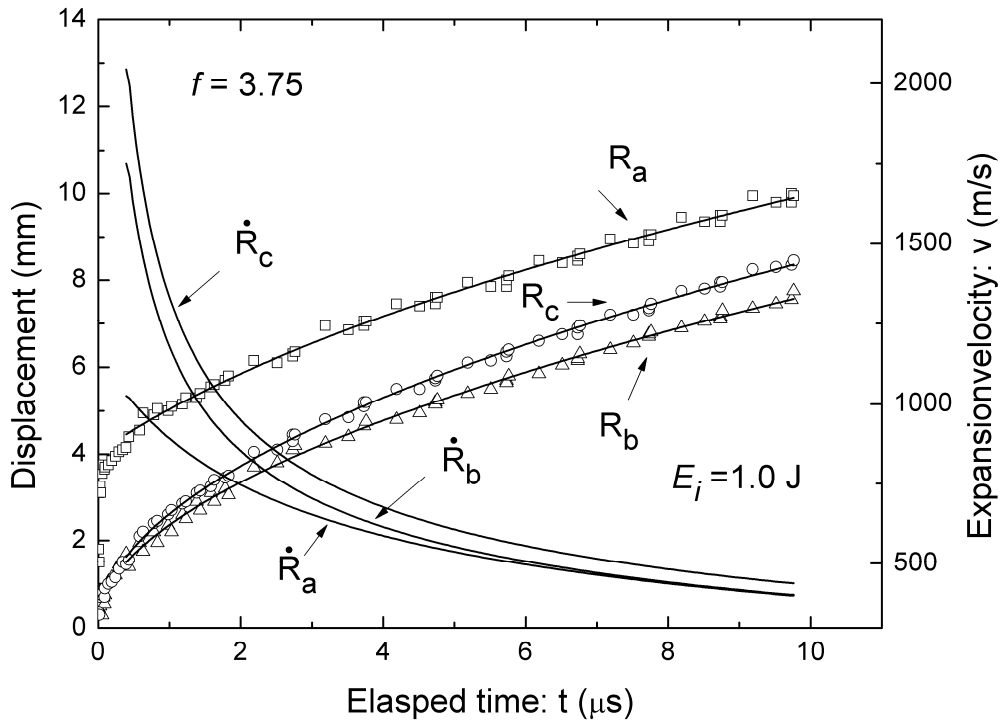


(a)

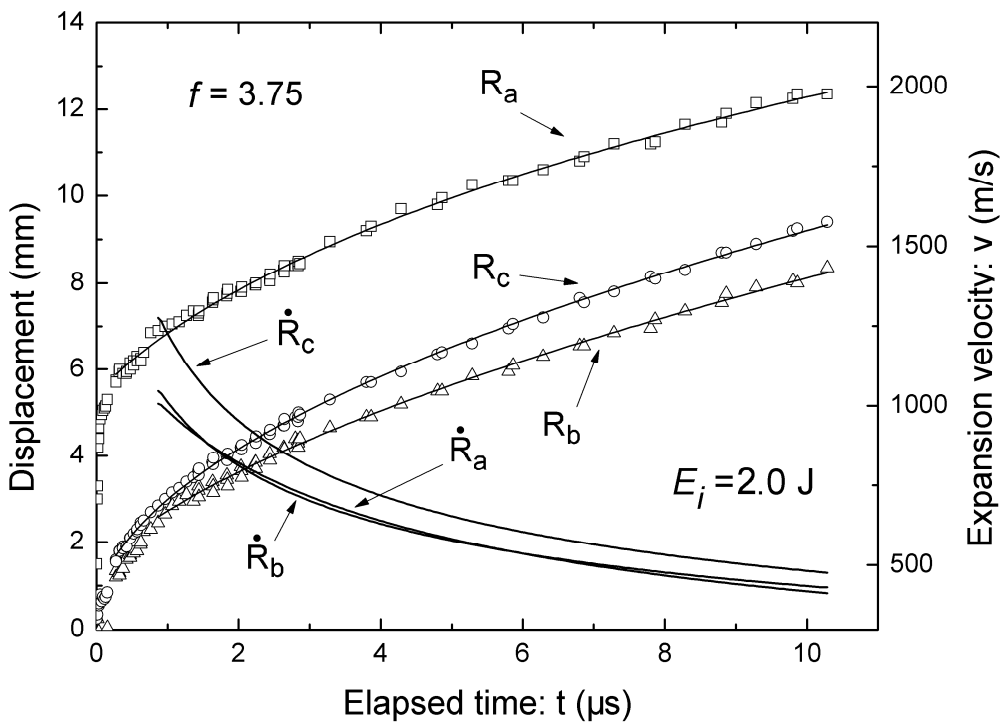


(b)

Figure 3.9: Temporal  $R$  variations and the expansion velocities for  $E_i=1.0 \text{ J}$  (a) and  $2.0 \text{ J}$  (b),  $f=6.27$ .



(a)



(b)

Figure 3.10: Temporal  $R$  variations and the expansion velocities for  $E_i=1.0 \text{ J}$  (a) and  $2.0 \text{ J}$  (b),  $f=3.75$ .

### 3.3.2 Blast wave energy

Some absorbed laser energy is converted to blast wave energy  $E_{\text{bw}}$ , as deduced by comparing the post-LSD blast wave expansion with the self-similar solution. Based on the blast wave theory,<sup>[5]</sup>  $E_{\text{bw}}$  for an adiabatically expanding elliptical blast wave is calculable from the equation as<sup>[7]</sup>

$$E_{\text{bw}} = \left( \frac{75\gamma}{16\pi\xi_0^5} \right) p_a V_{\text{bw}}(t) A M_s(t)^\alpha, \quad (3-2)$$

where ambient pressure  $p_a = 1.013 \times 10^5$  Pa,  $\xi_0$  is 1.03 for air when the specific heat  $\gamma = 1.4$ ;  $V_{\text{bw}}(t)$  signifies the time-dependent volume involved in the blast wave, and  $M_s$  denotes the expansion Mach number. The constant factors  $A$  and  $\alpha$  are 0.887 and 2.043, as derived respectively from the results of Brode's numerical computation, in response to  $2 < M_s < 48$ .

It is difficult to estimate the energy of a pear-shaped blast wave with different expansion velocities along different directions. Therefore, an elliptical expansion model with identical expansion velocity  $\bar{v} = dR(t)/dt$  introduced by Mori<sup>[1]</sup> was applied. In this approach, an elliptical expansion is characterized by a major radius  $R_{\text{major}} = (R_a + R_b)/2$  (along to the laser axis) and a minor radius  $R_{\text{minor}} = R_c$  (perpendicular to the axis) on the projected elliptic image. The uniform expansion Mach number  $M_s$  is given as shown below.

$$M_s(t) = \frac{\bar{v}}{c_a} = \frac{1}{c_a} \frac{d(R_{\text{minor}} + R_{\text{major}})}{2dt} \quad (3-3)$$

In that equation,  $c_a$  represents the speed of sound. Furthermore, the volume involved in the ellipsoid blast wave can be expressed as

$$V_{\text{bw}}(t) = \frac{4\pi}{3} R_{\text{major}} R_{\text{minor}}^2 \quad (3-4)$$

Using this model, the shock wave energy can be expressed as the following equation

$$c_a (E_{\text{bw}} / B p_a)^{1/\alpha} = R_{\text{major}}^{1/\alpha} R_{\text{minor}}^{2/\alpha} dR / dt \quad (3-5)$$

in which  $B$  is a constant under a given experimental condition, as shown below.

$$B \equiv A(75\gamma / 16\pi\xi_0^5)(4\pi / 3) \quad (3-6)$$

By integrating formula (3-5), an equation is deduced in which the blast wave energy  $E_{\text{bw}}$  can be computed from the blast wave temporal expansion radii.<sup>[7]</sup>

$$c_a \left( \frac{E_{\text{bw}}}{B p_a} \right)^{1/\alpha} = \frac{g(R_{\text{major}}(t), R_{\text{minor}}(t)) - g(R_{\text{major}}(t_0), R_{\text{minor}}(t_0))}{t - t_0} = \frac{\Delta g}{\Delta t} \quad (3-7)$$

$$g(R_{\text{major}}, R_{\text{minor}}) \equiv \int R_{\text{major}}^{1/\alpha} R_{\text{minor}}^{1/\alpha} dR \quad (3-8)$$

The slopes of  $g(R_{\text{major}}, R_{\text{minor}})$  after their LSD termination are depicted in Figure 3.11. The plots started from the LSD termination time and ended at the time when  $M_s$  decreased to 2 to ensure the validity of Equation 3.2. The inclination  $\Delta g / \Delta t$  represents the blast wave energy, which is constant in the adiabatic expansion regime. Using Equation 3.7, the corresponding energy was calculated as presented in Table 3.2. The error of this estimation might result from the difference between the assumption of elliptical blast wave and the realistic pear-shaped blast wave.

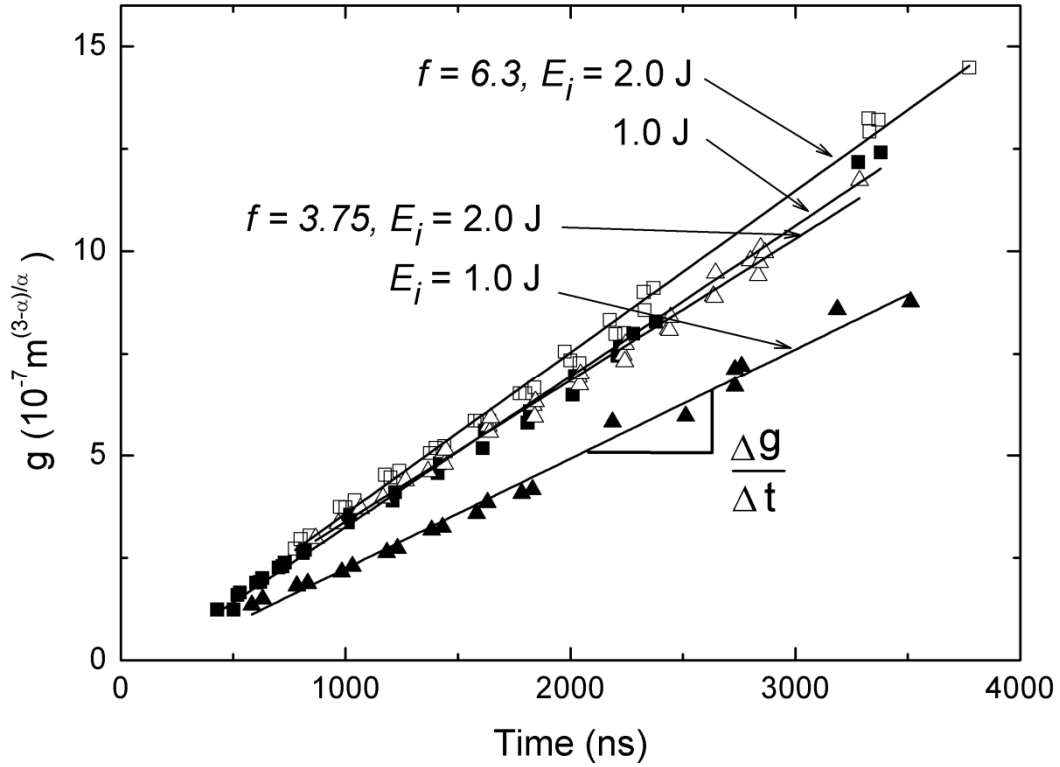


Figure 3.11: Temporal  $g$  variation with  $E_i = 1.0$  J and  $2.0$  J,  $f=6.27$ .

Table 3.2: Energy efficiencies with CO<sub>2</sub> laser data

	Nd:Glass laser				TEA-CO <sub>2</sub> laser <sup>[1]</sup>	
	$E_i = 1.0$ J		$E_i = 2.0$ J		$E_i = 10$ J	
$f$	3.75	6.27	3.75	6.27	2.2	3.3
$\eta_{bw} = E_{bw}/E_i$ , %	$31 \pm 2$	$59 \pm 2$	$40 \pm 4$	$34 \pm 1$	$47 \pm 5$	$44 \pm 10$
$E_{bw}/E_{abs}$ , %	90	78	81	62	48	45

### 3.3.3 Discussion

The blast wave energy efficiency  $\eta_{bw}$  was estimated as 59% for  $E_i=1.0$  J and 34% for 2.0 J, which are of the same level as that in CO<sub>2</sub> laser experiments<sup>[1]</sup> in spite of its large transmissions, because of its efficient energy conversion from  $E_{aba}$  to  $E_{bw}$ . The conversion efficiency  $E_{bw}/E_{abs}$  is almost twice as high as that obtained in CO<sub>2</sub> laser experiments probably because of its faster LSD propagation and higher plasma density than CO<sub>2</sub> laser-induced LSD. In future development, reduction in transmission will be important to achieve high  $\eta_{bw}$  because transmission is the predominant energy loss mechanism in the Nd:Glass laser case.

An increasing tendency of  $\eta_{bw}$  with  $f$  number was observed at  $E_i = 1.0$  J. This tendency is opposite to that for  $E_i = 2.0$  J and the CO<sub>2</sub> laser ones, which implies the existence of an optimum  $f$  number for energy conversion.

In conclusion, high-power glass laser oscillating at near-infrared wavelength is a promising candidate for laser energy conversion applications such as laser propulsion and igniters.

### 3.3.4 Energy flow

Here the energy flow, as schematically shown in Figure 3.1, in the blast wave energy converting process can be finally tabulated in Table 3.3. The major energy loss in the process is the laser transmission for this near infrared wavelength laser. The laser beam fractions absorbed during the LSD regime  $\eta_{\text{LSD}}$  is between 50 ~ 70% in glass laser for both pulse energy, which is lower than that gotten in CO<sub>2</sub> laser case. However, though this  $\eta_{\text{LSD}}$  is lower, the final blast wave energy efficiency  $\eta_{\text{bw}}$  is high, which is especially true in  $E_i = 1.0$  J case. The conversion ratio,  $\eta_{\text{bw}}/\eta_{\text{LSD}} = 86\%$ , is obviously higher than the CO<sub>2</sub> laser result. This high conversion ratio is the major reason that the blast wave energy efficiency could reach as high as that gotten use CO<sub>2</sub> laser.

It is known that the energy losses in the conversion from  $E_{\text{LSD}}$  to  $E_{\text{bw}}$  are in forms of radiation and frozen flow. So this result means that the radiation and frozen flow losses when using solid-state laser are smaller than that in the CO<sub>2</sub> laser case. This is reasonable because the CO<sub>2</sub> laser induced LSD wave has very thin laser absorption layer, which is typically less than 1 mm, propagating with the blast wave. The high energy deposition in this area results in the generation of a high temperature plasma area, and thus serious radiation energy loss and frozen flow loss. For solid-state laser, the relative lower IB absorption coefficient results in a thicker laser absorption layer, in another word, a larger absorption volume. So the concentration of high temperature plasma area is not so serious compares with that happens in the CO<sub>2</sub> laser case, which means lower radiation loss and frozen flow loss.

Table 3.3: Energy flow in the blast wave energy conversion process

	$E_i$ (J)	$\eta_{\text{abs}}$	$\eta_{\text{LSD}}$	$\eta_{\text{bw}}$	$\eta_{\text{bw}}/\eta_{\text{LSD}}$
<i>Glass laser</i>	1.0	76%	69%	59%	86%
	2.0	55%	54%	34%	63%
<i>CO2 Laser</i>	10	98%	86%	47%	55%

### 3.4 Ambient pressure influence

Experiments were conducted in a test cell to investigate the blast wave energy conversion process influenced by ambient pressure. The energy absorption in air pressure ranged from 100 kPa to 30 kPa is shown in Figure 3.12. At  $30 < p_a < 101$  kPa, the absorption fraction decreased continuously with the reducing on pressure. However, this decrease is not serious, only 16% as the pressure declined to 30 kPa. Then, at  $p_a < 30$  kPa breakdown become difficult under the optical condition.

With the same experimental arrangement as previous study, laser transmission profiles with  $E_i = 2.0$  J for ambient air pressure of 101, 80, 50, 30 kPa are portrayed in Fig. 3.13. As shown there, the breakdown time was approximately 14 ns after the start of laser irradiation. A trend is that, lower air pressure lead to shorter time needed for breakdown. In other words, a decrease in ambient pressure leads to a decrease in breakdown power threshold. However, this influence is small. The pre-breakdown transmissions were about 8% of the total energy for the tested pressures.

After the breakdown, if check closely about the transmission profiles in the figure, it could be seen that major differences between those transmission curves only appear in the time duration from the breakdown time to about 200 ns. It is the small power differences during this period that makes the difference on the cumulative transmission energy. A tendency is that lower ambient pressure leads to higher temporal power transmission all through the process in the pressure range studied.

The evolution of blast waves gotten in Shadowgraph experiments are shown in Figure 3.14, with applying the three directions expansion model. Follow the same calculation process as introduced in former sections, the corresponding  $g$  after their LSD termination in different ambient pressures were obtained as given in Figure 3.15. From the slopes of  $g$ , the blast wave energy efficiencies are figured out and listed in Table 3.4.

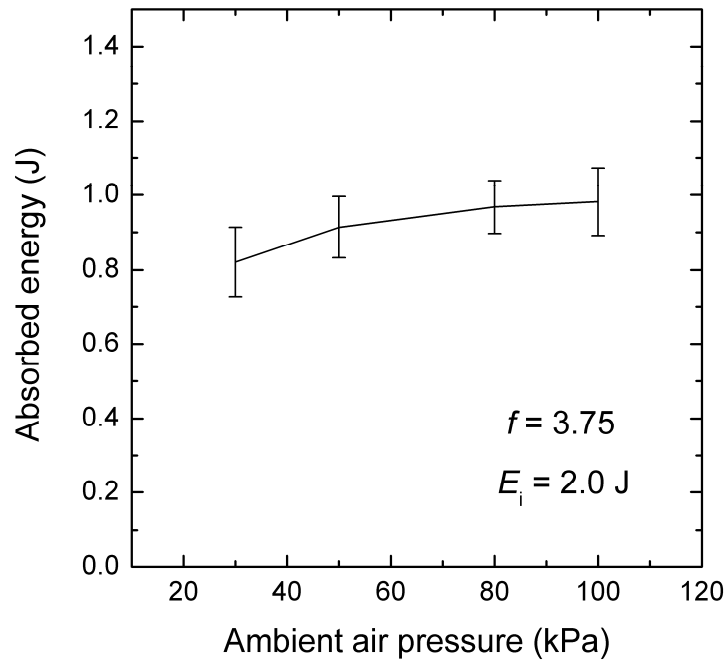


Figure 3.12: Energy absorbed under reduced air pressure,  $E_i = 2.0 \text{ J}$ ,  $f=3.75$ .

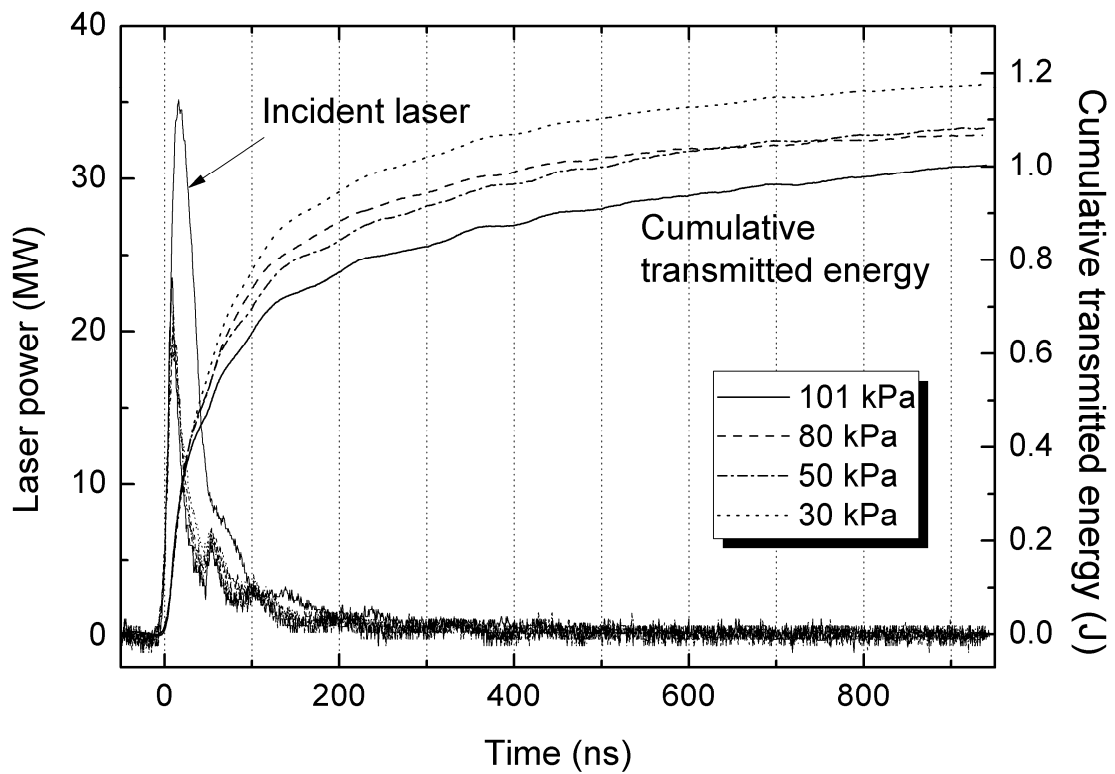
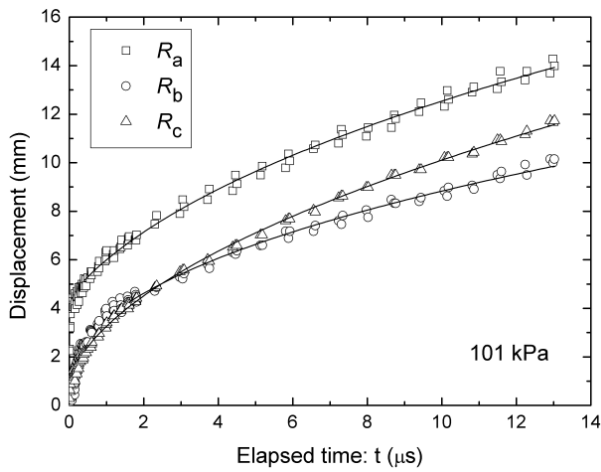
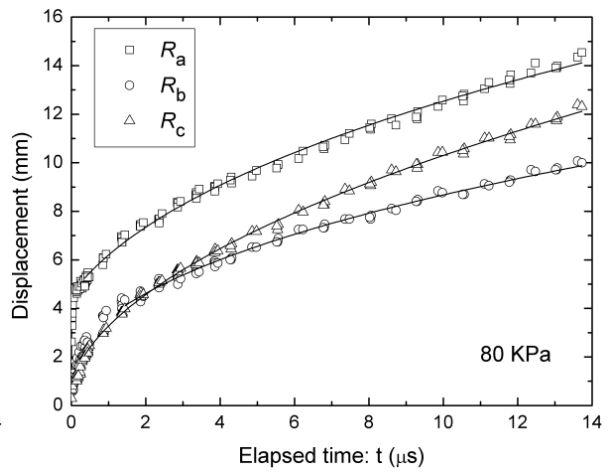


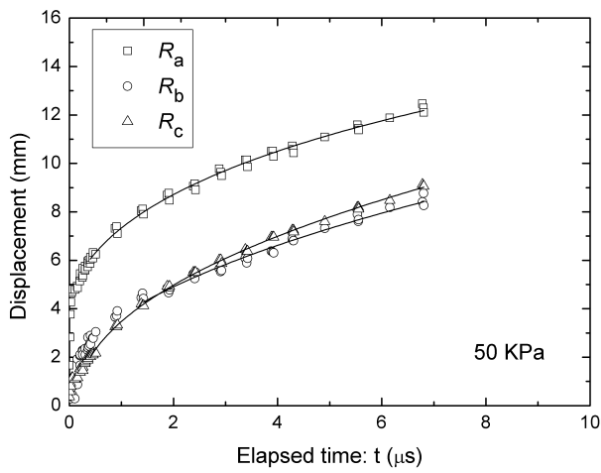
Figure 3.13: Temporal incident and transmitted laser power  $E_i=2.0 \text{ J/pulse}$ ; air pressures are 101, 80, 50 and 30 kPa.



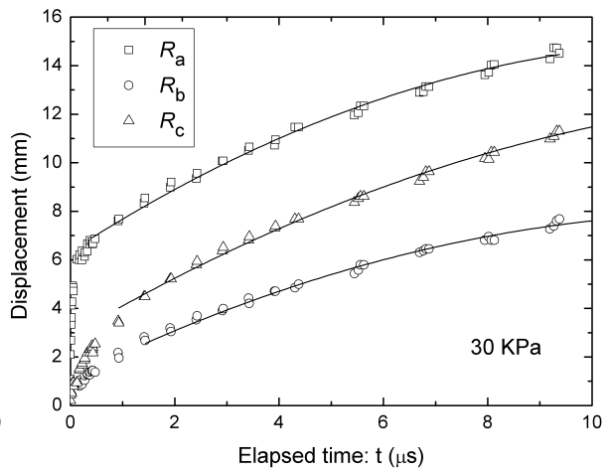
(a)



(b)



(c)



(d)

Figure 3. 14: Blast wave expansion in three directions, for (a) 101 kPa, (b) 80 kPa, (c) 50 kPa and (d) 30 kPa.

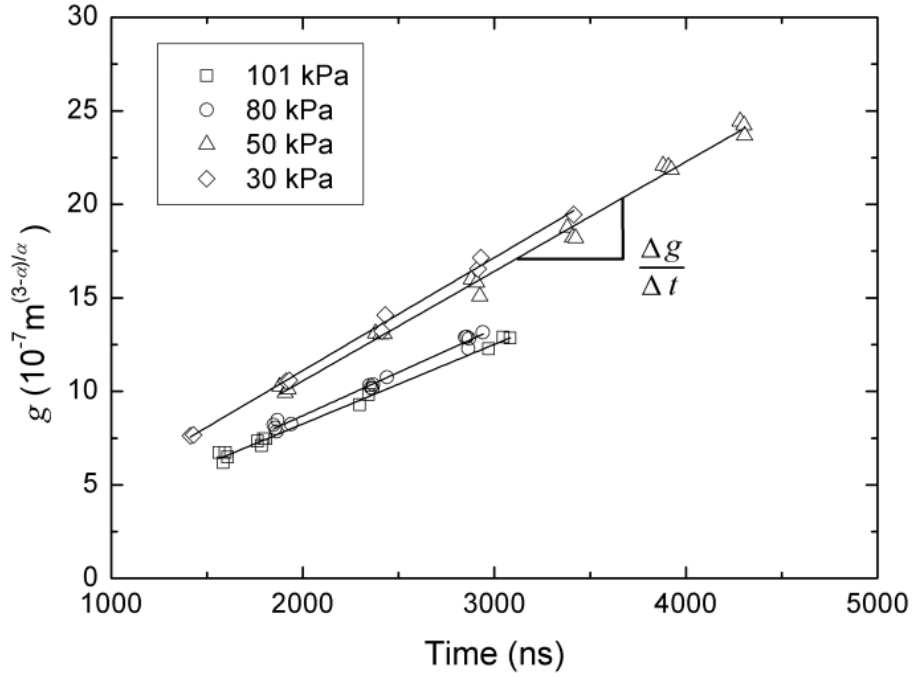


Figure 3.15: Temporal  $g$  variation at reduced ambient pressure.

Table 3.4: Energy flow in the blast wave energy conversion process under various ambient pressure,  $f=3.75$ .

	$p_a$ (kPa)	$E_i$ (J)	$E_{abs}$ (J)	$\eta_{abs}$	$E_{LSD}$ (J)	$\eta_{LSD}$	$E_{bw}$ (J)	$\eta_{bw}$
$f=3.75$	101	2.0	0.98	49%	0.94	47%	$0.80 \pm 0.08$	$40 \pm 4\%$
	80	2.0	0.97	49%	0.91	46%	$0.76 \pm 0.10$	$38 \pm 5\%$
	50	2.0	0.91	45%	0.86	43%	$0.76 \pm 0.06$	$38 \pm 3\%$
	30	2.0	0.82	41%	0.74	37%	$0.48 \pm 0.04$	$24 \pm 2\%$

The blast wave energy efficiency  $\eta_{bw}$  was estimated as 40% for  $E_i=2.0$  J in 1 atm, and it slightly decreased to 38% as the air pressure reduced to 50 kPa, which still approximates that gotten in the CO<sub>2</sub> laser case. This high  $\eta_{bw}$  is due to its efficient energy conversion from  $E_{ab}$  to  $E_{bw}$ . The result indicates that the decreasing of ambient pressure plays a negative role in the energy conversion process from absorbed laser energy to blast wave energy when the pressure is under a certain value.

In future development, optimization of the thrust performance like  $\eta_{bw}$  should be more focused on ways like changing optical and laser beam conditions, because transmission is the predominant energy loss mechanism in the Nd:Glass laser propulsion case.

### **3.5 Summary of Chapter 3**

Temporal laser absorption and transmission are obtained with photodetectors, which show that laser transmission is always occurring during the laser pulse, higher pulse energy lead to higher power transmission.

Blast wave energy efficiency with use of a solid-state laser was estimated. Result shows that  $\eta_{bw}$  could reach as high as 59%, which approximates that obtained in CO<sub>2</sub> laser. The efficiency is sensitive to both pulse energy and focusing  $f$  number. For ambient air pressure range 50 kPa to 101 kPa, the efficiency is not sensitive to the pressure. It decreases as the pressure further reduced to 30 kPa.

As a result, the blast wave energy conversion with a solid state laser process is clarified. The main energy loss comes from the laser transmission during the laser pulse.

## References

- 1) K. Mori, K. Komurasaki, and Y. Arakawa, *J. Appl. Phys.* **95**, 5979, 2004
- 2) N. H. Kemp, and P. F. Lewis, *Laser-heated thruster, interim report*. NASA-CR-161665, 1980, P. 9.
- 3) J. F. Kielkopf, *Physical Review E*. **52**(2), 2013–2024, 1995.
- 4) Ya. B. Zel'dovich and Yu. P. Raizer, *Physics of shock Waves and High-temperature Hydrodynamics Phenomena*. Dover, New York, 2002, p. 93.
- 5) L. I. Sedov, *Similarity and Dimensional Methods in Mechanics*. Academic Press, New York, 1959, p. 185.
- 6) G. B. Whitham, *Linear and Nonlinear Waves*. Wiley, New York, 1999, pp. 263–311
- 7) H. L. Brode, *J. Appl. Phys.* **26**, 766, 1955

## Chapter 4

# THRUST GENERATION PROCESS

The impulsive thrust generated by focusing pulsed Nd: Glass laser in cone-shaped nozzle thrusters was measured in an impact pendulum experiment, to validate the blast wave energy efficiency obtained in the former chapter. After that, the relationship between the thrust performance in terms of  $C_m$  and the nozzle scale was studied. The results were compared with that obtained in CO<sub>2</sub> laser experiments.

### 4.1 Experimental setup for thrust measurement

The impact pendulum experiment was conducted to study the thrust performance use the solid-state laser. The experimental setup is schematically shown in Fig. 4.1. By focusing the pulse laser in a thruster nozzle, plasma is generated at the focusing point. Its expansion drives a blast wave which brings impulse to the thruster as the blast wave reached the nozzle wall. Then the pendulum starts to swing around the pivot. By comparing the maximum displacement with a calibration result, the thrust is estimated.

Based on former  $\eta_{bw}$  result, the optical condition which gotten the highest blast wave energy efficiency,  $\eta_{bw} = 59\%$ , is applied in this experiment. The aspheric lens with 62.7 mm focal length, focusing number  $f = 6.27$ , is used to generate breakdown in the thruster nozzles. The pulse energy was  $E_i = 1.0$  J with a pulse to pulse error of 0.02 J. A laser displacement sensor (Keyence Inc., LK-500) was used to measure the thruster displacement.

In order to compare with the results gotten in the CO<sub>2</sub> laser case<sup>[1]</sup>, conical nozzle was

selected to learn the thrust performance and discuss the relation between the impulse and the nozzle scale. The conical nozzles (Fig. 4.2) are made of aluminum, with a half-cone angle of  $\alpha$  and nozzle length of  $r_n$ . For studying the influences of nozzle geometry on  $C_m$ , several nozzles with different  $\alpha$  and  $r_n$  were made.

The largest difference of this experiment from that has been performed with CO<sub>2</sub> laser is that the laser focusing point is not set at the conical apex. There are two reasons for this arrangement. One is that their laser absorption structures are different. In CO<sub>2</sub> laser case, the LSD only propagates upstream along the laser axis after breakdown. So an LSD starts from cone apex does not influence the energy absorption and conversion in the process. However, in the solid-laser case, the laser energy absorption happens in both forward and backward directions. In this reason, some space between the breakdown point and the cone apex is needed for the forward propagation LSD. The other reason is that if the micrometer wavelength laser beam is focused at the conical apex, serious laser ablation will happen. Therefore, certain distance between the focusing point and the apex is necessary for avoiding this ablation effect. During the experiment, the breakdown position was adjusted to get the highest  $C_m$  for each nozzle shape.

As schematically shown in Fig. 4.3, the relationships between the impulse and the thruster maximum displacement for each nozzle were calibrated with an impulse-hammer<sup>[2,3]</sup>. The temporal force signal was measured by a load cell (LMA500GA-P, Fig. 4.4(a)) mounted at the head of the hammer. Fig. 4.4(b) shows an example signal gotten with this load cell. The impulse imparted to the thruster could be obtained by integrating the temporal force signal. A calibration line is given in Fig. 4.5 which shows good linearity between the impulse and the maximum displacement.

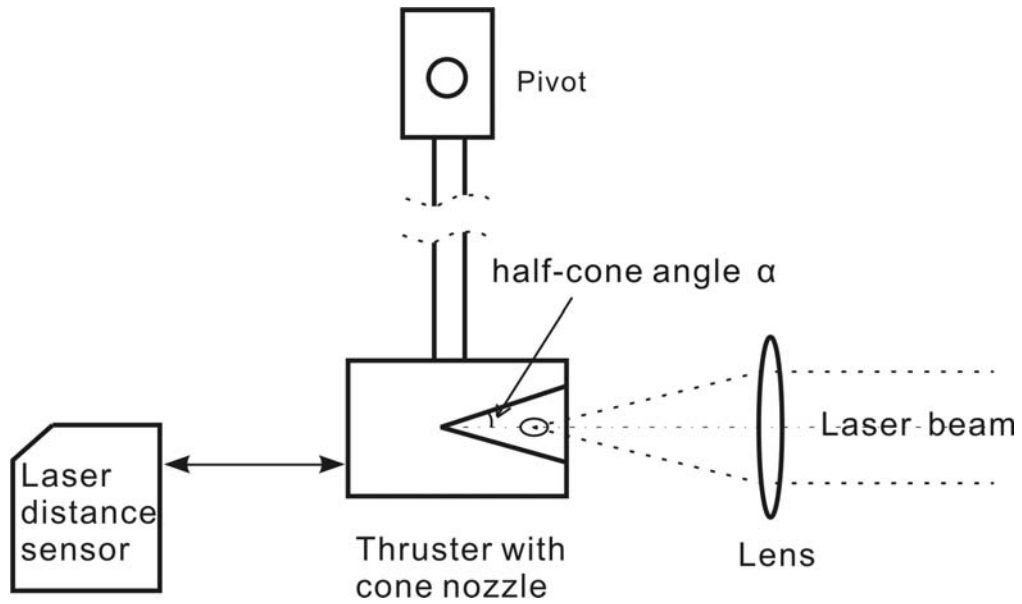
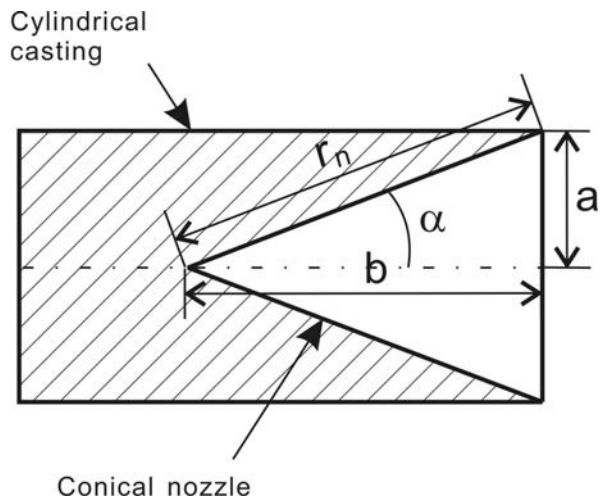


Figure 4.1: Impulse pendulum experimental setup.



(a)

(b)

Figure 4.2: Design map (a) and photo (b) of conical nozzle thrusters.

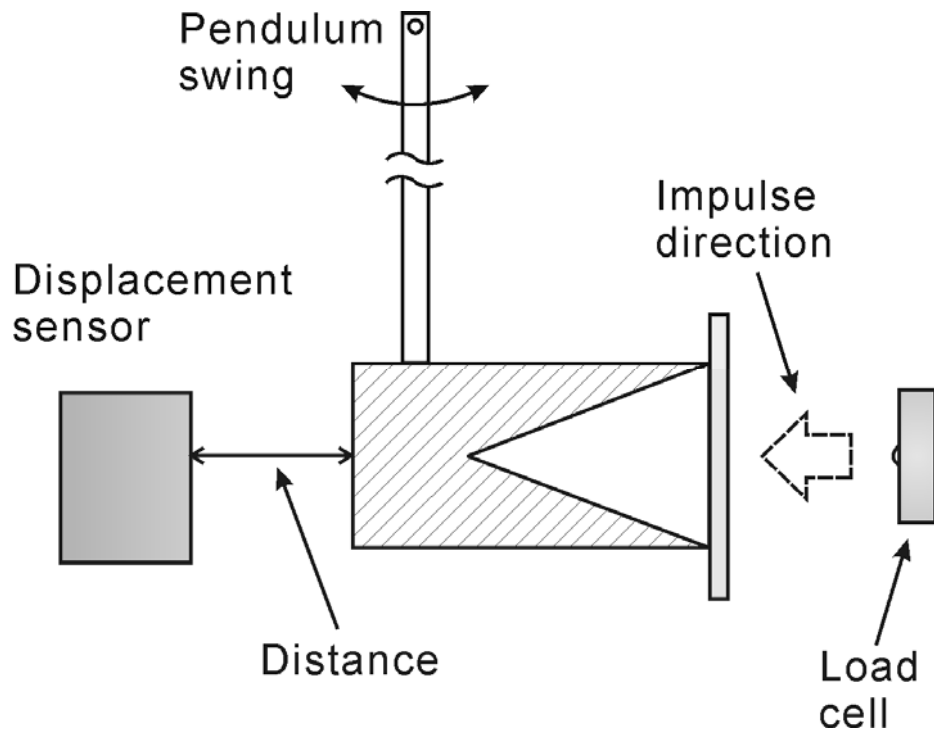
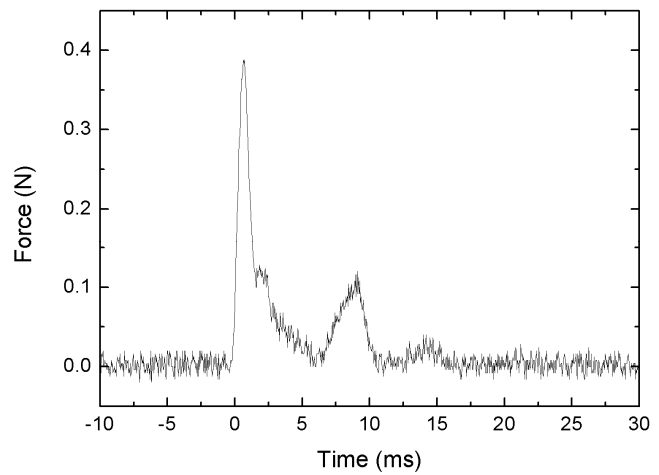


Figure 4.3: Schematic of calibration setup.



(a)



(b)

Figure 4.4: (a) Photo of load cell and (b) typical load cell signal.

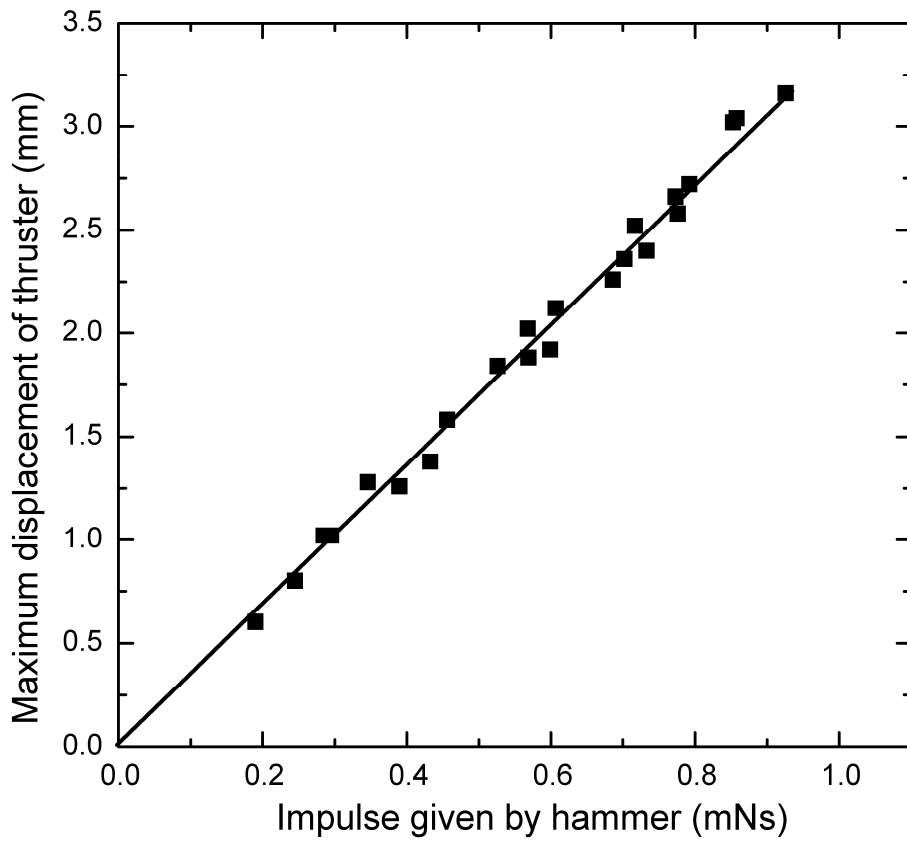


Figure 4.5: Calibration line, using a nozzle with 45° apex angle

## 4.2 Results and discussions

In Figure 4.6, the measured momentum coupling coefficient  $C_m$  result is plotted as a function of a dimensionless nozzle length  $\tilde{r}_n$ , together with the result in the CO<sub>2</sub> laser case<sup>[1]</sup> for comparison. The normalized nozzle length is defined as

$$\tilde{r}_n \equiv r_n / r^* \quad (4-1)$$

here  $r_n$  is the thruster nozzle length,  $r^*$  is a characteristic shock wave radius. For a blast wave expands from a conical apex

$$r^* = \{2E_{bw} / p_a(1 - \cos \alpha)\}^{1/3} = \{2E_t \eta_{bw} / p_a(1 - \cos \alpha)\}^{1/3} \quad (4-2)$$

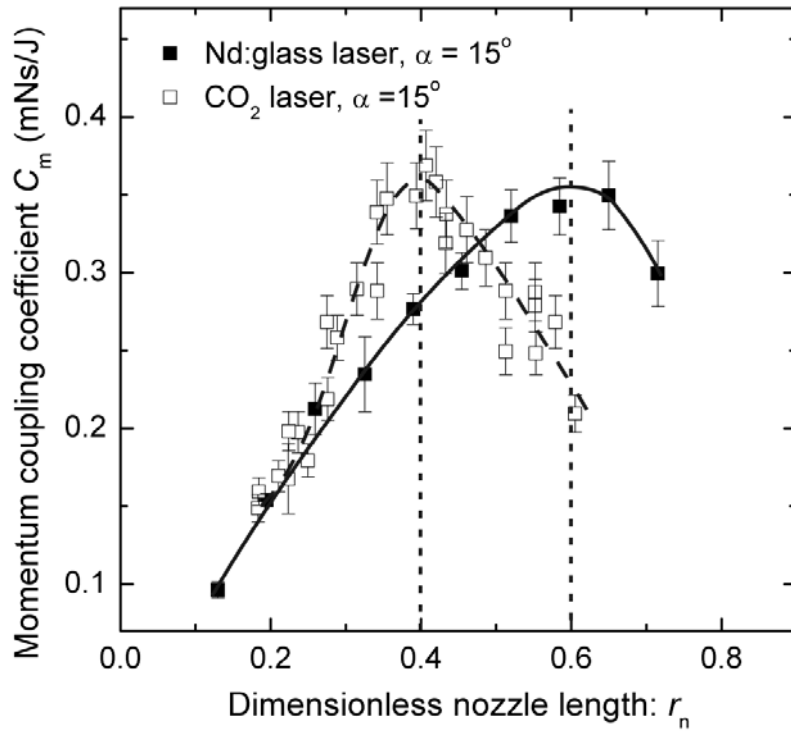
It can be seen that the highest  $C_m$  achieved with the solid laser are 0.35 mNs/J for  $\alpha = 15^\circ$  and 0.27 mNs/J for  $\alpha = 22.5^\circ$ , respectively. These results are almost the same as that obtained in the CO<sub>2</sub> laser cases, which are listed in Table 4.1. It validates the blast wave energy efficiency obtained in the former chapter. Besides, the result shows that  $C_m$  decreases with the increase of half-apex angle  $\alpha$  when other parameters are fixed, which agrees with the calculation result given by Katsurayama<sup>[4]</sup>.

Table 4.1: Measured maximum  $C_m$  with solid state laser, together with data got in former CO<sub>2</sub> laser experiments.

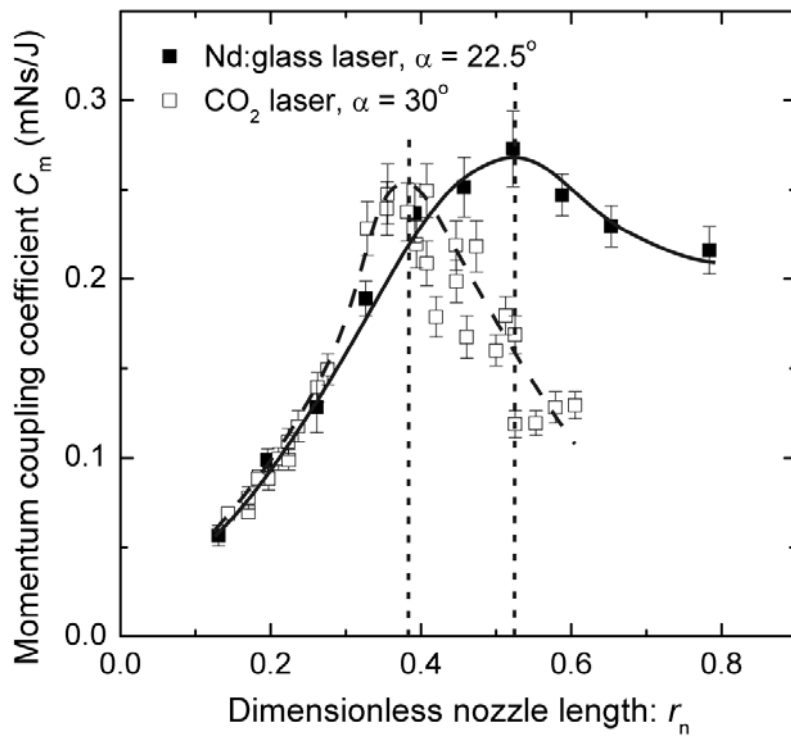
Laser	Nd:glass		TEA CO <sub>2</sub>	
$\eta_{bw}$	59%		44%	
Half-cone angle $\alpha$	15°	22.5°	15°	30°
Maximum $C_m$ (mNs/J)	0.35	0.27	0.37	0.25

For the influence of nozzle size on thrust performance, when using a CO<sub>2</sub> laser, optimized  $C_m$  are obtained at  $\tilde{r}_n \sim 0.4$ , both in Ageev<sup>[5]</sup> and Mori's<sup>[1]</sup> experiments. However, this is different for the solid-state laser.

As shown in the Fig. 4.6,  $C_m$  has a peak at  $\tilde{r}_n \sim 0.6$  for  $\alpha = 15^\circ$  and  $\tilde{r}_n \sim 0.52$  for  $\alpha = 22.5^\circ$ , respectively. Both are larger than the optimized nozzle length gotten in the CO<sub>2</sub> laser experiments. This difference on optimized  $\tilde{r}_n$  is possibly because of the difference on their breakdown positions, and thus the blast wave expansion processes in the nozzles. For two lasers, the blast wave shapes at their corresponding LSD termination time in nozzle lengths of  $\tilde{r}_n \sim 0.4$  and  $0.6$  are shown schematically in Fig. 4.7. As seen, the CO<sub>2</sub> laser experiments (Fig. 4.7(a)) satisfied the assumption that point explosion occurring at the cone apex well, while solid-state laser case not.



(a)



(b)

Figure 4.6: Measured  $C_m$  at various dimensionless nozzle lengths, (a)  $\alpha = 15^\circ$ ; (b)  $\alpha = 22.5^\circ$  for glass laser and  $\alpha = 30^\circ$  for CO<sub>2</sub> laser.

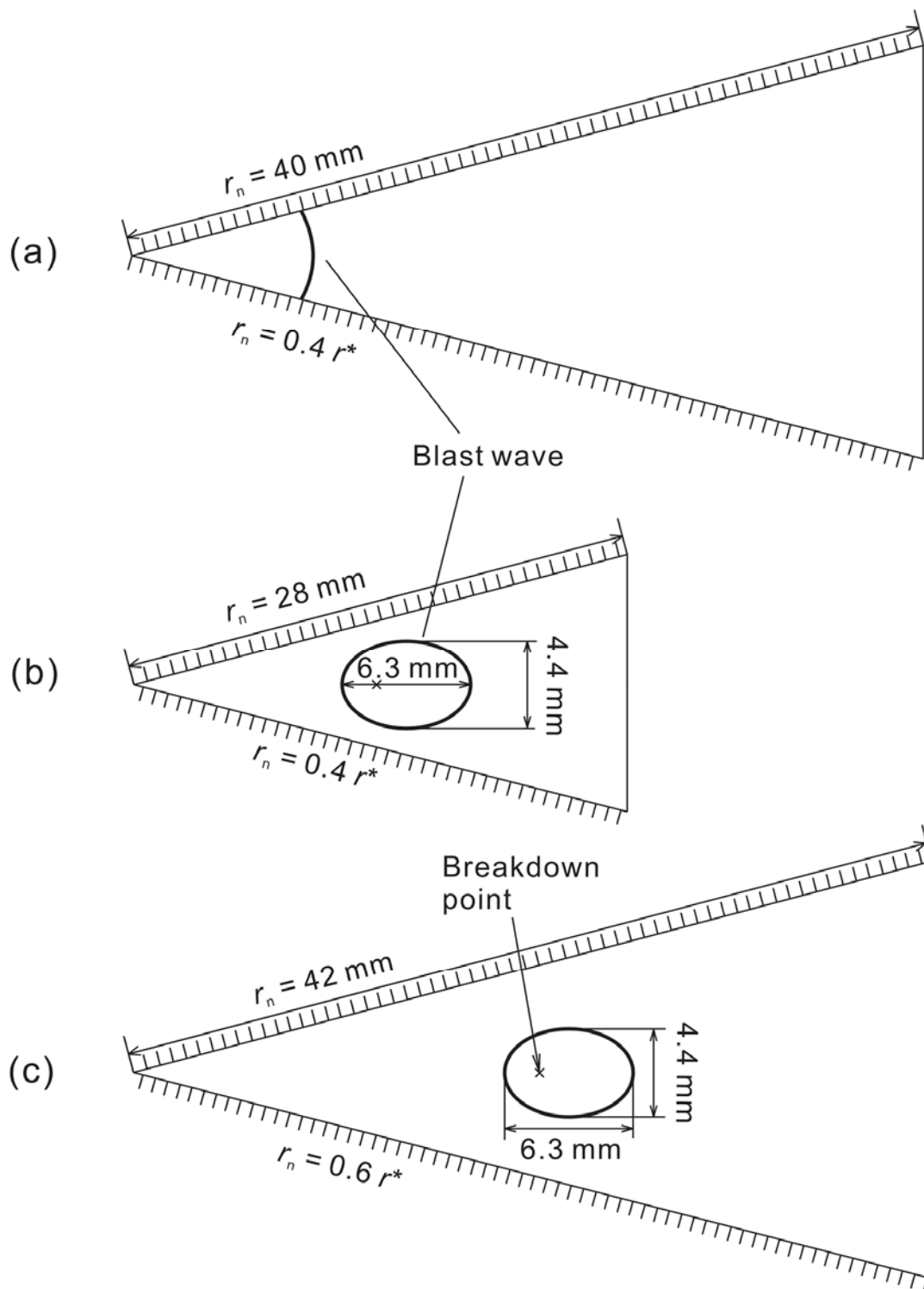


Figure 4.7: Blast wave shapes in the nozzles at LSD termination time, for (a) TEA CO<sub>2</sub> laser, (b) and (c) Nd:glass laser.

### 4.3 Summary of chapter 4

The  $C_m$  gotten with a solid-state laser can reach the same value as that with a CO<sub>2</sub> laser. This result validates the measured blast wave energy efficiency.

For the solid laser, the optimum dimensionless nozzle length is larger than that in the CO<sub>2</sub> laser case.

## References

- 1) K. Mori, K. Komurasaki, and Y. Arakawa, *J. Spacecraft and Rockets* **41**(5): 887-889(2004)
- 2) Myrabo, L. N., Libeau, M. A., Meloney, E. D., Bracken, R. L., and Knowles, T. B., "Pulsed Laser Propulsion Performance of 11-cm Parabolic 'Bell' Engines Within the Atmosphere," AIAA Paper 2002-3783, 2002.
- 3) Nakagawa, T., Mihara, Y., Komurasaki, K., Takahashi, K., Sakamoto, K., and Imai, T., "Propulsive Impulse Measurement of a Microwave-Boosted Vehicle in the Atmosphere," *Journal of Spacecraft and Rockets*, Vol. 40, 2003.
- 4) Katsurayama, H., Komurasaki, K., Momozawa, A., and Arakawa, Y., "Numerical and Engine Cycle Analyses of a Pulse Laser Ramjet Vehicle," *Transaction of JSASS Space Technology*, Vol. 1, 2003, pp. 9-16
- 5) Ageev, V. P., Barchukov, A. I., Bunkin, F. V., Konov, V. I., Korobeinikov, V. P., Putjatin, B. V., and Hudjakov, V. M., "Experimental and theoretical modeling of laser propulsion," *Acta Astronautica*, Vol. 7, 1980, pp. 79-90.

## Chapter 5

### CONCLUSIONS

1. Solid-state laser induced LSD waves expanded in the forward and backward directions as founded in improved Half-Shadowgraph-Half-Self emission experiments. The termination threshold intensity on the backward propagating LSD was estimated at about  $110 \text{ MW/cm}^2$ . This is two orders of magnitude higher than that in the  $\text{CO}_2$  laser induced LSD. The threshold was not sensitive to the pulse energy.
2. The temporal laser absorption and transmission were measured. The laser beam has not been perfectly absorbed in the LSD wave, and transmission was observed even after the breakdown.
3. The pear shape expansion of solid-laser induced blast wave was described with a three directional blast wave expansion model. The blast wave energy efficiency  $\eta_{\text{bw}}$  calculated using this model was as high as 59%. This is almost the same as that obtained with a  $\text{CO}_2$  laser. In addition,  $\eta_{\text{bw}}$  was not sensitive to the ambient pressure when  $50 \text{ kPa} < p_a < 101 \text{ kPa}$ . However, it rapidly decreased as  $p_a$  reduced to 30 kPa.
4. The momentum coupling coefficient obtained with a solid laser reached as high as  $0.35 \text{ mNs/J}$  for a conical nozzle with half-cone angle of  $\alpha = 15^\circ$  and  $0.27 \text{ mNs/J}$  for that with  $\alpha = 22.5^\circ$ , which are almost the same as that gotten by a  $\text{CO}_2$  laser. This result would validate the measured  $\eta_{\text{bw}}$ . For a solid laser, optimized dimensionless nozzle length is at  $\tilde{r}_n = 0.5 \sim 0.6$ , which is longer than the  $\text{CO}_2$  laser case.

5. Solid-state laser gives as good performance as a CO<sub>2</sub> laser in performing laser propulsion mission. Then, we can expect a solid laser power station combining several thousand solid lasers with using latest technology.
6. This series of measurement validates the feasibility of using solid laser as power source in performing laser propulsion. The results will give valuable information to future researches on topics such as reducing laser transmission loss, minimizing the radiation loss, and thruster nozzle geometry optimization.

## Journal Publications and Conference papers (Wang Bin)

### Chapter 1

Kimiya Komurasaki and **Bin Wang** (2010). Laser Propulsion, in *Encyclopedia of Aerospace Engineering*, R. Blockley and W. Shyy (eds). John Wiley & Sons Ltd, Chichester, UK, pp 1351-1360

Kimiya Komurasaki, **Bin Wang** and Yoshihiro Arakawa, “Laser Propulsion: Its Mechanisms and Potentials,” 27th International Symposium on Space Technology and Science, 2009-b-35, Tsukuba, Japan, 2009.

Kohei Shimamura, Keigo Hatai, Koichi Kawamura, Akihiro Fukui, **Bin Wang**, Toshikazu Yamaguchi, Kimiya Komurasaki, Yoshihiro Arakawa, Internal Structure of Laser Supported Detonation Waves by Two-Wavelength Mach-Zehnder Interferometer, *Journal of Applied Physics*, 109,084910(2011).

Kohei Shimamura, Keigo Hatai, Koichi Kawamura, Akihiro Fukui, Akio Fukuda, **Bin Wang**, et al, Structure Analysis of Laser Supported Detonation Waves by Two-Wavelength Mach-Zehnder Interferometer, *JOURNAL OF THE JAPAN SOCIETY FOR AERONAUTICAL AND SPACE SCIENCES*, Vol. 58 (2010), No. 682, pp. 323-329

### Chapter 2

**Bin Wang**, Toshikazu Yamaguchi, Keigo Hatai, Kimiya Komurasaki, Yoshihiro Arakawa, “Energy Absorption Structure of Laser Supported Detonation Wave,” *AIP Conference Proceedings* 1230, Arizona, USA, 2010, pp. 137-147.

**Bin Wang**, Kimiya Komurasaki, Toshikazu Yamaguchi, Kohei Shimamura, Yoshihiro Arakawa, “Laser Detonation Supporting Conditions with a Solid-state Laser”, *Journal of Applied Physics* (will be submitted)

### Chapter 3

**Bin Wang**, Kimiya Komurasaki, Toshikazu Yamaguchi, Kohei Shimamura, Yoshihiro Arakawa, Energy Conversion in a Glass-laser-induced Blast Wave in Air, *Journal of Applied Physics*, 108,124911(2010).

**Bin Wang**, Taro Han, Kohei Shimamura, Toshikazu Yamaguchi, Kimiya Komurasaki, Yoshihiro Arakawa, “Study of Laser Propulsion Efficiency from Solid State Laser to Shock Wave Energy in Reduced Ambient Pressure,” 61st International Astronautical Congress, IAC-10.C4.8.3, Prague, Czech

Republic, 2010.

#### *Chapter 4*

**Bin Wang**, Taro Han, Keisuke Michigami, Kimiya Komurasaki, Yoshihiro Arakawa, “Thrust Measurement of Laser Detonation Thruster with a Pulsed Glass Laser”, *7th International Symposium on Beamed Energy Propulsion, AIP Conference Proceeding*, Ludwigsburg, Germany, 2011

**Bin Wang**, Keisuke Michigami, Kimiya Komurasaki, Yoshihiro Arakawa, “Thrust Measurement for Laser Detonation Propulsion with a Solid-state Laser”, *Journal of Propulsion and Power*, (will be submitted).

## ACKNOWLEDGEMENTS

I would like to express my sincerest appreciation to my supervisor, Professor Kimiya Komurasaki in the University of Tokyo. This work would not have been done without Sensei's professional guidance and patience in supervisions. It is Professor Komurasaki's continuous encouragement and massive help in not only research but also daily life that make me have a great three-year-study in Japan.

I would like to express my sincere thanks to Professor Yoshihiro Arakawa, Research Associate Ai Momozawa. For given me many insightful advices when I was facing to research problems.

I would like to give my particular gratitude to Mr. Toshikazu Yamaguchi, who is not only a good partner in research, but also my personal secretary and my best friend in Japan. I appreciate so much for his self-giving help and great supporting in all respects of my life in the University of Tokyo.

I gratefully acknowledge with deep gratitude the assistance given to me by the RP group members: Mr. Keigo Hatai, Mr. Yutaka Shimada, Mr. Kouhei Shimamura, Mr. Masashi Fukunari, Mr. Keisuke Michigami, and Mr. Yoshihiro Mizuno.

My special thanks should be given to all the lab members: Mr. Satoshi NOMURA, Mr. Tony Schoenhrerr, Ms. Mai Ishiba, Mr. Kensaku Tanaka, for their precious encouragements and valuable supporting.

I wish to express thanks to my Chinese friends in Janpan, Mr. Wang Baotong, Mr. Sun da, Ms. Zhou Juan, who helped me so much and brought me so many precious memories in these years.

Finally, I would like to thanks my family for their tremendous and selfless helps.